A Hybrid Type Small 5-Axis CNC Milling Machine

by

Seung-Kil Son

B.S., Mechanical Engineering
Seoul National University, 1987

M.S., Mechanical Engineering
Seoul National University, 1989

SUBMITTED TO THE DEPARTMENT OF MECHANICAL ENGINEERING IN PARTIAL FULFILLMENT OF THE REQUIREMENTS FOR THE DEGREE OF

DOCTOR OF PHILOSOPHY IN MECHANICAL ENGINEERING

AT THE
MASSACHUSETTS INSTITUTE OF TECHNOLOGY

SEPTEMBER 2002

Signature of Author..
Department of Mechanical Engineering
August 27, 2002

Certified by..
Sanjay E. Sarma
Thesis Supervisor, Associate Professor of Mechanical Engineering

Accepted by..
Ain A. Sonin
Chairman, Department Committee on Graduate Students

A Hybrid Type Small 5-Axis CNC Milling Machine

Seung-Kil Son

Submitted to the Department of Mechanical Engineering
on August 27, 2002 in partial fulfillment of the
requirements for the Degree of Doctor of Philosophy in
Mechanical Engineering

Abstract

5-axis CNC milling machines are important in a number of industries ranging from aerospace to consumer-die-mold machining because they can deliver high machining accuracy with a spindle tilting capacity. Most of these machines have serial mechanisms so that low static and dynamic stiffness become very critical design issues especially for high speed machining. Parallel mechanisms have recently received attention from machine tool designers because of their inherent potential for stiffness and because of their compactness.

However, much of the promised advantages of parallel machines only occur within a very small region of their workspace with the expense of the large machine-tool foot print. We discuss some of the kinematic and structural challenges to extracting machining performance from serial and parallel machines. We compare a hybrid machine, which combines serial and parallel mechanisms, with typical serial and parallel machines such as Euler angle machines and the Hexapod. In particular, we consider singularities, reversal characteristics, and manufacturability. We show that hybrid machines can benefit from the advantages of serial and parallel mechanisms while avoiding most potential pitfalls of both mechanisms.

However, hybrid structures can suffer from the manufacturing problem of over-constraint. We show that the degree of over-constraint depends on the size of the parallel machine. We have designed and fabricated a small hybrid 5-axis motion platform, the MIT-SS-1, which can tolerate this over-constraint through a novel layout of axes. Numerical and experimental test results of the MIT-SS-1 are presented and compared. Finally we show that this structure has potential as a small 5-axis CNC milling machine.

Thesis Committee:	Professor Sanjay E. Sarma, Chairman, Mechanical Engineering, MIT
	Professor Alexander H. Slocum, Mechanical Engineering, MIT
	Professor Samir Nayfeh, Mechanical Engineering, MIT

Acknowledgement

Many people have contributed to develop a new hybrid type machine tool, the MIT-SS-1, over the last few years. First and foremost, I would like to express my appreciation to my advisor, professor Sanjay E. Sarma, for the guidance and support. It was my great experience to work with him in my life. Professor Sarma who has broad engineering insight as well as profound understanding, was willing to listen and offer advice which always got me on the right track whenever I got stalled on a problem.

I'd also like to thank the other members of my thesis committee, professor Alexander H. Slocum and professor Samir Nayfeh, both of whom have provided many good suggestions and different perspectives, for sharing expertise in machine tool design. The concept of the hybrid mechanism with one installation plane was based on the discussion with them.

Special thanks also to Dr. Taejung Kim for his time and help toward this work; the discussions I had with him made the problems I faced clearer, and often provided me with lucid and valuable insights into my work. To Mark and Gerry in LMP machine shop for their help toward machine fabrication, and Kripa, who helped me test the fabricated structure for the last few months; most of the experiment's mode shapes in my thesis were from his help. And thanks to Ajay and Kirit for their willingness to help me assemble the machine, the MIT-SS-1, and proofread my thesis. I also wish to thank Jinpyung, Hyung-Soo, Dohyoung and Kwangduk for their help during my stay at MIT.

Finally, I'd like to express my gratitude to my family. During my time at MIT, my wife, Hyun-Seo, always encouraged me to do my best when I was down. Her love, support and encouragement have allowed me to make it to the end of this experience. My mother has been anxiously waiting for me to finish my Ph.D course. My son, Jeong-Won, and my daughter, Jeong-Hee, have given me a hope and great joy, and they have grown up well. I will always remember the time I spent with my family at MIT.

Table of Contents

List of Figures

List of Tables

1 Introduction

1.1 Overview

Machine tool users perpetually seek faster, stiffer, more compact and more accurate machines, especially those with 4 or 5 axes and greater reach and dexterity. Stewart Platforms, parallel kinematic machines (PKM's), shown in Figure 1, have recently received consideration as machine tool structures in this context. However, these objectives compete, and informed trade-off's need to be made to optimize machine tools for the particular application; indeed the feasible space in machine design is tight, and there is a little margin for error in the design process. When Stewart Platform machines first emerged as a possible machine tool configuration in the early nineties, there was considerable excitement in the machine tool users community about their potential. Unfortunately, the trade-offs in the design of hexapod are mathematically inescapable, and this usually leads to quirks in performance such as an oddly shaped workspace or varying speed capability in the workspace [19,27,29]. Consider for example, the trade-off between stiffness, workspace size and machine-tool footprint. A feature much highlighted of hexapods in machine tool magazines a few years ago was greater reach, stiffness, and accuracy for a machine tool of relatively small footprint [53]. However, analysis suggests that the stiffness of the hexapod is very sensitive to its location in the workspace, and indeed that the stiffness and accuracy rapidly drop as the spindle moves away from the "sweet-spot" of the machine [8,14]. Generally, PKM's have very limited orientation space. In fact, the stiffness vanishes completely in certain configurations known as singular configurations.

At the same time, serial mechanisms have a number of drawbacks which do make PKM's attractive. One major problem with serial machines is that serially stacked-up axes tend to

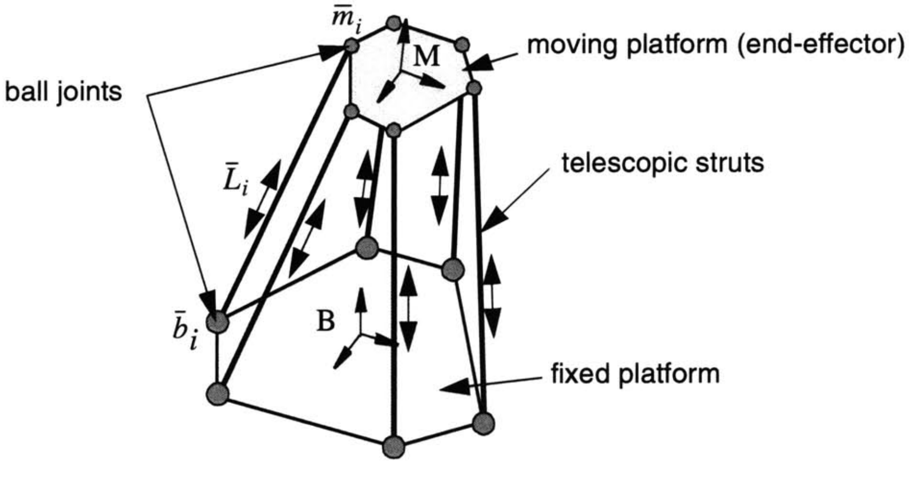

Figure 1 Stewart Platform

balloon in size—joints lower in the serial chain, which carry the higher joints, must be larger and stiffer, and this effect cascades serially. A stack-up of 3 axes, which is necessary in a 5-axis machine, is always limiting because to achieve static stiffness, the structure needs to be quite substantial, which reduces dynamic performance. PKM's, on the other hand, have less moving mass because they don't suffer from this form of stack-up. Another common problem in 5-axis serial machines, which has received little attention so far in the machine-tool literature, is "*manipulability*" loss. Many 5-axis machine tools today have a degree of freedom known as the *C-axis*. The attraction of the *C-axis* is that it is compact, and mitigates the stack-up problem — but this results in loss of performance. When the spindle is oriented parallel to this axis, it may enter a state similar to gimbal lock. In a sense, this loss of manipulability is a mathematical dual of the kinematic singularity.

In many ways, PKM's and serial machines are the opposites of each other. For example, while it is the solution of the forward kinematics of PKM's which is difficult, it is the inverse kinematics of serial machines which poses the real challenge[†]. While serial machines have the problem of axis stack-up, and therefore more error build-up, PKM's have extra passive joints in the structure, providing more scope for compliance build-up. There are other such dualities, and some researchers have argued that a hybrid concept, which combines the benefits of parallel and serial machines, avoiding the pitfalls of both, may be an ideal configuration [9].

In this thesis, we list kinematic and structural problems that machine designers must be aware of in the synthesis of serial, parallel or hybrid machines, and describe the MIT-SS-1, which is a hybrid 5-axis structure designed specifically to avoid the pitfalls of parallel and serial machines. We discuss how the MIT machine addresses these problems. We also attempt to understand the dimensional effect on the structural stiffness in both mechanisms based on the dimensional analysis. Then we address the design process and the fabrication issues which include part machining and assembly of the MIT-SS-1. Based on the numerical and experimental results, we introduce a few important issues which are related with structural static/dynamic stiffnesses and tracking performance, and show that the hybrid type structure, the MIT-SS-1, can be potentially used as a small 5-axis CNC milling machine.

This thesis is organized as follows. In Chapter 1, we present a brief review of the literature surrounding new parallel structures based on the industrial applications, design processes, kinematics, and a hybrid concept which combines a parallel mechanism and a serial mechanism. In Chapter 2, we list a series of kinematic and structural considerations that must be kept in mind in the design of machines, both serial and parallel, and introduce several challenging issues in the design of a new type 5-axis machine tool. In Chapter 3, we investigate the scaling effects on the

---

[†] There is no passive joint in serial machines, which implies that it is easy to find an end-effector position and orientation with known actuator coordinates. Passive joints in PKM's generally make it difficult to find an end-effector position and orientation with actuator coordinates but it is easy to find active joint coordinate with known end-effector coordinates because passive joint displacements can be easily found with end-effector coordinates.

structural stiffness and illustrate numerical examples of serial and parallel mechanisms. In Chapter 4 we show that the reversal characteristics of parallel machines are more complicated than that of serial machines. Reversal effects and their occurrences in both machines are discussed and shown with examples. In Chapter 5 we go through the reasoning process of selecting a kinematic structure that minimizes the downsides of both serial and PKM's and then describe the MIT Hybrid Structure, the MIT-SS-1. In Chapter 6, kinematic properties of the MIT-SS-1 are investigated and numerical analysis results with solid model are shown. In particular, we point out the problem of over-constraint and show that it can be addressed with a novel axis layout. In Chapter 7 we summarize some of the performance targets for this machine. In Chapter 8 issues related with fabrication, such as part machining with high accuracy and bearing assembly, are dealt with. We have investigated the tracking performance and the static/dynamic stiffness with the MIT-SS-1. The experimental results are discussed and several mode shapes and frequencies are shown in Chapter 9. We describe a moving-bridge variant of the structure in Chapter 10, which can be used as a 4-axis machine for manufacturing long aerospace spars or marine components. We conclude in Chapter 11 and future works are discussed in Chapter 12.

1.2 Background

Over the last decade, PKM's have garnered much attention in machine tool research area because of their inherently high structural rigidity and low inertia. The machine tool industry and research universities have developed and evaluated various type of PKM's in an effort to adopt the advantages of parallel mechanisms for 5-axis machine tools. Several working prototypes including the Triaglide by ETH and HexaM by Toyota have been reported to have comparable performance to conventional machine tools [16,41]. There are over 20 hexapod machine tool designs in existence world-wide, and many more in existence for pick-and-place applications. A broad discussion about machine tool applications of parallel mechanism and existing prototypes in industry is available in [10]. The website [6] contains an ongoing list of parallel machines.

In designing PKM's, the most time-consuming process is often the conceptual design phase because it determines the fundamental structural characteristics on which machine performance and manufacturing costs depend. Much efforts have been added on the development of design methodology by many researchers. A design methodology using connectivity which is defined as the degrees of freedom (dof) associated with the joints of the limb in parallel manipulators was introduced by L. Tsai [54]. Once the connectivity of each limb is decided, a joint type can be assigned and feasible configurations of limb mechanisms can be enumerated using combinatorial analysis. From an engineering point of view, G. Pritschow and K-H. Wurst describe a systematic design process for parallel manipulators using 3-dof arm elements [42]. By constraining the joint type, infeasible design candidates can be removed at the conceptual stage. An integrated design methodology by considering the virtual environment was suggested by Tosatti *et al.*[35]. And design parameters of PKM's are analyzed with the concept of vertex in [23].

Many passive joints are incorporated in PKM's, which makes the kinematics of parallel mechanisms more challenging. One of the most critical challenges in the design of PKM's is that of actuator singularities, at which the mechanism loses the rigidity, in the workspace. A. Karger and M. Husty [25] demonstrate all possible actuator singularities in the original Stewart-Gough platform. When the Jacobian matrix or inverse Jacobian matrix loses rank, the mechanism loses its mobility or rigidity in some direction and such configurations are called kinematic or actuator singularities [8,36]. The singularity of different kind of parallel mechanisms are investigated and analyzed in [12]. Forward kinematics of parallel mechanisms are challenging for control purpose. Innocenti and Parenti-Castelli solved the forward kinematics of 6-6 general hexapod in [20,21,22].

The end-effector position and orientation errors are very important for machine tool applications. The dimensional errors in the parallel mechanisms can affect the end-effector position and orientation accuracy in all directions. To compensate the errors, error sources and their effects are investigated in [40,61].

Several researchers have qualitatively or quantitatively evaluated PKM's for their use as machine tools considering structural stiffness, acceleration capability, and dynamic performance. Tlusty *et. al.* show that PKM's with fixed length struts are possibly comparable to the conventional Cartesian machine tools in particular applications in [50]. El-Khasawneh and P. Ferreira [8] compare the advantages and disadvantages of serial and parallel mechanisms qualitatively and also develop kinematic theory related to stiffness near singularities. They were among the first to suggest hybrid serial-parallel concepts as an approach to melding the advantages of serial and parallel mechanisms. In [9] the same authors also describe a hybrid 3-axis platform. Tonshöff and Grendel [52] observe that in production engineering, most applications of parallel mechanisms have been in the role of robots and positioning devices. For machine tool applications, they too compare drive mechanisms, and suggest the use of fixed length strut and rotary arm joints as favorable for tasks which require high forces and high speeds.

The study of PKM's, and our work also draws significantly from the robotics community. Some valuable resources where various types of singularities are described can be found in [36]. The robotics community has also studied manipulability in many contexts [32,44,63].

2 Kinematics of Serial and Parallel Structures

In this chapter we list the kinematic and structural challenges that must be addressed in the machine tool design process. The factors considered here include standard kinematic theory, new kinematic observations, and some practical facts gathered from our experience in using and designing machine tools, especially PKM's.

2.1 Singularities in serial and parallel machines

Singularity is defined as the Jacobian matrix or the inverse Jacobian matrix loose rank. Let X be the end-effector configuration and Θ be the active joint angles of a machine tool, which are specified by 5-tuples.

$$X = \begin{bmatrix} x \ y \ z \ a \ b \end{bmatrix}^T \tag{1}$$

$$\Theta = \begin{bmatrix} \theta_1 \ \theta_2 \ \theta_3 \ \theta_4 \ \theta_5 \end{bmatrix}^T . \tag{2}$$

where x, y, and z are the translational Cartesian coordinates of the machine, and a and b are the rotational coordinates, in some pre-selected reference frame attached to the world, and where θ_i are the displacements of the 5 linear or rotary actuators in the machine. In a 5-axis machine, the degree of freedom associated with the space about tool axis is not in our interest. The relationship between X and Θ can be written as

$$F(X, \Theta) = O \tag{3}$$

where F is a 5 dimensional column vector. By differentiating Equation 3 with respect to time, we have:

$$F_X\dot{X} + F_\Theta\dot{\Theta} = O \tag{4}$$

where $F_X = \frac{\partial F}{\partial X}$ and $F_\Theta = \frac{\partial F}{\partial \Theta}$.

If F_X is not singular, the Jacobian, J, of the mechanism, which is useful for investigating kinematic properties, such as manipulability, kinematic and actuator singularities of the mechanism, can be obtained by using F_X and F_Θ as in Equation 5.

$$J(X, \Theta) = -F_X^{-1}F_\Theta \tag{5}$$

so that $\dot{X} = J\dot{\Theta}$. Likewise, we can define, $J^{-1} = -F_\Theta^{-1}F_X$, when F_Θ is not singular. When F_X or F_Θ becomes zero, the structure experiences kinematic or actuator singularities and loses the mobility or rigidity respectively.

2.1.1 Actuator Singularities in PKM's

Actuator singularities are a well-studied phenomenon in robotics literature [36]. The amount the tool deflection in the face of cutting forces is determined by the static and dynamic stiffness of the system. In some configurations of parallel mechanisms, actuator forces are not transmitted to the end-effector and the end-effector can not resist external forces in some directions. These configurations are called actuator singularities and they can be investigated by looking at the Jacobian. However, any passive joint is not incorporated in serial mechanism so that actuator singularity does not exist and the mechanism can resist any directional forces with stiffness.

In general, near singularities, the stiffness of the structure is usually much lower than far away from singularities, which is one of the drawbacks PKM's have. The workspace of the machine where high stiffness is achieved can therefore be related to the location of the points of singularity.

The torques and forces on the end-effector, T, are related to actuator torques and forces, G, as follows [8]:

$$T^T \Delta X = G^T \Delta \Theta . \tag{6}$$

The equation above can be written in terms of the Jacobian and the actuator resisting forces as:

$$T = J^{-T} G . \tag{7}$$

Clearly, when J^{-1} loses rank, the end-effector loses the capability of resisting force or torque in some direction. It can also be shown that in the neighborhood of these singularities, the machine becomes mechanically disadvantaged [8]. Joint compliances become magnified significantly, and machine stiffness is greatly compromised. This problem is especially severe in PKM's because these mechanisms have many passive joints, whose compliances add.

2.1.2 Kinematic singularities in serial machines

Interestingly, actuator singularities don't occur in serial mechanisms as explained in the previous section. However, a dual of the actuator singularity exists for serial machines, which we refer to as a kinematic singularity. Essentially, serial machines instantaneously lose a degree of freedom. Paths except very special ones which pass through these configurations cannot maintain velocity tracking, which is a serious drawback, especially in high-speed machines. A large number of serial machines today suffer from this drawback.

The effect can be demonstrated though the Jacobian. In some configurations, the rank of

Jacobian matrix drops, and in these configurations, the mechanism loses manipulability in some directions [32]. When the end-effector velocity is known, the required actuator velocity can be obtained with Equations 4 and 5 as shown in Equation 8:

$$\dot{\Theta} = J^{-1}\dot{X} = \frac{1}{|J|}adj(J)\dot{X} \tag{8}$$

Equation 8 implies that infinite actuator velocity is required at a kinematic singularity to achieve definite end-effector velocity in some direction.

This kinematic singularity is very common in conventional Cartesian 5-axis machine tools which incorporate two rotational axes. The nomenclature for axes is as follows: rotation axes aligned (in home position) to the *x*-, *y*- or *z-axis* are referred to as the *A*-, *B*- and *C-axis* respectively. In *5-axis* Cartesian machines, two of these three rotational axes are typically used as shown in Figure 2-(a). This implies that there are configurations of the rotational axes in which the spindle axis is aligned with one of the two rotational axes. Let $\vec{q}$ be the unit direction vector aligned with spindle axis and q_x, q_y, q_z be its components. Let *a*, *b*, *c* be the Euler angles corresponding to *A*-, *B*-, and *C-axis*. Vertical type Euler angle machine tools use only (A, C) or (B, C) axis pairs, and horizontal type Euler angle machine tools use (A, B) axis pair.

In the case of vertical Euler angle machines, because $q_x = sin(a)sin(c)$, $q_y = -sin(a)cos(c)$ and $q_z = cos(a)$, differentiating them with respect to time leads to:

$$\begin{bmatrix} \dot{q}_x \\ \dot{q}_y \\ \dot{q}_z \end{bmatrix} = \begin{bmatrix} cos(a)sin(c) & sin(a)cos(c) \\ -cos(a)cos(c) & sin(a)sin(c) \\ -sin(a) & 0 \end{bmatrix} \begin{bmatrix} \dot{a} \\ \dot{c} \end{bmatrix} \tag{9}$$

Equation 9 shows that the mechanism which consists of two rotational axes (A, C) has only one rotational degree of freedom when the orientation angle, *a*, becomes zero. The spindle axis is aligned with *z-axis* in this configuration, and one rotational degree of freedom has been lost. This can be a serious problem in the Cartesian machine tools because it usually occurs in the middle of the orientation workspace.

In the case of horizontal machines, $\dot{q}_x$, $\dot{q}_y$, $\dot{q}_z$ can be expressed in terms of (a, b) and $(\dot{a}, \dot{b})$ as:

$$\begin{bmatrix} \dot{q}_x \\ \dot{q}_y \\ \dot{q}_z \end{bmatrix} = \begin{bmatrix} 0 & cos(b) \\ -cos(a)cos(b) & sin(a)sin(b) \\ -sin(a)cos(b) & -cos(a)sin(b) \end{bmatrix} \begin{bmatrix} \dot{a} \\ \dot{b} \end{bmatrix}. \tag{10}$$

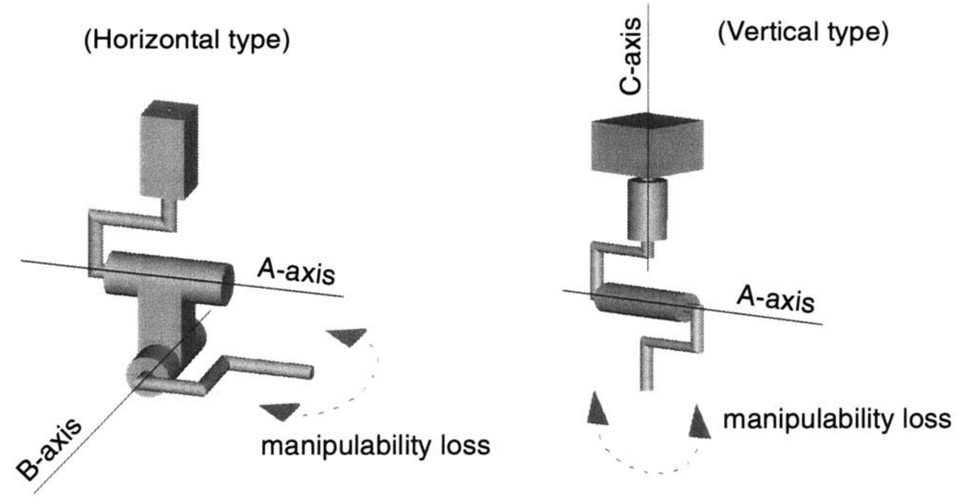

(a) Euler-angle machine tools

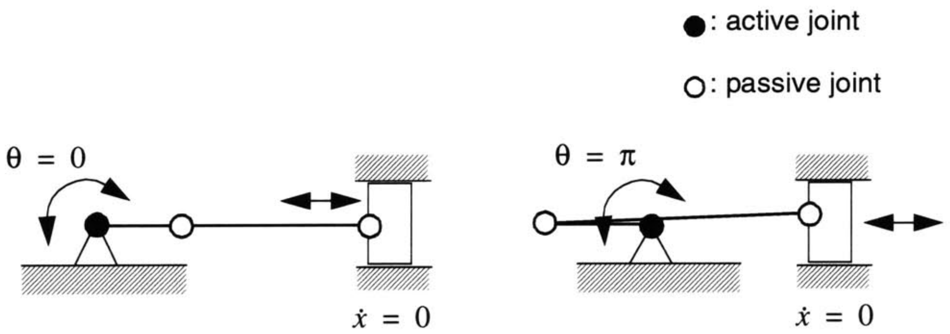

(b) PKM with 1-dof

Figure 2 Kinematic singularity configurations

When b is equal to $\pi/2$, the mechanism loses one rotational degree of freedom. In general, such singularities can not be avoided in 5-axis serial machine tools. The challenge is to place the points of singularity outside the workplace. The use of *C-axis* in machine tools is usually the source of the problem. Most 5-axis CNC machine tools in the field today are *C-axis* machines, and consequently, suffer from this debilitating problem. Note that this problem occurs regardless of whether the axes are stacked together, or are at different locations in the serial chain. The temptation of using a *C-axis* arises from the fact that the *C-axis* is a more compact addition to a serial 3-axis or 4-axis machine than an *A-axis* or a *B-axis*.

Given the inertial and structural stack-up challenges associated with serial machines, which we will discuss in Chapter 5, this compactness of *C-axis* machines is often the only way to achieve 5-axis motion without reducing machine performance. Kinematic singularities also occur in PKM's, as shown in Figure 2-(b).

2.2 Manipulability

In the robotics community, manipulability at a given configuration is defined as the ability to change the position and orientation of the end-effector in an arbitrary direction [36]. Complete loss of manipulability was defined above to be a kinematic singularity. Even if the singularity position has not been reached, manipulability can be limited in some configurations, and this can be quantitatively measured with one of: 1) minimum eigen value, 2) the condition number or 3) the determinant of the Jacobian[†]. Manipulability can be visualized with the velocity ellipsoid when the mechanism is not in a singular configuration. The more anisotropic this ellipsoid, the more difficult it is to plan tool paths. Manipulability for position and orientation can be investigated independently with the condition that either orientation or position is fixed [27,29].

Position manipulability can be investigated with the condition that rotation axes are fixed, $\dot{a} = 0$ and $\dot{b} = 0$. We partition the inverse of the Jacobian matrix into $J^{-1} = \begin{bmatrix} C_t & C_r \end{bmatrix}$ where C_t is 5×3 and C_r is 5×2. $\dot{\Theta}$ can be written as

$$\dot{\Theta} = \begin{bmatrix} C_t & C_r \end{bmatrix} \dot{X} = C_t \dot{X}_t \tag{11}$$

where $\dot{X}_t = \begin{bmatrix} \dot{x} & \dot{y} & \dot{z} \end{bmatrix}$.

Let $H = (C_t^T C_t)^{-1}$ and V be an orthonomal matrix of H. Multiplying Equation 11 and its transpose leads to:

$$\dot{\Theta}^T \dot{\Theta} = \dot{X}_t^T H^{-1} \dot{X}_t = \dot{X}_{tv}^T D^{-1} \dot{X}_{tv} \tag{12}$$

where D is a diagonal matrix which consists of the eigenvalues of H and $\dot{X}_{tv} = V^T \dot{X}_t$. With the actuator constraint of $\dot{\Theta}^T \dot{\Theta} = 1$ and Equation 12, velocity ellipsoid for position manipulability can be obtained as:

$$\frac{\dot{x}_v^2}{\lambda_{t1}} + \frac{\dot{y}_v^2}{\lambda_{t2}} + \frac{\dot{z}_v^2}{\lambda_{t3}} = 1 \tag{13}$$

[†] Minimum eigen value of the Jacobian implies worst-case end-effector velocity. The condition number and the determinant of the Jacobian imply isotropy in workspace.

where λ_{ti} is $D(i, i)$. Equation 13 describes an ellipsoid whose axes lie along the eigen vectors, V.

Orientation manipulability can be investigated with the condition $\dot{x} = 0$, $\dot{y} = 0$ and $\dot{z} = 0$. The procedure of orientation manipulability is similar to that of position manipulability. Because there are only 2 degrees of freedom in orientation, a 2-dimensional expression is possible. Therefore, orientation manipulability can be visualized with velocity ellipses on a 2-dimensional plane. In case of the hexapods, there are 3-dof orientation so that 3-dimensional expression like position manipulability is possible.

Figures 3, 4, and 5 show the manipulability of the Hexel's Hexapod in *x-A* axis workspace when *B-* and *C-axis* orientations are fixed at zero, $y = 0m$, and $z = 0.4m$. Dimensional information about the Hexapod is shown in Appendix A. There are 3-dof in the Hexapod orientation workspace so that 3-dimensional expression for orientation is possible as for the translation. The velocity ellipsoids of translation and rotation in Figure 3-(a) and 3-(b) show a great deal of anisotropy, which implies that the change of the end-effector position and orientation is not easy in the eigen vector direction associated with the minimum eigen value. On the other hand, the end-effector can move with ease in the eigen vector direction associated with the maximum eigen value.

In case of translation, the minimum condition number is 2.76 and maximum condition number is 3.10, which implies that the manipulability in whole *x-A* workspace is highly dependent on the direction. Minimum eigen values are almost the same (0.46 ~ 0.47) in the *x-A* workspace and the volume of the ellipsoid varies between 0.66 and 0.71.

In case of rotation, the condition number varies a lot (1.45 ~ 7.89) according to the orientation, and the minimum eigen value varies highly also (2.57 ~ 7.04), which implies that the Hexapod's orientation manipulability is highly position and direction dependent, poor in one direction and good in another direction. The volume of the ellipsoid varies between 137.9 and 508.4.

In short, the Hexapod is a highly non-isotropic machine tool such that better mobility of the end-effector can be obtained only along the limited directions.

This has serious implications on tool paths. If a certain constant cutting speed, feedrate, is desired, as might be the case in high-speed machining, the manufacturing engineer has little option but to pick the worst-case speed everywhere in the workspace. This means that the actual performance of the machine, in practical terms, may be very poor. The alternative is to go as fast as possible everywhere. This is a difficult path planning problem which is not available in most CAM systems.

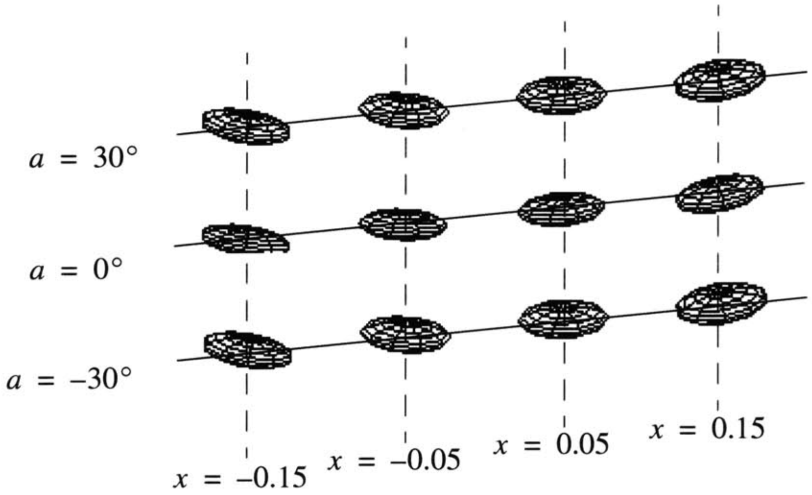

(a) Translation

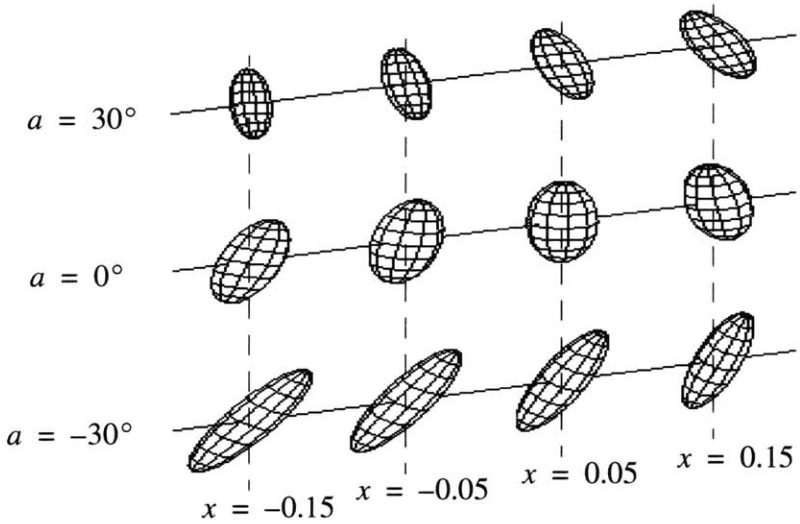

(b) Rotation

Figure 3 Velocity ellipsoids of the Hexapod

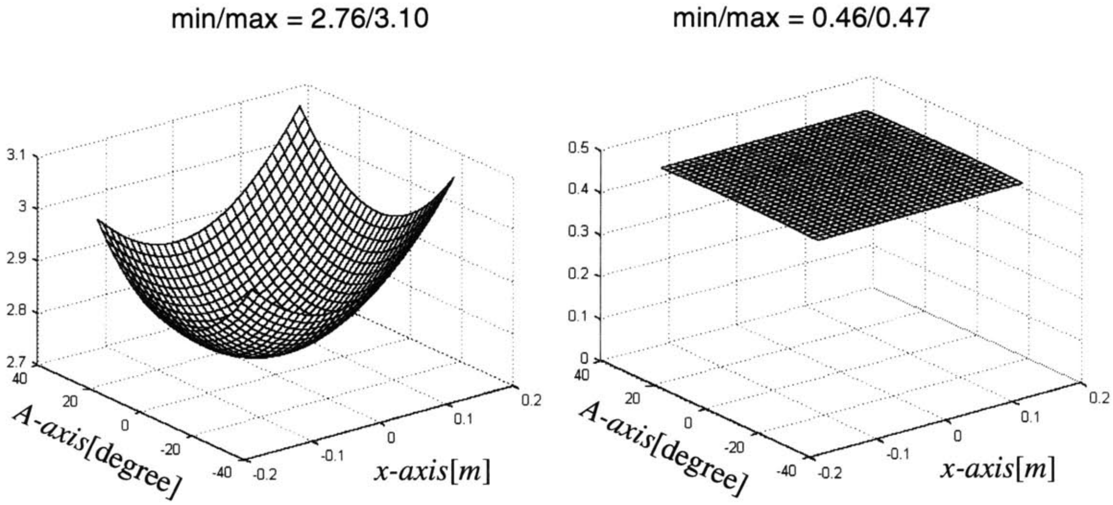

(a) Condition number (b) Minimum eigen value

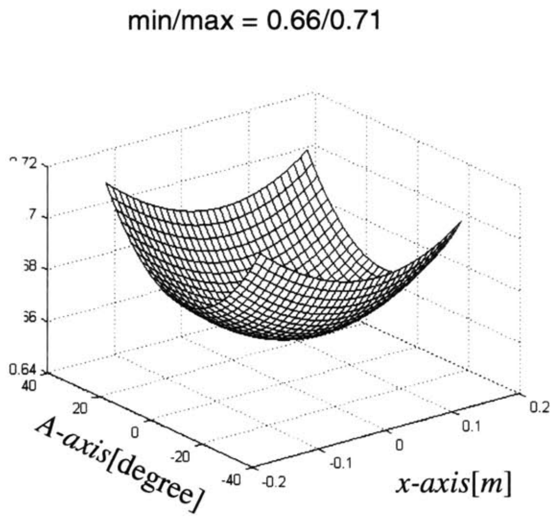

(c) Volume of the ellipsoid

Figure 4 Position manipulability of the Hexapod

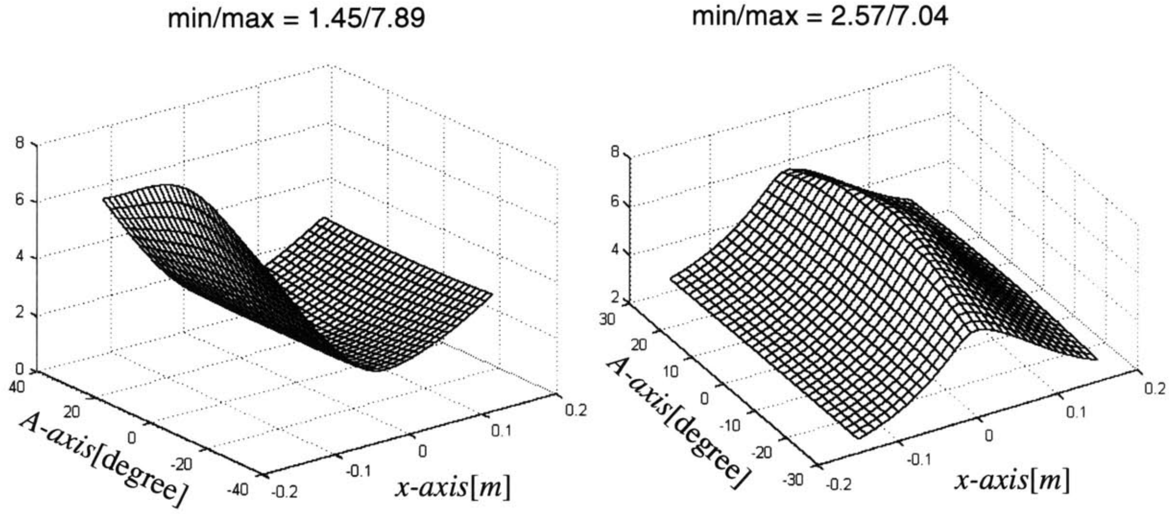

(a) Condition number

(b) Minimum eigen value

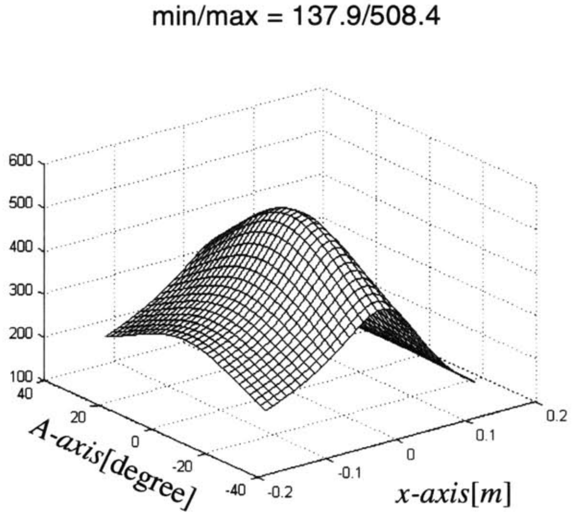

(c) Volume of the ellipsoid

Figure 5 Orientation manipulability of the Hexapod

2.3 The challenges of joint performance in PKM's

The performance of joints poses additional challenges in the design of PKM's. Parallel machine tools have extra passive joints (the hexapod generally incorporates 6 actuators, 6 spherical joints, and 6 universal joints), and each joint adds compliance, error motions and friction to the structure. Furthermore, hexapods, in particular, use spherical joints and telescoping struts. The characteristics, and challenges of designing with several types of joints are compared qualitatively in [17].

Telescoping joints also have other problems. First, they have varying bending stiffness depending on the length to which they are extended. We describe the sources of bending moment later in this chapter. Consider the situation in which the telescope doubles in length. The maximum stiffness variation will be about 800% in bending direction because beam bending stiffness is proportional to $1/(length)^3$. Even though bending a strut may appear in a non-sensitive direction, it can be significant for a precision machine tool. In related work, Tlusty *et. al.* [50] compared 2-dof planar parallel structures with fixed-length struts and telescoping-struts for machine tool applications by considering acceleration capability, workspace, and stiffness variation. They suggest that fixed-length struts have better kinematic characteristics than telescoping struts for machine tool applications.

Second, telescoping joints have the problem of thermal expansion. Fixed-length struts do not have this problem because there is no frictional heat generated directly in the strut — all the heat is generated at the joints, which are pre-loaded. Thermal expansion in prismatic joints can be compensated, for example, by pre-tensioning the baluster. Telescoping joint lengths must, however, be measured and compensated for either directly, using lasers within the screws, or indirectly, with temperature sensors and expansion estimation.[†]

A final class of problems relates to friction. PKM structures are elegant because in the absence of friction, all forces in the joint are purely compressive or purely tensile, theoretically leaving the telescoping elements, or struts, unburdened by a bending load. This makes the use of a screw shaft itself as both the actuator and the strut, and feasible in terms of diameter, because no bending loads are expected. Unfortunately, it is difficult to reduce friction beyond a point in sphere joints as the state-of-the art stands today. Our experience has shown that the friction in the joints does in fact cause the struts to bend, and this severely affects the stiffness of the hexapod. In the absence of a reaction mass in the moving platform, this loss of stiffness greatly reduces the ability of the machine to reject vibration during cutting.

[†] The Giddings&Lewis Variax, for example, uses laser interferometers within each strut. The placement of lasers is not trivial in general because bending in screws can occlude the laser.

2.4 Summary

We have investigated the kinematic properties of serial and parallel mechanisms and have also pointed out a series of potential problems related to the design of both mechanisms in this chapter. The conventional 5-axis machine tools generally have the kinematic singularity and parallel machines have the actuator singularity.

The challenge is to design a 5-axis machine tool that meets the following conditions:

- No actuator singularities in the workspace (a PKM problem)
- Well behaved stiffness in the workspace (primarily a PKM problem)
- No kinematic singularities in the workspace (primarily a serial machine problem)
  - This requires that there not be a *C-axis*
- No reversal-singularities in the *x-y* workspace (will be discussed in Chapter 4)
- Large reversal free region (will be discussed in Chapter 4)
- No telescoping joints
- No spherical joints

3 Machine Scaling

3.1 Introduction

Scaling is one of the most fundamental design methodologies. Most design candidates are generated by scaling the typical models which perform well on specific task such as, machining, pick-and-place, and positioning, during concept design phase. Robot arms, for example, are usually designed with serial chains using the beam elements with scaling at the concept design phase. When a bigger or a smaller mechanism needs to be designed, knowing the scaling law is very helpful to generate new initial configurations.

Generally, the structural morphology which is proper for larger machines is not good for smaller machines. Axial stiffness of a beam is proportional to Ac / L where Ac is cross-sectional area and L is the beam length. If the beam scales with geometric similarity, the stiffness is proportional to the size. The weight, however, is proportional to L^3 with the same condition. The deflection by its own weight is proportional to L^2, which implies that the beam getting stiffer as it becomes smaller. Electric motor torque is generally proportional to L^3, but hydraulic motor torque is proportional to L^2. They experience different scaling laws. Understanding the scaling law, therefore, at the early design stage, can reduce the design cycle time considerably.

Scaling law, known as dimensional analysis, is very well established and successfully applied in fluid mechanics area. Small scale robotic systems are getting attention in robot research area, especially in legged robot area. Scaling laws are applied to the legged robot to achieve more natural motion and better performance [1,57]. The scaling laws of robotic mechanisms are briefly discussed in [58].

3.2 Scaling effects on structural stiffness

We are interested in designing a small 5-axis CNC milling machine. Several important issues in machine tool design should be addressed before configuration design phase, which include the machining accuracy and allowable maximum feedrate. Material Removal Rate (MRR) is considered as the most important machine tool performance parameter due to its economical importance in the field. Dynamic/static stiffness is also essential to good machining qualities, such as surface roughness and dimensional accuracy.

We have attempted to get the scaling effects based on the fundamental machining performance, MRR. Machine tool structure can be considered as a assembly of beam elements. From the beam theory as shown in Figure 6, the bending stiffness, K_b, can be expressed as:

$$K_b \sim \frac{3EI}{L^3} \sim L \tag{14}$$

where $I = \frac{wh^3}{12} = \frac{k_1 k_2 L^3}{12}$, and k_1, k_2 are proportional constants.

On the contrary, parallel machine tools, like the Hexapod, are supposed to resist only compression or extension forces, ideally. Therefore, the representative stiffness of parallel machines, K_p, can be obtained.

$$K_p \sim \frac{EA_b}{L} \sim L \tag{15}$$

where A_b is the cross-sectional area $(w \times h)$ of the strut. From Equation 14 and 15, no matter how the structure type is, we know that the static stiffness tend to increase as the size of the structure increases.

When a larger or a smaller machine tool with the same MRR is to be designed, does the stiffness of the structure tend to change according to Equations 14 and 15? We will present the tendency of the structural stiffness changes as the machine size is changed while maintaining the same MRR. MRR in end milling process can be calculated with feedrate, f, and cross-sectional area of cutting surface, A_c, as shown in Figure 7.

$$MRR = A_c \times f \tag{16}$$

When the width of cut, w, is fixed, the cutting force in x and y direction can be expressed as in Equation 17 [24].

$$F_{c,x} = c_x d \mu_s, F_{c,y} = c_y d \mu_s \tag{17}$$

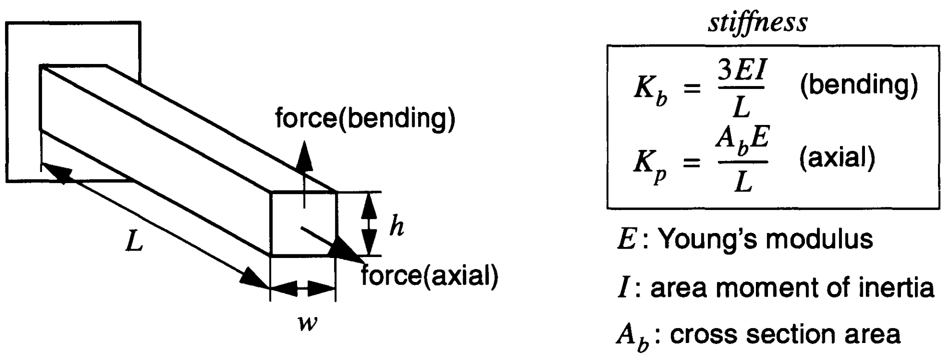

$K_b = \frac{3EI}{L}$ (bending)

$K_p = \frac{A_b E}{L}$ (axial)

E: Young's modulus

I: area moment of inertia

A_b: cross section area

Figure 6 Beam stiffness

where μ_s is the specific cutting energy of the workpiece material and c_x, c_y are constants. The resultant cutting force, F_c, therefore, is

$$F_c = \sqrt{(F_{c,x}^2 + F_{c,y}^2)} = \sqrt{(c_x^2 + c_y^2)}d\mu_s\,. \tag{18}$$

Equation 16 and 18 lead to Equation 19.

$$F_c \sim \frac{1}{f} \tag{19}$$

While machining, a large amount of the actuator force is used for moving the structural masses. Generally the cutting forces reflected to actuators are relatively small when compared to the inertia forces. In Figure 8, cutting forces with typical cutting condition and the inertial force needed to move 500kg mass with 0.5g are compared. The cutting force for alloy steel is about one tenth of the inertia force. In case of the high speed machining, the cutting force becomes much more negligible because the width of cut per one tool tooth, w_t, becomes smaller as the cutting speed increases. We can therefore assume that the required actuator force can be mainly determined by structural mass, *m*. When the minimum radius of curvature, *r*, and the maximum feed rate, *f* are desired, with the assumption that guide systems and driving mechanisms of the axes are ideal, the required actuator force can be written as:

$$F_{actuator} = \frac{mf^2}{r} \sim \left(\frac{\rho}{r}\right)L_c^3 f^2\,. \tag{20}$$

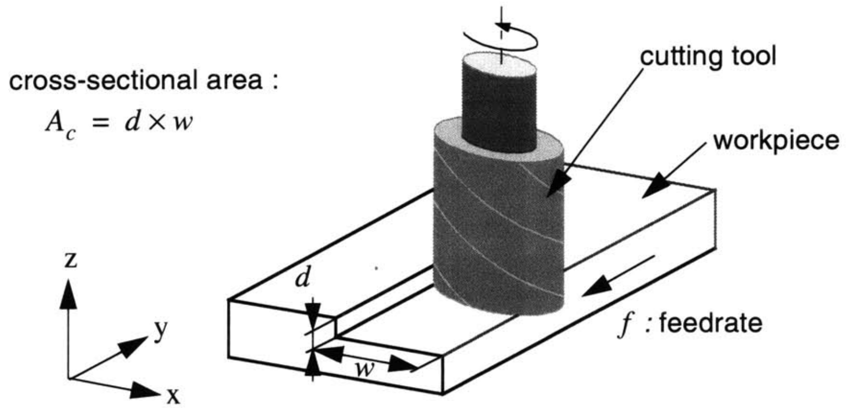

Figure 7 End milling process

where ρ is density, and L_c is the characteristic length of the structure to be moved.

The electric motor characteristics are highly dependent on their shapes and driving types. Specifically, the motor torque is closely related with the motor dimensions. The torque can be easily converted into the axial force by introducing a lead screw. It is assumed that the dimension of the actuator depends on the structure size because the required space for the actuator installation depends on the structure size. Let the actuator force be proportional to L_c^n.

$$F_{actuator} \sim L_c^n \tag{21}$$

We can relate the feedrate and the structure size with Equation 20 and 21.

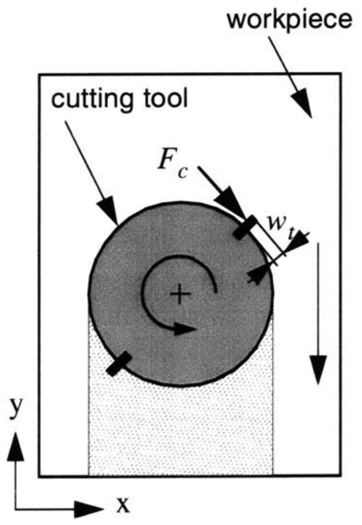

cutting condition:

$w_t = 0.2mm$: width of cut

$d = 0.2mm$: depth of cut

$V_s = 1m/s$: cutting velocity

Material	μ_s $\left[\frac{W \bullet s}{mm^3}\right]$	F_c $[N]$
Al-Alloys	0.76	30
Cast Irons	3.55	142
Steels	6.01	240

(a) Cutting force

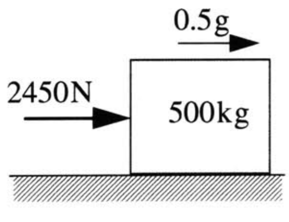

(b) Inertia force

Figure 8 Examples of cutting force and inertia force

$$f \sim L_c^{\frac{(n-3)}{2}} \qquad (22)$$

The static deflection, δ, can be determined with the structural stiffness, K, and cutting forces as written in Equation 23.

$$\delta = \frac{F_c}{K} \sim \frac{1}{L_c f} \sim \frac{1}{\sqrt{L_c^{(n-1)}}} \qquad (23)$$

It is well known that the electric motor torques are generally proportional to the area of the motor cross section and the axial length. This can leads that n in Equation 23 is about 3. In case of the industrial brushless DC servo-actuators, it is investigated that the torque is approximately proportional to $diameter^{3.5}$ [58]. Equation 23 implies that the structural static stiffness increases as the size increases.

Generally, modal frequencies are considered as dynamic stiffness of the structure and the lowest modal frequency, 1st mode frequency, usually becomes the criterion for the structural dynamic stiffness. If we assume that the structure can be modeled as a 2nd order system with a spring and a mass, natural frequency is as shown in Equation 24.

$$\omega = \sqrt{\frac{K}{M}} \sim \sqrt{\frac{L_c}{L_c^3}} \sim \frac{1}{L_c} \qquad (24)$$

Equation 24 implies that the modal frequency increases as the size decreases, and decreases as the size increases. From Equation 23 and 24, we can expect that the larger machines are usually stiffer statically but have lower modal frequencies. On the contrary, we can also expect that the smaller machines have poor stiffness statically but have higher natural frequencies. These results are well consistent with the stiffness characteristics of machine tools used in industry. In general, large machine tools are usually very stiff but suffer from the low modal frequency so that they are not proper for the high speed machining processes but proper for heavy cutting with low feedrate. On the other hand small machine tools suffer from low static stiffness but good for high speed machining with light cutting.

3.3 FEA results

Machine tools consist of many types of mechanical and electrical components which scale differently, which makes it difficult to see the scaling effects on the stiffness of machine tools. If we can assume the sub-systems experience same or similar scaling laws about stiffness, the problem becomes much easier. Roller bearings are very common in joint assembly of machine tools due to their high rigidity, and the stiffness of the roller is proportional to $length^{0.8}$ [15,18]

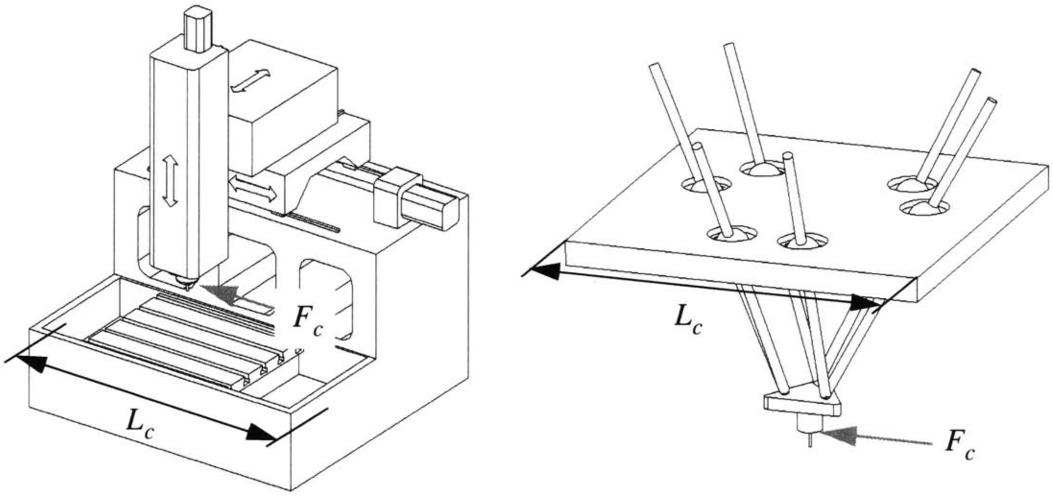

(a) Typical 3-axis milling machine

(b) Hexapod

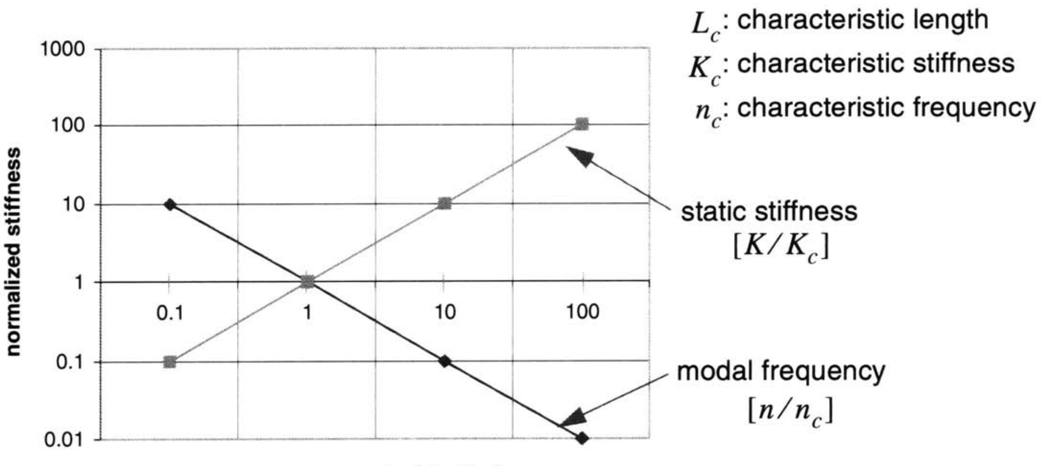

(c) Stiffness change due to scaling

Figure 9 Scaling effects on structural stiffness

so that we can assume that the stiffness of the joint is proportional to the *length*. With this assumption, we can investigate the scaling effect on the structural stiffness easily by changing the dimension. The structural stiffness of a typical serial machine and a typical parallel machine, hexapod, are investigated with the condition that all dimensions of the structure experience similar scaling.

Finite element analysis (FEA) is performed to get the static/dynamic stiffness with different dimensions. Solid models are generated using Pro/ENGINEER. The dimension change can be easily done with the Scale Model function in Pro/ENGINEER. Pro/MECHANICA is used for the numerical analysis. The results show that the scaling effects on the stiffness of a serial structure, Figure 9-(a), are the same as that of parallel structure, Figures 9-(b) and Figure 9-(c) show the relations between the scale and the structural stiffness, which are consistent with Equations 14, 15, and 24.

3.4 Summary

From the simulation results, we can clearly see that scaling the structure affects the static/ dynamic performance of the machine. As the structure gets bigger, the structures becomes stiffer statically and weaker dynamically. This, of course, implies that larger machines are good for heavy cutting with lower feed rate and smaller machines are good for light cutting with high feedrate, or larger machine can use different structural materials which have less density and lower Young's modulus to get similar machining performance. When MRR is maintained constant, the scaling effect depends highly on the actuator characteristics. If the actuator torque is proportional to the size of the structure, $F_{actuator} \sim L_c$, the deflection due to the cutting force does not change as the structure becomes bigger or smaller. However, torque characteristics of DC servo-actuator used in industry is roughly proportional to $L_c^{3.5}$, which implies that the deflection becomes smaller as the structure gets larger.

4 Reversals in Serial and Parallel Machines

When joints in a machine tool reverse the direction of their motion, unmodeled physics is reflected noticeably in the accuracy of a machined surface. For example, friction characteristics of a machine tool become highly non-linear at low operating speed, demanding sophisticated compensation. Motions of each machine tool mechanism are "natural" if they require a small number of reversals of its joints. We have attempted to know the reversal characteristics of the active joints in serial and parallel mechanisms. We show how we find reversal points in a tracking task and the reversal lines in a sweeping task, which is a family of tracking tasks. Then, we present fundamental theorems regarding the reversal of active joints. We also introduce a heuristic approach for reducing the number of reversals for a sweeping task. This reversal characteristic has implications both in design of machine tools and in path planning.

4.1 Introduction

When joints in a machine tool mechanism reverse the direction of their motion, a few anomalies must be taken care of to achieve high precision. In initial design stage of mechanism, those effects are usually ignored under idealized assumptions.

The back-lash in screws is an example. A few guiding systems, pre-loading their elements, are available, which reduce the back-lash; oversized spacers and oversized balls are common in use. However, the amount of pre-loading is limited by friction in bearings and the failure of mechanical elements. Careful consideration must be given to the "non-linear" effect in the friction between the links at a kinematic pair. Figure 10-(a) shows a typical relation between the friction force and the relative operating speed at a joint in a machine tool, which is known as Stribeck effect [48]. When two solids are in relative motion in lubricant, the friction force can be considered linear viscous, which is almost proportional to the relative speed as shown in Figure 10-(a), except for the "Coulomb-like" relation near the regime of low operating speed. Low velocity friction characteristics have been an important issue in the friction and control area due to its complexity [3,7,26,43]. The magnitude of the friction force will increase suddenly if the joint passes such a low speed regime. This requires high values of gain in the controller only for relatively infrequent situations to suppress the disturbance. Simple control strategies such as PID, designed for linear viscous friction models, hardly compensate this effect. This deviation from the viscous friction model can introduce unmodeled delays, irregularity in machined surfaces or loss of precision. The quadrant glitches, as shown in Figure 10-(b), are typical examples generated during circular end-milling in a 3-axis milling machine as a result of such mechanism [56].

Researchers in the field of motion control have proposed several compensation methods to achieve smooth motion with high accuracy under the action of friction. A straightforward solution is to construct an ad-hoc friction response model through experiments and to apply a feed-forward strategy based on the experiments. In [59], a gimbal device in an airborne tracking system is controlled by a strategy based on the time constant of the system measured through experiments under the action of joint friction. It is reported that the quality of the response is sensitive to the environmental factors such as lubrication, vibration, temperature, surface condition and applied load. Strategies for the general purpose disturbance reduction technique can be applied for the friction control. The repetitive control strategy, which adjusts the actuation signal based on the tracking errors in previous cycles, was demonstrated in [56]. In [38], a disturbance observer is designed to detect the sudden change in the friction, and the controller increases the actuation torque accordingly to overcome the friction force. In [2], the authors propose what they call the "non-linear" PID compensation. They gear up two values of control gain depending on the state of the system; obviously, a higher value of control gain is used if the relative speed at a joint is low. A broad discussion about machine tool control with friction can be found in [4].

Recently, parallel mechanisms have been adopted for various applications such as machine tools and industrial robots. The advantage over their serial counterparts is that the load can be distributed more evenly to their kinematic links and, as a result, the necessary stiffness is achieved using lighter structural elements and less-demanding actuators. The "non-prismatic" or coupled kinematics of parallel mechanisms can cause, however, reversals of their joints frequently for seemingly "simple" straight trajectories and the errors in an actuator propagate into all the coordinate axes [10]; this is important when maintaining the planarity or the straightness. In addition, frequent actuator reversals indirectly imply the excitation of higher harmonic components in the machine tool structure [55,62]. This increases the necessary structural stiffness for parallel machines and degrades the advantage of parallel mechanisms.

Absolutely fair comparison among different machine tool mechanisms is not easy to establish for this aspect of machine tool design because the performance is dependent on the required trajectories or the task. Instead, we will ask how many reversals can occur in a typical path and whether it is possible to achieve the same objective with a reduced number of reversals. This chapter is intended to introduce the reversal characteristics of a machine as an additional measure of its fitness to a particular task. The application can be two folds: design and planning. In Chapter 4.2, we set a mathematical framework upon which the rest of this chapter is based. In Chapter 4.3, we answer fundamental questions and show relevant analysis methods. In Chapter 4.4, we show some examples with two types of machine tools, which are serial and parallel machines as shown in Figure 11.

4.2 A Framework for Analysis

Now we discuss mathematical framework upon which the rest of this paper is based. It is assumed that what we will call a *(restricted) inverse kinematic map* is given. This section simply explains and justifies this assumption.

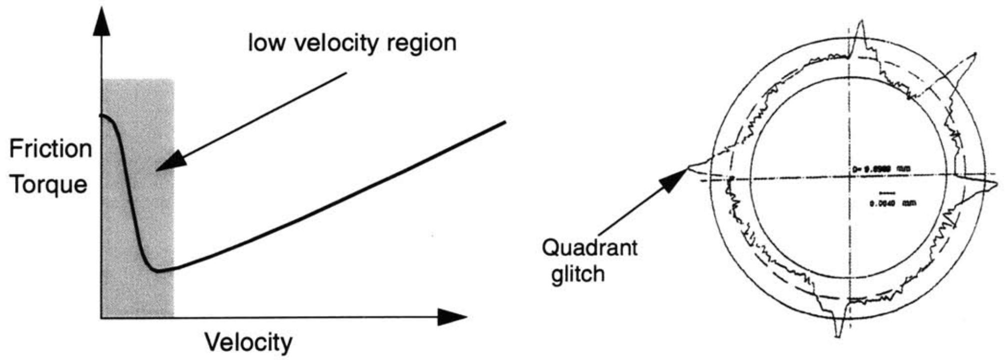

(a) Relation between friction and velocity (b) Quadrant glitches

Figure 10 A typical friction characteristic in a joint and its negative effect in precision.

To describe a motion of a cutting tool, we attach a fiducial point on the center line of the cutting tool “near the tool tip.”[†] The 3-tuples of the Cartesian coordinates of the fiducial point constitutes what we refer to as the workspace of the machine tool. In general, a cutting tool, as a rigid body,

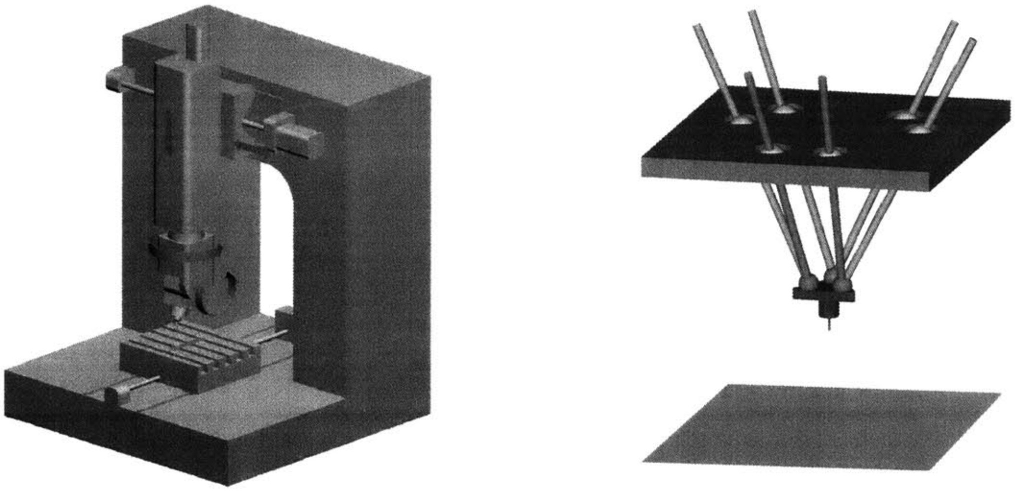

(a) typical serial 5-axis machine tool (b) typical parallel 6-axis machine tool

Figure 11 The machines we consider

has 6 degrees of freedom: three for the translation of the fiducial point and another three for the rotation of the cutting tool. Since we are considering milling machines and their cutting tools can be considered axi-symmetric, the sixth freedom of motion, which is the spin about the centerline of a cutting tool, is typically not a matter of our interest, or redundant. Therefore, to describe the rotation of our "interest," two coordinates are enough. A 5-axis machining strategy takes account of such 5 degrees of freedom, which are decided not by the kinematics but by a planning strategy or our subjective interest. We refer to the number of degrees of freedom of the cutting tool restricted to our subjective interest as the task space dimension of the machining strategy. The task space dimension is not necessarily identical to the degrees of freedom of the machine involved in the machining task. For example, we can perform 5-axis machining using 6-axis machines; the additional one degree of freedom is redundant. In 3 axis machining, only translation of a cutting tool is allowed and its task space dimension is 3. In planning stage, the number can be further reduced by introducing "task constraints." For example in 3-axis roughing, it is common to remove the material in a stock layer by layer; in this case, the task constraint is that the fiducial point should stay on a plane while a layer of material is removed. Then, the task space dimension of machining each layer is reduced to 2. In finishing of 5-axis machining, the "tool tip" is constrained on a designed surface and the task space dimension of finishing is reduced to 4. In a certain planning strategy for finishing, collision-free orientations of a cutting tool at each point on the designed surface can be determined by a pre-processor, and the remaining planning task can be performed on a 2 dimensional space. In this case, the task space dimension is 2.

Consider a machine tool possessing N degrees of freedom and a machining strategy whose task space dimension is $M \leq N$. The motion of a cutting tool, restricted to the strategy, can be captured by a history of an M-tuple of real numbers. The totality of the M-tuples of the restricted postures is referred to as the *task space* under the strategy. The totality of the N-tuples of displacements of actuators in the machine is referred to as the *actuation space*.

We assume that the kinematics of a machine tool and the constraints introduced by a machining strategy determine a C^1 continuous map f from the task space $U \subset R^M$ of the strategy to the actuation space $\Theta \subset R^N$ of the machine tool:

$$f : U \rightarrow \Theta, \quad \boldsymbol{u} \rightarrow \theta = f(\boldsymbol{u}) \tag{25}$$

which we refer to as the (*restricted*) *inverse kinematics* (*map*). Any redundancy must be resolved in a point-wise manner or "holonomically" due to our assumption. We assume that the task space U is simply-connected and that it avoids singularities by choice. The range $f(U)$ of the map is

---

[†] Since a cutting tool has thickness, in surface machining, the contact point between the tool and the surface is not necessarily on the line of symmetry. The readers are referred to [28] for this subtleties. However, the loose definition of the location of the fiducial point suffices for our current purpose.

an M-dimensional subspace of the N-dimensional actuation space. The actuator displacement θ can be thought of as one of the local coordinates of the configuration space of the machine tool. This setting is general enough for our purpose, even though complete generality can be achieved by considering the configuration space of machine tools including both active and passive joints. A rigorous statement of the above assumption exceeds the range of our current treatment, about which the readers are referred to conferring [39,60]. In this chapter, we show how we can capture machining processes into the setting laid down above in regard to the reversal characteristics of given machines.

4.3 Motions in Analysis

we develop several concepts which are useful to judge the reversal characteristics of machine tools. We discuss whether a point-to-point task can be made without any actuator reversals or whether there is a condition that guarantees the reversal-free or surely-reversing path. We also consider also at which point in a trajectory, actuators reverse their direction of motion. Finally, we analyze the reversal characteristics of surface machining or sweeping. The comparison of the 2 machine tools is made in Chapter 4.4 using the notions developed in this section.

4.3.1 A Reversal Condition

In this section, we show various ways to interpret the reversals of actuator displacements.

4.3.1.1 A Reversal Condition on a Trajectory for a Tracking Task

A fundamental functionality of a machine tool is the ability to track a specified trajectory of the configuration of its end-effector. We consider the fiducial point of a machine tool moving along a *regular* trajectory $\boldsymbol{u}: t \in [0, T] \rightarrow \boldsymbol{u}(t) \in U$ in the task space U. The condition for the reversal of the actuators is obvious in this case. For the *i-th* actuator to be reversed at $t \in [0, T]$, it is sufficient that

$$\dot{\theta}_i(t) \equiv \frac{d}{dt} f_i(\boldsymbol{u}(t)) = \sum_{j=1}^{M} \left(\frac{\partial f_i}{\partial u_j} \cdot \frac{du_j}{dt} \right) = 0 \text{ and } \ddot{\theta}_i(t) \equiv \frac{d^2}{dt^2} f_i(\boldsymbol{u}(t)) \neq 0 . \qquad (26)$$

If the actuators reverse their directions of motion at a point $\boldsymbol{u}(t_o) \in U$ or at $t = t_o$, we refer to the point $\boldsymbol{u}(t_o)$ as a *reversal point*. If there is no reversal point along a trajectory, we say that the trajectory is *reversal-free*. This "definition" itself suggests a straightforward procedure for finding the reversal points along a given trajectory in the task space. Plotting and counting reversal points along specified trajectories is a one way to visualize or to compare the characteristics of the kinematics of machine tools.

4.3.1.2 Reversal-singular Points and Strong Reversal-Singular Points

At a point $\boldsymbol{u} \in U$ in the task space U, if there is an integer $k \in \{1, 2, ..., N\}$ such that

$$\nabla f_k \equiv \left[\frac{\partial f_k}{\partial u_1}, \frac{\partial f_k}{\partial u_2} \cdots \frac{\partial f_k}{\partial u_M}\right] = 0, \tag{27}$$

the point $\boldsymbol{u}$ is referred to as a *reversal-singular point* with respect to the *k*th actuator, where f_k is the *k-th* component of the inverse kinematics f. A reversal singular point with respect to the *k-th* actuator is said to be *strong* if the Hessian $[h^k_{ij}]$ of the *k-th* component f_k of the inverse kinematics f is definite at the point, where

$$h^k_{ij} \equiv \frac{\partial^2 f_k}{\partial u_i \partial u_j}. \tag{28}$$

At a strong reversal singular point with respect to the *k-th* actuator, the *k-th* actuator displacement f_k is either local maximum or minimum. Therefore, the *k-th* actuator must reverse its direction of motion at the strong reversal-singular point.

Observation 1 When the fiducial point of a machine tool passes a strong reversal singular point with respect to the k-th actuator, the reversal of the k-th actuator is not avoidable.

Reversal singular points, not necessarily strong, also imply a "high" chance of reversals because the trajectories passing a reversal-singular point should satisfy a very special condition for reversal-free motion. This is especially easy to be understood in 2 dimensional task space. If a reversal singular point in a 2 dimensional task space with respect to the *k-th* actuator is not strong, the *k-th* component f_k of the inverse kinematics has a saddle point in the reversal singular point.

Observation 2 At a non-strong reversal singular point in a 2 dimensional task space, a trajectory must be tangential to one of the separtix of the function f_k if it is reversal-free. In high dimensional spaces, we can make a similar statement.

This is a very special condition which is rarely satisfied especially in the sweeping tasks, which we discuss in Section 4.3.3. Plotting the reversal singular points is a rather canonical way to visualize the reversal characteristics of machine tools because it does not depend on a particular trajectory we choose.

4.3.1.3 Reversal Free Directions in the Tangent Space of the Task Space

We can also specify a reversal condition in terms of tangent vectors of trajectories. We also define related terms for future use in this section.

If a cutting tool moves obeying the given task constraints, the "velocity" $\dot{\theta}$ of the actuators and the "velocity" $\dot{\boldsymbol{u}}$ in the task space have the following linear relation:

$$\dot{\theta} = \boldsymbol{C}\dot{\boldsymbol{u}} \tag{29}$$

where $\boldsymbol{C}$ is the Jacobian matrix of the restricted inverse kinematics f. The M-tuple $\dot{\boldsymbol{u}}$ is an element of the tangent space of the task space. The *tangent space* at a point $\boldsymbol{u} \in U$ is denoted by $T_{\boldsymbol{u}}U$. The union of tangent spaces is referred to as the *tangent bundle*, and symbolically as TU.

At every point in the task space at an instant, each actuator has 2 alternatives, either increasing or decreasing its displacement, namely either $\dot{\theta}_i \geq 0$ or $\dot{\theta}_i \leq 0$.[†] Such cases can be encoded using a binary system; for example, in a 5-axis machine tool, if its first and the last actuator displacements increase and the other displacements decrease, we denote the case by $(1, 0, 0, 0, 1)$, which we refer to as an *actuator permutation*. The number of possible actuator permutations is 2^N, where N is the number of actuators. In other words, an actuator permutation p imposes N inequalities in the tangent space $T_{\boldsymbol{u}}U$ at a given point $\boldsymbol{u} \in U$; each inequality can be thought of as a half space in the tangent space. The intersection of such half spaces forms a simply-connected cone in the tangent space. The resulting cone is referred to as the *p-th (reversal-free) cone* of a given point $\boldsymbol{u} \in U$, and symbolically as $C^p_{\boldsymbol{u}}U$. We say that $C^p_{\boldsymbol{u}}U$ is *void* if $C^p_{\boldsymbol{u}}U = \{\boldsymbol{0}\}$, and $C^p_{\boldsymbol{u}}U$ is *degenerate* if $C^p_{\boldsymbol{u}}U$ is a set of measure zero. An entire task space can be partitioned into two regions depending on whether the *p-th* reversal-free cone is degenerate or not. The set of points of non-degenerate *p-th* cone is referred to as the *p-th plate*, and symbolically, as P^p. Especially in a 2 dimensional tangent space, a reversal free cone is bounded by 2 rays emitted from the origin of the tangent space; the one is referred to as the *right ray* and the other is referred to as the *left ray* where "right" and "left" is determined by the view from the inside of the cone. By normalizing the right rays and the left rays in a plate into unit vectors, we can form corresponding unit vector fields in the plate. They are referred to as the *right* and the *left vector field*, respectively; symbolically as $V^p_R U$ and $V^p_L U$. The complementary permutation of an actuator permutation p is defined as the permutation generated by reversing the signs of the corresponding inequalities and denoted by $-p$. For example, if $p = (1, 0, 0, 0, 1)$, then $-p = (0, 1, 1, 1, 0)$.

Example: A Reversal Free Cone

Consider finish machining a parabolic surface parameterized by

$$x = u + 2v,\ y = u - v \text{ and } z = u^2 + 2v^2 + 2uv \tag{30}$$

using a 3-axis Cartesian machine tool; the tool tip is constrained in the surface. In this case, the

---

[†] The case, $\theta_i = 0$, is considered to be either one of the cases.

inverse kinematics map f is simply:

$$f : U \rightarrow \Theta,\ \ (u, v) \rightarrow (\theta_1, \theta_2, \theta_3) = (u + 2v,\ u - v,\ u^2 + 2v^2 + 2uv) \tag{31}$$

where we regard the uv-parameter space of the surface as our task space. We will derive the *p-th* reversal-free cone at $(1/2, 1/2) \in U$ in this example, when $p = (1, 0, 1)$.

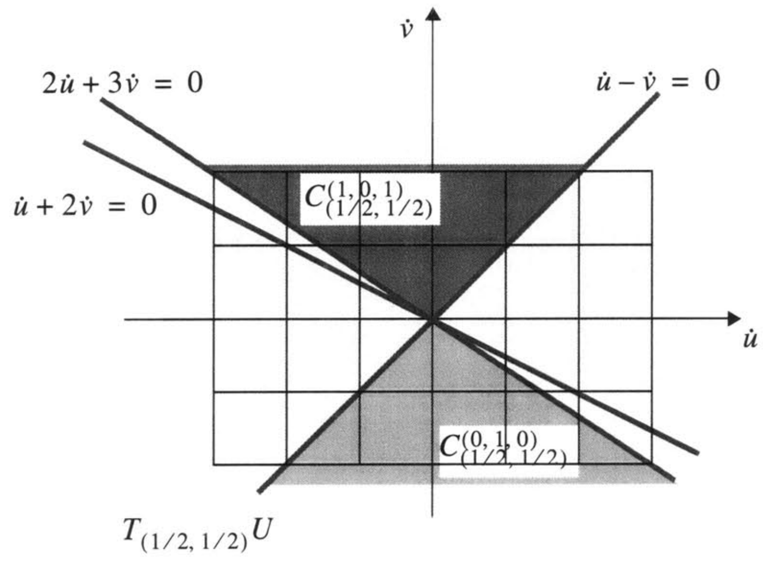

(a) A Reversal Free Cone and its complement

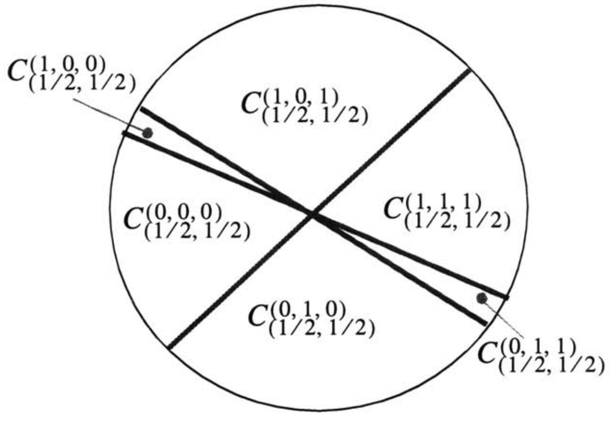

(b) $\bigcup_p C^p_{\mathbf{u}} = T_{\mathbf{u}} U$

Figure 12 A Reversal Free Cone

The Jacobian matrix $\boldsymbol{C}$ of the inverse kinematics is derived by differentiation:

$$\boldsymbol{C} = \begin{bmatrix} 1 & 2 \\ 1 & -1 \\ 2u+2v & 4v+2u \end{bmatrix} . \tag{32}$$

Especially, the Jacobian matrix at $(u, v) = (1/2, 1/2) \in U$ is $[1\ 2; 1\ -1; 2\ 3]$. When the actuator permutation is $(1, 0, 1)$, the inequalities imposed on the tangent space at $(1/2, 1/2) \in U$ are:

$$\dot{u} + 2\dot{v} \geq 0 \text{ , } \dot{u} - \dot{v} \leq 0 \text{ and } 2\dot{u} + 3\dot{v} \geq 0 \text{ .} \tag{33}$$

Formally, we can write:

$$C^{(1,0,1)}_{(1/2,1/2)} = \{(\dot{u}, \dot{v}) \mid \dot{u} + 2\dot{v} \geq 0, \dot{u} - \dot{v} \leq 0, 2\dot{u} + 3\dot{v} \geq 0\} \subset T_{(1/2,\,1/2)}U \tag{34}$$

and a graphical representation is given in Figure 12-(*a*). As shown in Figure 12-(*b*), the union of the reversal-free cones at a point covers an entire tangent space at the point. In the figure, the ray defined by $\dot{u} - \dot{v} = 0$ is the right ray of the cone $C^{(1,0,1)}_{(1/2,1/2)}$, and the ray, $2\dot{u} + 3\dot{v} = 0$, is its left ray.

Observation 3 We can state the following immediate consequences:

(1) If a trajectory $\boldsymbol{u}(t) \in U$ is reversal-free, its velocity vector $\dot{\boldsymbol{u}}(t) \in T_{\boldsymbol{u}(t)}U$ must stay in a reversal free cone for an actuator permutation; namely there should be an actuator permutation p such that $\dot{\boldsymbol{u}}(t) \in C^p_{\boldsymbol{u}(t)}U$ for all t for reversal free motion.

(2) At a regular point $\boldsymbol{u}$, $C^p_{\boldsymbol{u}}U$ and $C^{-p}_{\boldsymbol{u}}U$ are axi-symmetric in $T_{\boldsymbol{u}}U$. In particular, $C^p_{\boldsymbol{u}}U = \{\boldsymbol{0}\}$ iff $C^{-p}_{\boldsymbol{u}}U = \{\boldsymbol{0}\}$; $C^{-p}_{\boldsymbol{u}}U$ is degenerate iff $C^p_{\boldsymbol{u}}U$ is degenerate.

(3) At a regular point $\boldsymbol{u}$, $\mathrm{U}_p C^p_{\boldsymbol{u}} = T_{\boldsymbol{u}}U$, namely, the tangent space at a point is covered or "tiled" by the reversal-free cones at the point.

(4) At a point $\boldsymbol{u}$ on the boundary of a plate, P^p, the corresponding reversal-free cone $C^p_{\boldsymbol{u}}U$ is degenerate except for some special isolated points, which are reversal singular points.

(5) The pth right vector field $V^p_R U$ and the *p-th* left vector field $V^p_L U$ are continuous in each component of P^p except at the reversal singular points. The vector field $\alpha V^p_R U + (1 - \alpha) V^p_L U$ is continuous and its value at any point $\boldsymbol{u} \in P^p$ belongs to the cone $C^p_{\boldsymbol{u}}U$, where α is a continuous function on U whose range is the interval $[0, 1] \subset R$.

(6) $P^p = P^{-p}$.

4.3.2 Reversals in Point to Point Tasks

Given two end points in the task space, a point-to-point task is to find a trajectory that connects the two end points satisfying certain conditions. We can make the following general statement in the actuation space:

Observation 4 For given two points in an actuation space, the straight segment that connects the two points is a reversal-free path if the segment stays in the actuation space. Especially, if the actuation space is convex, any two points in the actuation space can be connected without any reversal.

However, in a task space, the problem is not trivial. For a task space, what we can assure is, at most, a negative statement:

Observation 5 Any periodic path in the task space must have reversal points,

which does not answer our original question: whether a given pair $(\boldsymbol{u}_o, \boldsymbol{u}_1)$ of points in the task space can be connected without any reversals by a trajectory staying in the task space. To answer the question, we construct the set of points which can be reachable without any reversal from one of the given points, $\boldsymbol{u}_o$. The resulting set is referred to as the *(reversal-free) reachability set* of the point $\boldsymbol{u}_o$ and symbolically as $F_{\boldsymbol{u}_o}$. If the other point $\boldsymbol{u}_1$ belongs to the reversal-free reachability set $F_{\boldsymbol{u}_o}$, we can conclude that the pair of points, $\boldsymbol{u}_o$ and $\boldsymbol{u}_1$, can be connected in a reversal free manner. The following observation is also useful in this regard:

Observation 6 If it is possible to connect two points with a reversal-free path, there must be a plate to which both points belong.

Plotting reversal-free reachability sets is also a good means of visualizing the reversal characteristics of machine tools. In a high dimensional task space, finding a reversal-free reachability set of a point is computationally-intensive. However, the problem can be dealt with effectively in a 2 dimensional task space in a heuristic manner. Here, we show how we can visualize the reversal-free reachability set of a given point $\boldsymbol{u}_o \in U$ in a 2 dimensional task space U. Consider the set of points which are reachable from a point $\boldsymbol{u}_o \in U$ by a trajectory $\boldsymbol{u}(t) \in U$ while the velocity $\dot{\boldsymbol{u}}(t)$ of the trajectory stays in the *p-th* reversal-free cones $C^p_{\boldsymbol{u}(t)}$ along the trajectory. The resulting set is referred to as a *p-th (reachability) leaf* of the point $\boldsymbol{u}_o$ and, symbolically, as $F^p_{\boldsymbol{u}_o}$.

Observation 7 The following properties of reachability-leaves is immediate from the definition:

(1) A reachability leaf is *path-connected.*

(2) $F^p_{\boldsymbol{u}_o} - \{\boldsymbol{u}_o\} \subset P^p$.

(3) $\boldsymbol{u} \in F^p_{\boldsymbol{u}_o}$ implies that $F^p_{\boldsymbol{u}} \subset F^p_{\boldsymbol{u}_o}$ and $\boldsymbol{u}_o \in F^{-p}_{\boldsymbol{u}_o}$.

(4) $F_{\boldsymbol{u}_o} = \mathrm{U}_p F^p_{\boldsymbol{u}_o}$, namely, the reversal-free reachability set of a point can be constructed simply as the union of its leaves.

Consequently, the problem is reduced to finding the reachability-leaves of a given point and we need to show how to attain a leaf $F^p_{\boldsymbol{u}_o}$ of a point $\boldsymbol{u}_o$ in a 2 dimensional task space U. If the start point $\boldsymbol{u}_o$ does not belong to the plate P^p, namely $\boldsymbol{u}_o \notin P^p$, we simply terminate the procedure because $F^p_{\boldsymbol{u}_o} - \{\boldsymbol{u}_o\} \subset P^p$ and $F^p_{\boldsymbol{u}_o}$ is a path-connected set. Henceforth, we consider only the case of $\boldsymbol{u}_o \in P^p$.

We integrate the *p-th* right vector field from the start point. The integral line, which we denote by L_R, must meet the boundary of the plate P^p at a point r. In the same manner, we define the intersection point l between the integral line L_L of the left vector field and the plate. This is shown in Figure 13-(a). We construct the reachability leaf by connecting the two end points.

Observation 8 The cone at r *and the cone at* l *are degenerate if they are not reversal singular points because they are on the boundary of the plate. The directions of the corresponding cones,* $C^p_r U$ *and* $C^p_l U$*, are parallel to the integral lines* L_R *and* L_L*, respectively. The directions must be towards the outside of the plate.*

We march along the boundary from the point r to the left. During the march, we observe the

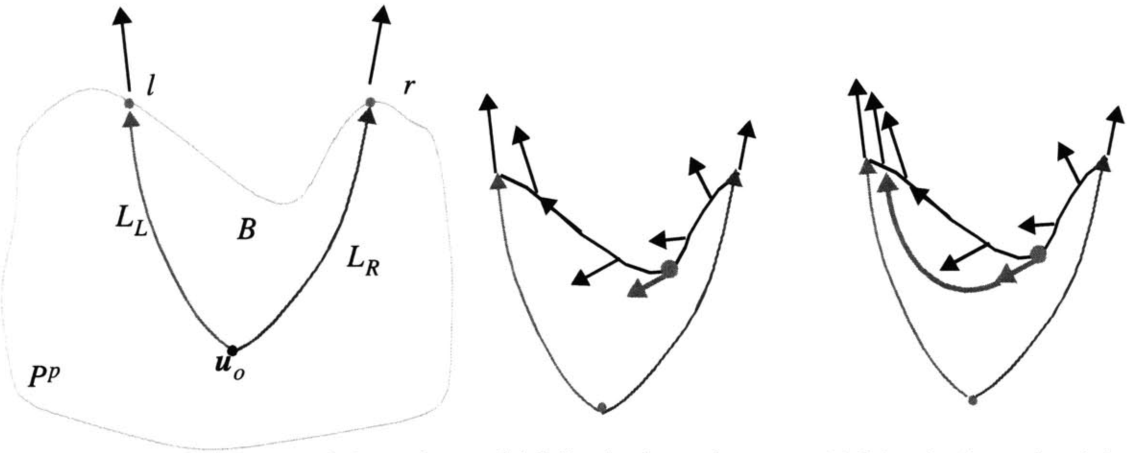

(a) Integration along the right and the left vector field.

(b) March along the boundary.

(c) March along the right vector field.

Figure 13 Constructing a Reachability Leaf

degenerate cone along the boundary. At the beginning, the cone is directed towards the outside of the plate. At some instant during the march, there is a chance that the cone on the boundary directs toward the inside of the plate as shown in Figure 13-(b). If so, at that point, we march along integral line of the right vector field as shown in Figure 13-(c). The integral line must hit the boundary of the plate. Then, we march along the boundary again. This march is continued until the march hits the point l or it forms a loop. We do the same procedure from the left to the right. The most inside marched lines together with the original integral lines form a boundary of the reachability leaf.

This heuristics worked in most cases. However, the existence of the reversal singularities or holes inside the plate hinders the universality of the marching procedure. In that case, we adopted a rather brute-force procedure: we integrated the vector field $\alpha V_R^p U + (1-\alpha) V_L^p U$ from the starting point for various values of α. On the other hand, we can prove that the above heuristics find correct reachability leaves for a special but common situation.

Observation 9 Suppose that the points, r and l, which are the end points of the first two integral lines in the marching procedure, are on the most outside boundary loop of the component of the plate which the starting point $\boldsymbol{u}_0$ belongs to. Let B be the region bounded by the two integral lines, L_L and L_R, together with the segment of the boundary of the plate that connects the two points, r and l, from r to l counter-clockwise. If the region, B, contains no holes and reversal-singular points, the marching procedure given above finds the reachability leaves correctly.

4.3.3 Modeling Surface Machining with Vector Fields

The objective of finishing is to sweep a 2 dimensional manifold. If we assume that the orientation of a cutting tool is pre-determined, the task space dimension is 2, for the finishing process. We can capture the family of sweeping paths with a vector field. More rigorous treatment of this model can be found in [28].

A surface in the workspace of a machine tool can be specified in a parametric form, $\boldsymbol{r}(u, v)$, where $\boldsymbol{r}$ is a regular map from the uv-parameter space of the surface, which we think of as the 2 dimensional task space U, to the Cartesian workspace W. We require that the tool tip be constrained in the surface and that the orientation is pre-determined.

A vector field on the task space, which captures a family of streamlines, can be specified with a continuous mapping,

$$\dot{\boldsymbol{u}} : U \rightarrow TU, \quad \boldsymbol{u} \rightarrow \dot{\boldsymbol{u}}(\boldsymbol{u}) \equiv [\dot{u}(u, v) \quad \dot{v}(u, u)]^T \in T_{\boldsymbol{u}} U.$$

In this setting, we regard that tool paths are chosen only from the streamlines of the given vector field. Now, given a vector field $\dot{\boldsymbol{u}}(\boldsymbol{u}) \equiv [\dot{u}(u, v) \quad \dot{v}(u, u)]^T$ on the task space U, the candidate for the points in the task space where the *k-th* actuator reverses its direction, can be determined by solving the following equation:

$$\dot{\theta}_k \equiv \frac{\partial f_k}{\partial u} \cdot \dot{u} + \frac{\partial f_k}{\partial v} \cdot \dot{v} = c_{k1}(u, v) \cdot \dot{u}(u, v) + c_{k2}(u, v) \cdot \dot{v}(u, v) = 0 \tag{35}$$

which defines a curve in the task space, where c_{ij} are known as the Jacobian matrix of the inverse kinematics. We call those lines *reversal lines* of the vector field, which is also a visualization tool for the reversal characteristics of a machine tool. In a higher dimensional task space, the equation defines a hyper-surface.

The reversal singularities have a stronger implications for sweeping tasks.

Observation 10 When we sweep a surface, the reversal of actuators is not avoidable once there appears a strong reversal singular point in the task space no matter what vector field is assigned to sweep the surface. If a streamline of a sweeping passes a reversal singularity, not necessarily strong, with respect to the kth actuator without any reversals, the streamline must be tangential to one of the separtix of the function $f_k(u, v)$. *This is a very special condition which is rarely satisfied.*

Therefore, once a reversal singular point appears in a task space, the corresponding actuator reverses its motion at the reversal singular point almost surely; plotting the reversal singular points is a rather canonical way to visualize the reversal characteristics of sweeping tasks because it does not depend on the vector field we choose.

We now ask a question in the positive direction and answer it:

Observation 11 If there is no reversal singular points in a task space and a plate P^p *covers the task space, we can cover the task space with the following vector field:*

$$\alpha V_R^p U + (1 - \alpha) V_L^p U \tag{36}$$

which was mentioned in Observation 3.

An extension of this problem is to cover the task space with the minimum number of plates, which is essentially reduced to the minimum set cover problem when we discretize the problem.

4.4 Visualization for the Serial and Parallel Machines

The various concepts that were developed in the previous section can be visualized to enhance our understanding of the reversal characteristics of machine tools. In this section, we show reversal singular points, reversal lines, reversal points and reachability sets for the 2 machine tools shown in Figure 11, which, we believe, assists designers' or path planners' high level decision on the design and the use of machine tools. In addition, we explain the notions we developed in the previous section in detail with examples.

4.4.1 The Machine Tools and the Surfaces

Figure 14-(a) shows the "skeletons" of the 2 machines which are serial and parallel. Their actuators are numbered in the same figure. We consider 2 surfaces, which are specified as Bezier tensor product patches; one is a flat surface, and the other is a rather curved surface as shown in Figure 14-(b). The actual size of the surface was scaled for each machine tool so that the surface can fit into the designed workspace. For the serial machine tool, the surface was rotated about the x-axis to avoid the singularity at the vertical posture. As long as the inverse kinematics is computable, the flat surfaces were adjusted at a rather large size so that global phenomena can be observed. We assign both the surface normal and the vertical direction to the orientation. We consider the finish process whose task space is 2 dimensional. The inverse kinematics is given as a map $(u, v) \in [0, 1]^2 \rightarrow f(u, v) \in R^N$, where N is the number of actuators, and u and v are parameters used for defining the surface.

4.4.2 Reversal Singular Points

Figure 15 shows the distribution of the reversal singular points for the curved surface we are considering. There is a general tendency that the number of reversal singular points increases as the mechanism approaches the fully parallel mechanism and as the surface is curved. Especially,

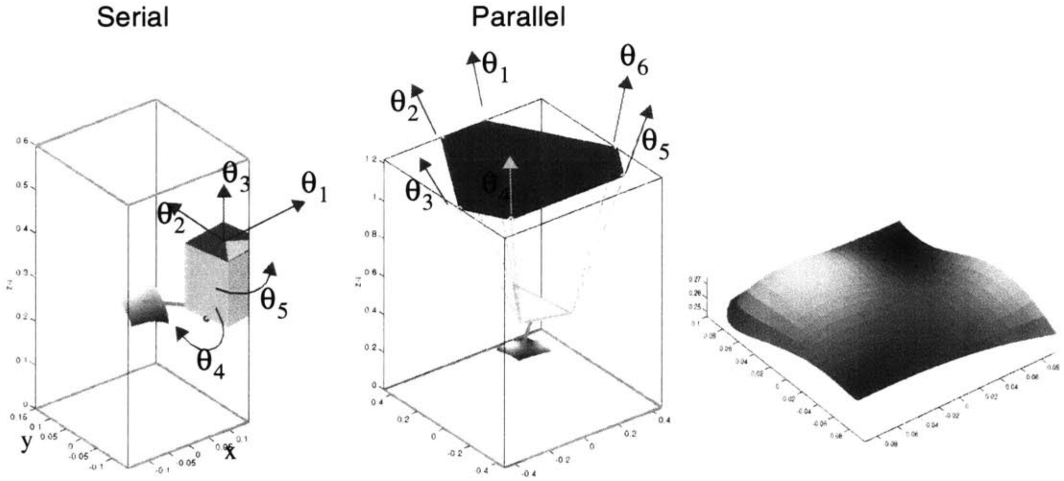

(a) The "Skeletons" of the 2 machines with the Surfaces

(b) The Curved Surface

Figure 14 Machines and surfaces

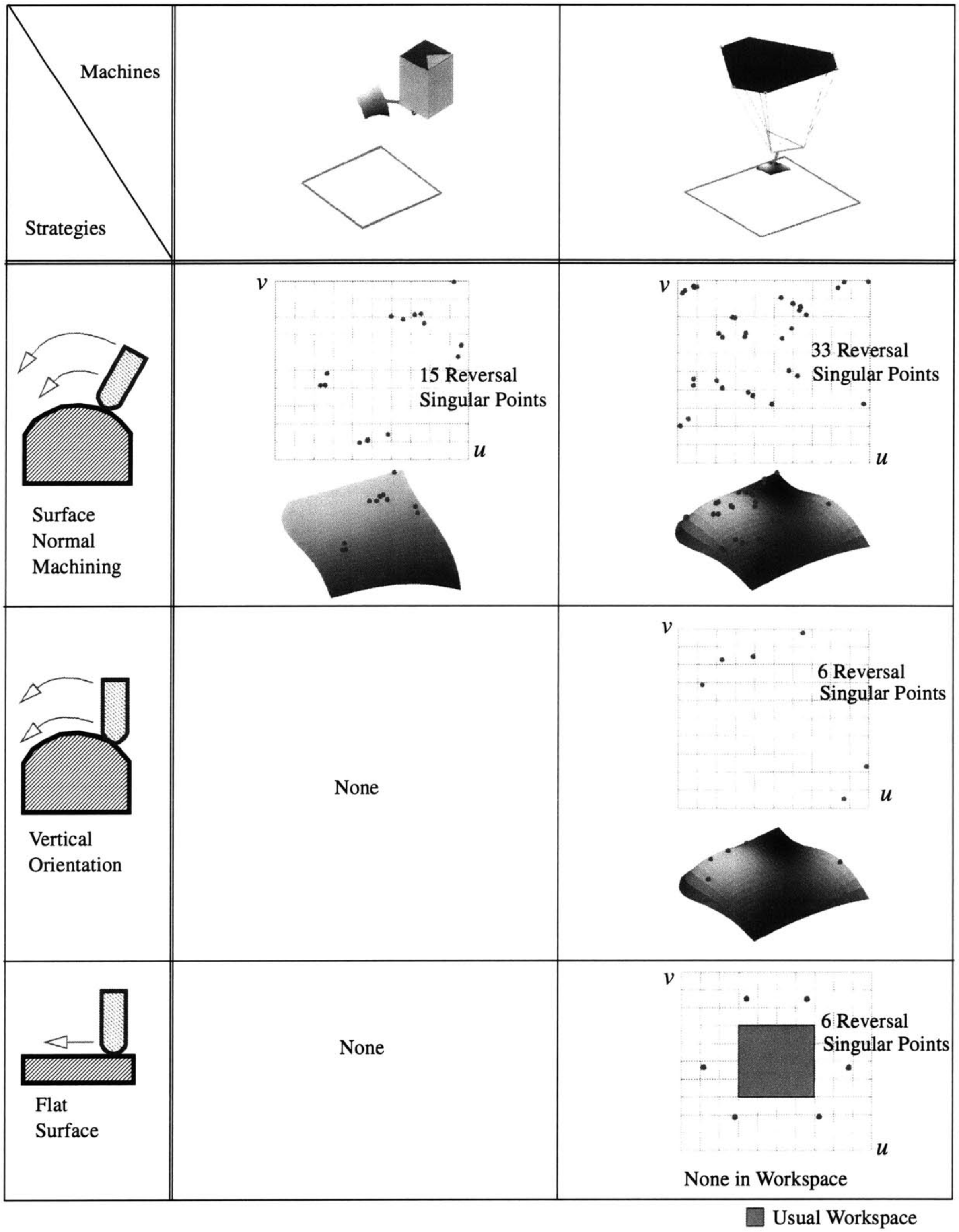

Figure 15 Distribution of reversal singular points

in surface normal machining, the swing in the orientation is the major contributor for the increase in the number of reversal singular points.

4.4.3 Reversal Points along Specified Trajectories

In Figure 16, we show reversal points along specified trajectories. Largely circular and figure 8-like curves are traced on surfaces in the workspace. It is observed that the parallel machine exhibits more number of reversal points than the serial machine. More of reversal points are found in the "figure-8" curves than the "circular" curves. The comparison between Figure 15 and Figure 16 shows that the tendency in the number of reversal singularity is well transferred to the tendency in the number of the reversal points.

4.4.4 Reversal Lines for Sweeping Tasks

Figure 17-(b) shows streamlines of a vector field we consider in this example for a sweeping task. Reversal lines with respect to an actuator are defined by Equation (35). In Figure 17-(a), we show reversal lines with respect to the first actuator of the parallel machine tool in the *uv*-parameter space, which are the bold lines; the circular markers are placed at the reversal singular points and the dashed lines are the level lines of the first component $f_1(u, v)$ of the inverse kinematics. It is observed that the reversal lines pass the reversal singular points and a level line is tangential to a streamline at each point along reversal lines. By solving the same equation for other actuators, we can visualize a complete set of the reversal lines of the sweeping task as shown in Figure 17-(c).

In Figures 18 and 19, we show reversal lines for various cases; reversal lines well represent the complexity in the reversal characteristics of machine tools. Like our previous comparisons, we observe more complex patterns of reversal lines at the fully-parallel machine. However, in the surface normal machining for curved surfaces, the disadvantage is insignificant; both of two machines show fairly complex patterns of reversals in this case. As implied by Observation 5, sweeping paths with circular patterns are more susceptible to the actuator reversals than the largely parallel sweeping paths.

We find few cases in Figure 19 for the flat surfaces, which succeed in reversal-free sweeping. They can be explained by Observation 11. For example, we consider the reversal-free sweeping of the parallel machine tool, which consists of "horizontal" sweeping paths as shown in the bottom of Figure 19. Figure 20 shows a number of sampled points in the 011100th plate and the corresponding reversal free cones therein, for the parallel machine. We find that the tangent vectors of any horizontal lines in the plate belong to the reversal free cones as shown in Figure 20. Therefore, we can sweep the 011100th plate with horizontal lines if the workspace is set as the indicated box.

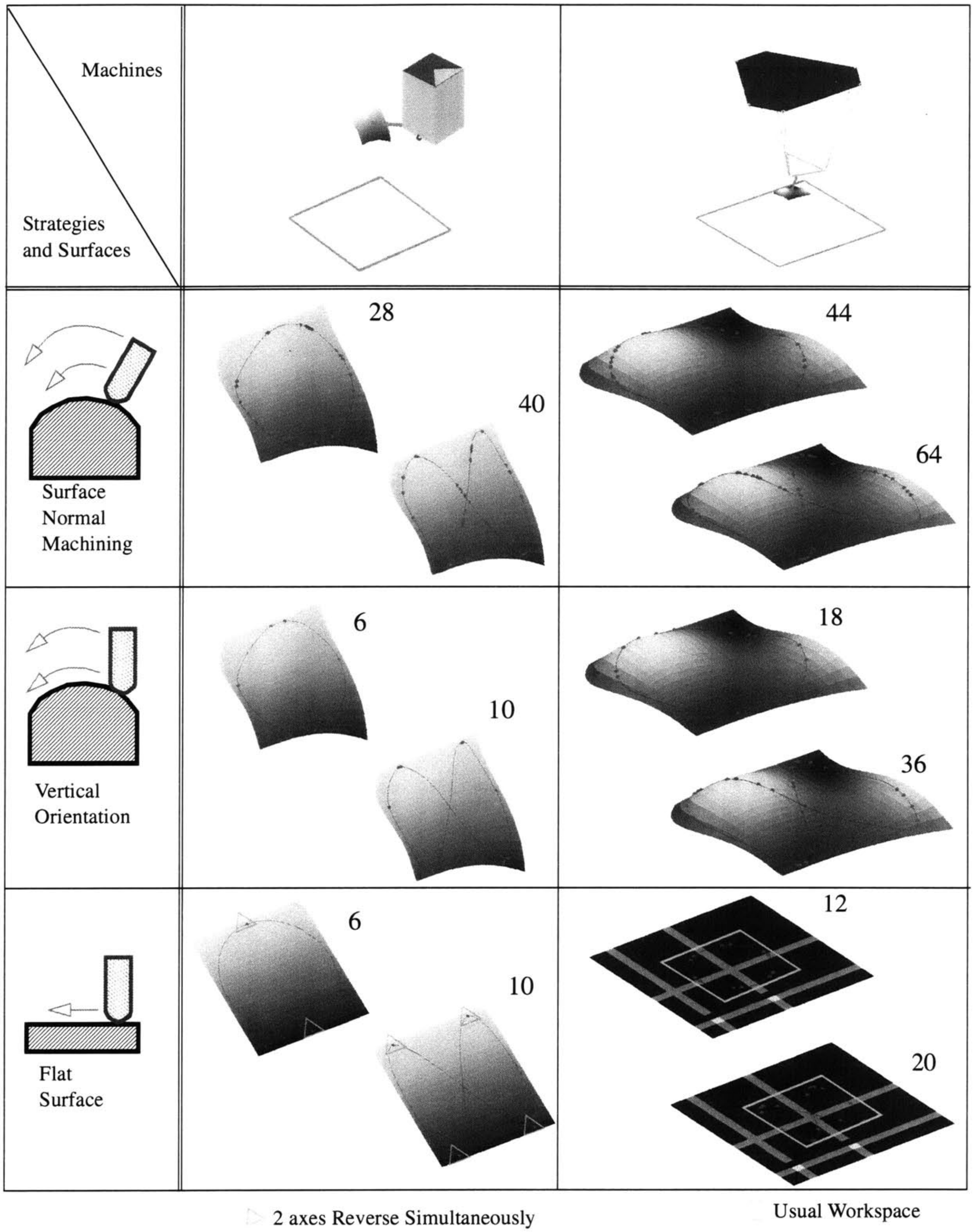

Figure 16 Reversal points along specified trajectories

4.4.5 Reversal Free Reachability Sets

We make a table of the reachability sets for all the three machines in Figure 21. It is seen that the vertical or fixed orientation produces much wider reachability set than the surface normal orientation. In the case of the flat surface, we can reach the whole workspace without any reversals with the serial machine tool. On the other hand, it is observed that the parallel machine tool can reach much smaller area of the workspace. Especially for machining a planar surface

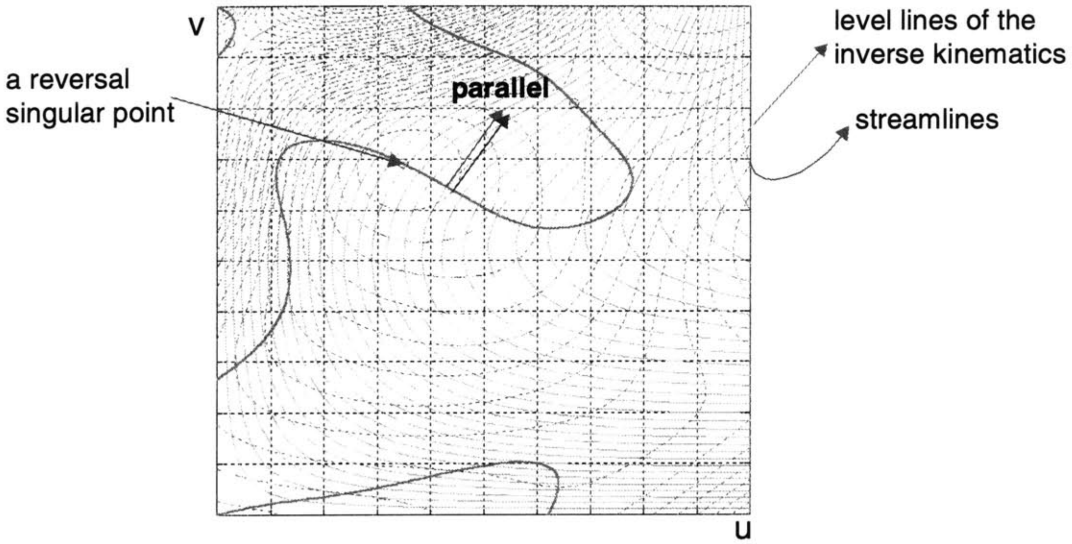

(a) Reversal lines for an actuator in the uv-parameter space

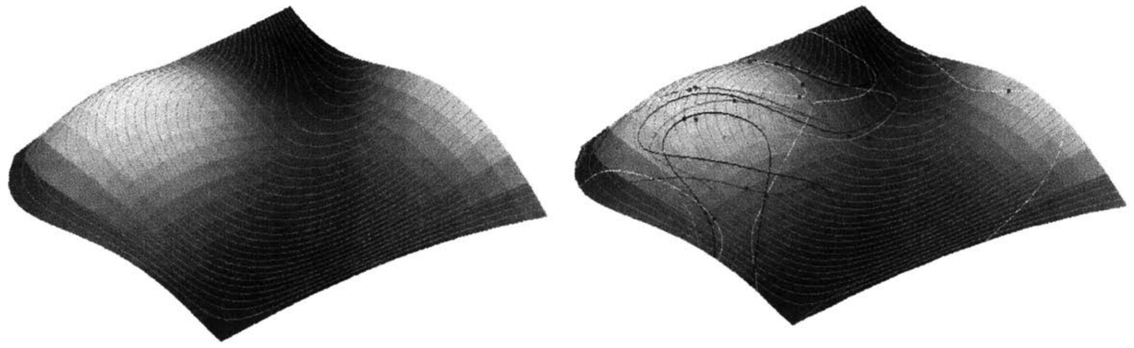

(b) The streamlines of a vector field

(c) All the reversal lines on the surface

Figure 17 Finding reversal lines for a vector field

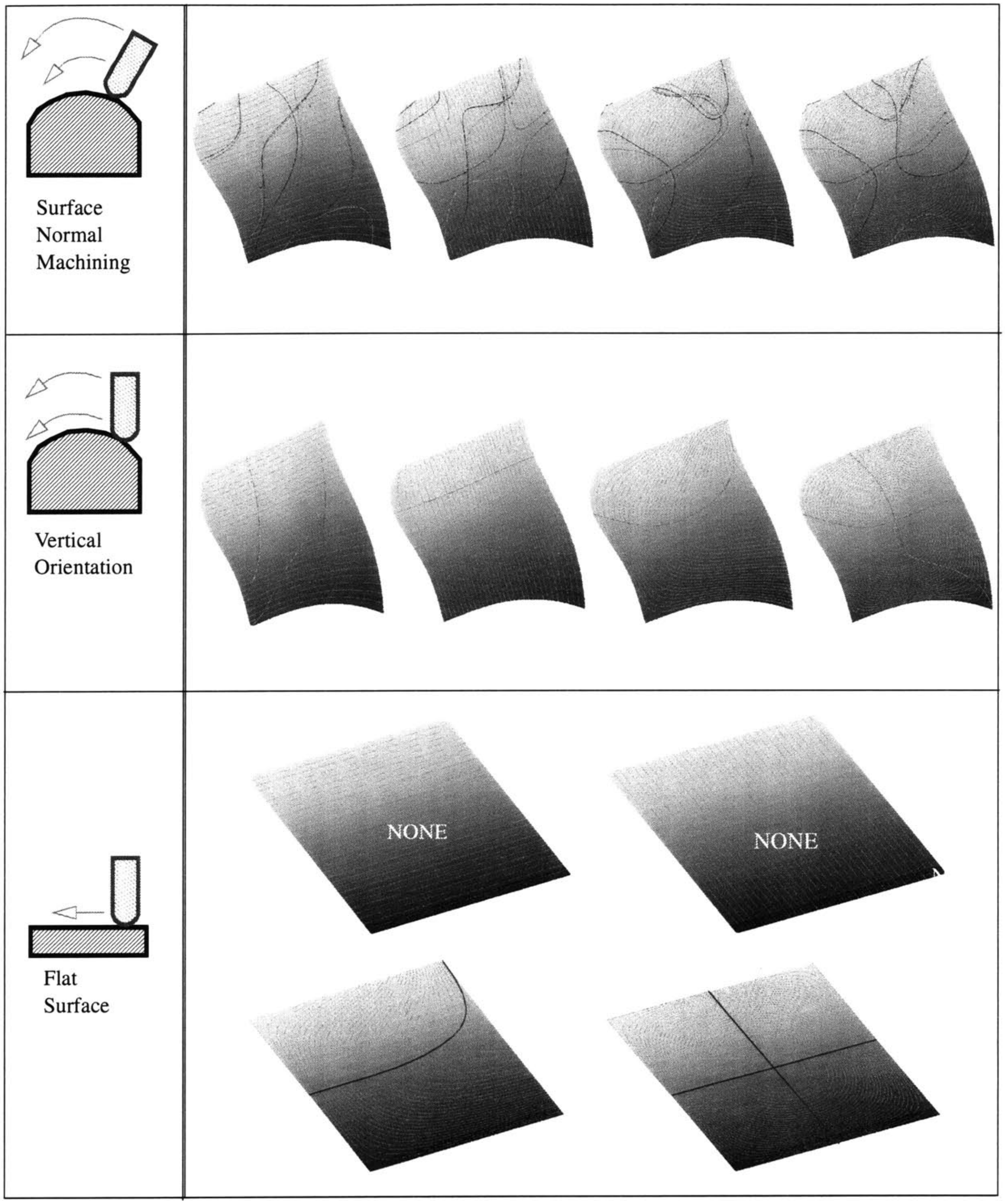

**Figure 18 Reversal lines for various cases
(Serial machine)**

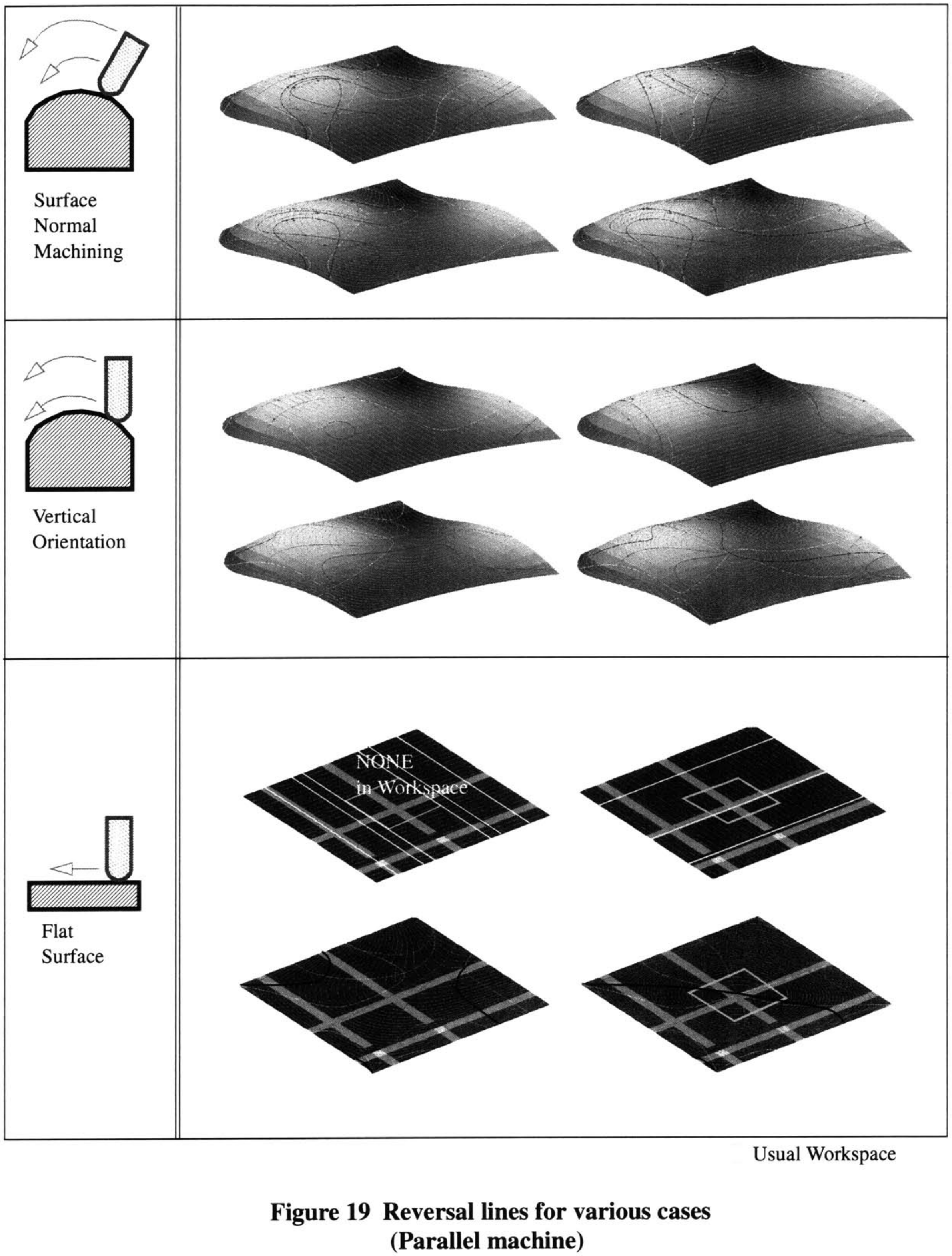

Figure 19 Reversal lines for various cases (Parallel machine)

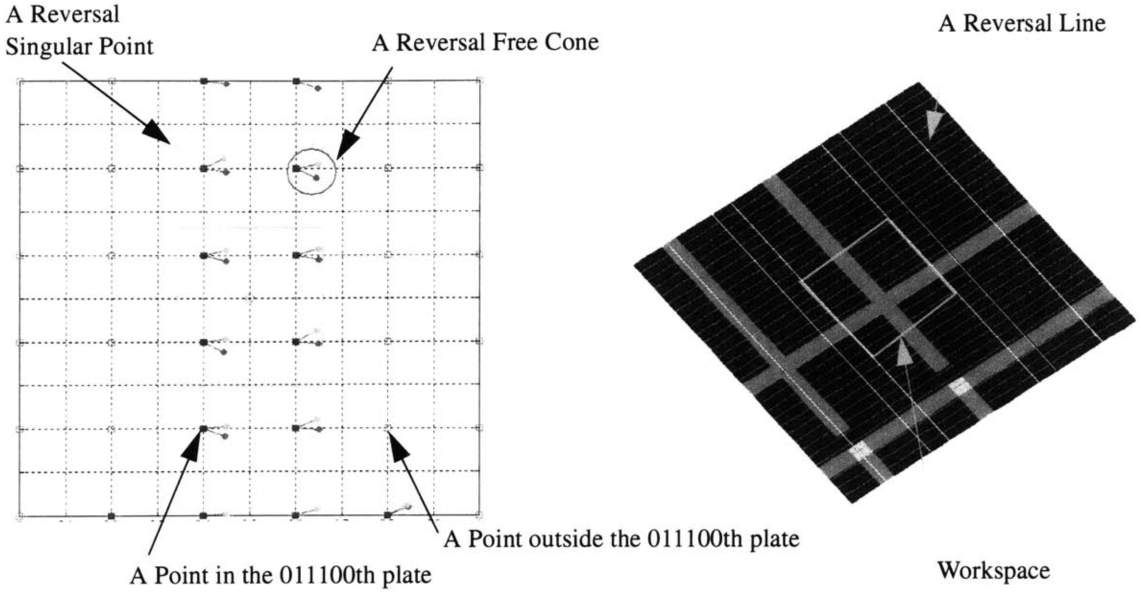

Figure 20 Reversal free sweeping

using the parallel machine tool, we can construct its reversal free reachability set using only a ruler and a compass, which is shown in Figure 22. In this figure, we do not show the construction for all the boundaries of the reachability set because of its symmetry.

4.5 Summary

In this chapter, we investigated the reversals of the relative motion in kinematic pairs of machine tools, which can generate unmodeled adverse effects such as glitches on machined surfaces. First, we developed the necessary notions, which were: reversal singular points, reversal points along specified trajectories, reversal free cones, reversal lines for a sweeping task and reversal free reachability sets. Then, we visualized them for various machine tools varying orientation patterns and the surfaces. We demonstrated that such means of visualizing reversal characteristics make predictions, consistent to each other. In addition, we briefly discussed the algorithms for the visualization and the topological properties related to the developed notions.

We conclude that the factors that increase the susceptibility of joint reversals are (1) the number of joints in the mechanism moving simultaneously (2) the "curvatures" of the inverse kinematics, (3) patterns of tool orientations and (4) the curvatures of the surfaces and the trajectories. Largely, the parallel machine tool showed relatively poor reversal behavior, especially for simple — for example, planar — geometries, compared to the serial machine. For "complex" situations — for example, if all the axes move simultaneously along a curved surface — both of machines

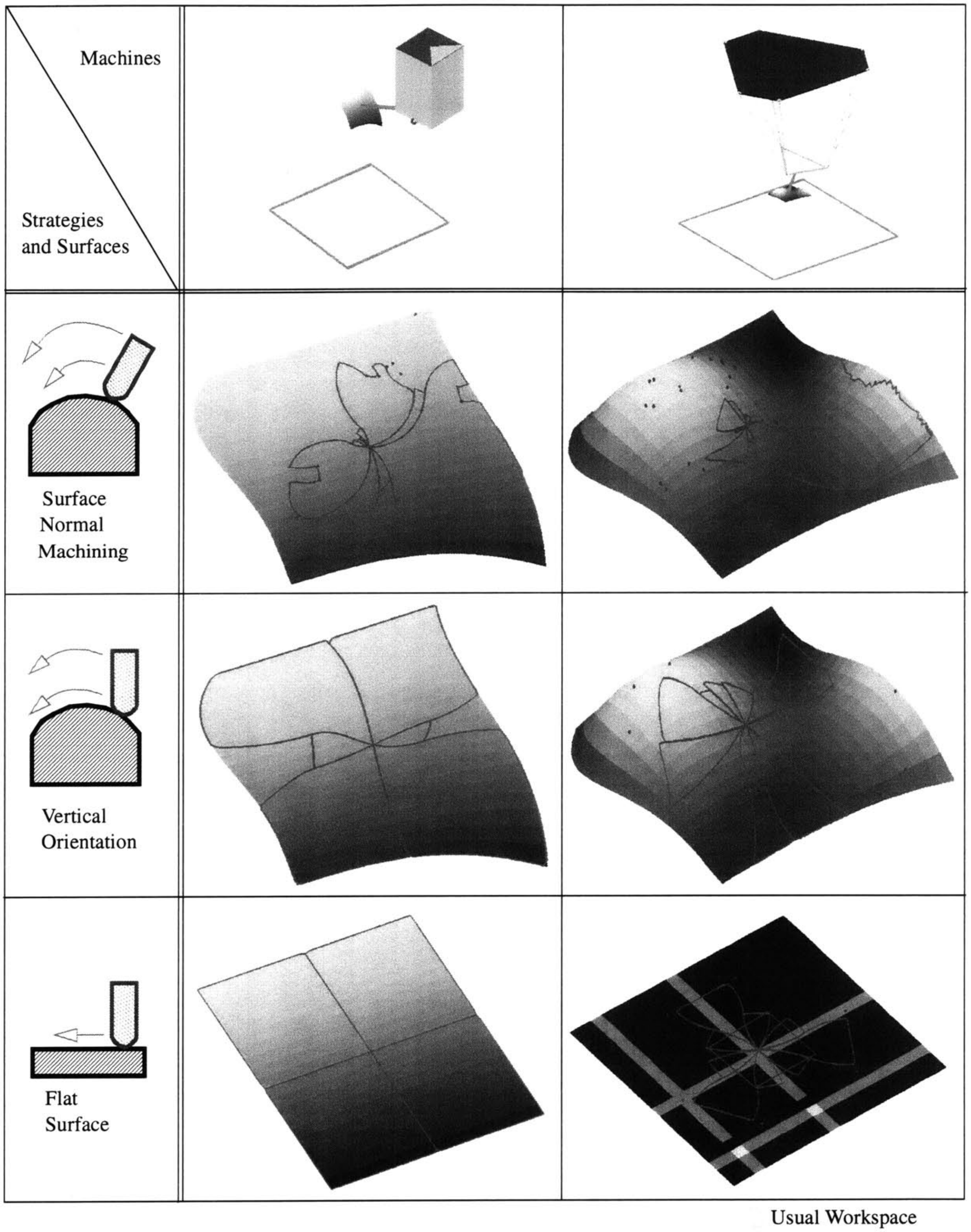

Figure 21 Reversal free reachability sets

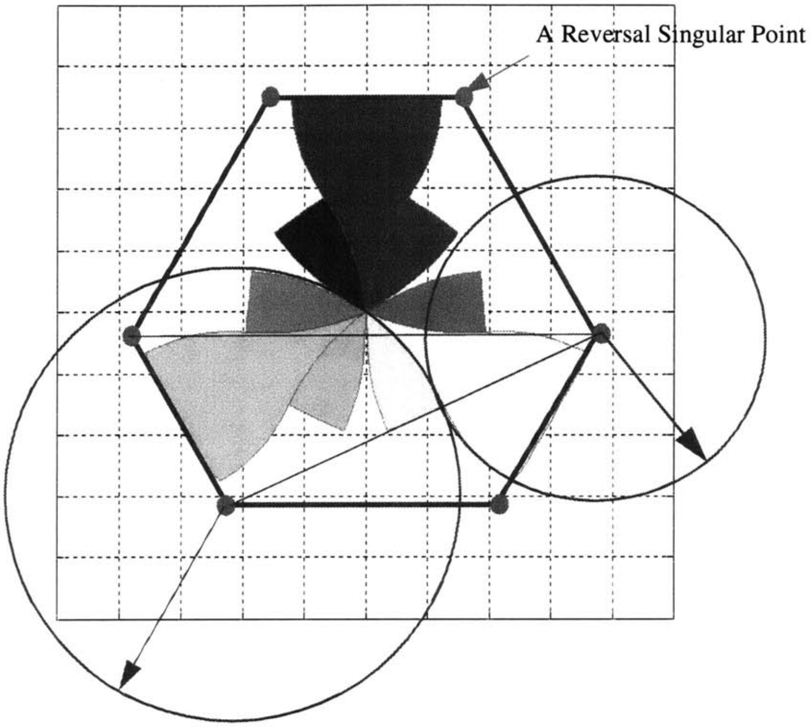

Figure 22 The construction of the reachability set for the parallel machine tool using only a ruler and a compass.

show high susceptibility for joint reversals, and the advantage or disadvantage is not sharply discerned.

5 The Hybrid Concept

We have attempted to use the advantages of both serial and parallel mechanisms in our hybrid type 5-axis CNC milling machine. We begin by listing the possible configurations and explaining our choice of machine topology.

5.1 Serial/parallel axis distribution

A 5-axis CNC milling machine requires at least 5 actuators. The hexapod has six actuators, making it more dextrous than necessary — the sixth axis is degenerate with the axis of symmetry of the rotating tool, and the extra degree of freedom is usually constrained in software. Since the cost of a machine is related to the number of actuators, the design of a hybrid 5-axis machine with 5 actuators offers an immediate potential advantage over the hexapod.

Several combinations of axis distribution for 5-axis CNC milling machines are possible, as shown in Table 1. Fully serial structures and fully parallel structures belong to Type I and Type VI respectively. The Type II structure is impractical. Therefore Types III, IV, and V are the only real candidate distributions for the 5-axes. Furthermore, we eliminate the Type III structure from consideration on the grounds that stacking 3 dof serially is very challenging. We are therefore only left with two distributions of parallel and serial axes, Types IV and V.

Parallel structures with less than 6 degrees of freedom need constraining elements which limit the mechanism in the other directions. Type V structures consist of a 1-dof serial structure and a 4-dof parallel structure which needs 2-dof constraints. Such constraining structures must be carefully designed because they may determine the overall stiffness of the parallel structure. A 4-dof parallel structure using a passive constraining leg was introduced in [64]. The overall stiffness depends critically on the passive leg which is intended to resist bending and twisting moments, and the passive leg must be large enough to achieve the required structural stiffness. On the other hand, Type IV structures are attractive because experience with 3-axis machines shows that a serial 2-axis stack-up can be achieved without significantly enlarging the structure.

	Type I	Type II	Type III	Type IV	Type V	Type VI
Serial	5	4	3	2	1	0
Parallel	0	1	2	3	4	5
Total dof	5	5	5	5	5	5

Table 1: Potential hybrid configurations

We can therefore limit our search to Type IV structures.

Amongst Type IV structures, where 3-dof are attained with a parallel structure and 2-dof are attained serially, the next question is which of the three translational and two rotational degrees of freedom must be assigned to the serial and parallel components of the machine, respectively. One option is to place both the rotational degrees of freedom on the serial mechanism. However, this leads to the problem alluded to in Section 2.1.2: from an engineering point of view, the stack-up of two revolute pairs in a machine tool requires that one of the two be a *C-axis*, which leads to kinematic singularities. Stacking an *A-axis* and a *B-axis* one on top of another is challenging because each structure is large by itself. We therefore conclude that a workable combination of the 5 degrees of freedom, based on our analysis, is a Type IV structure configured as shown in Figure 23-(a).

Given that we intend to avoid higher degree joints, the best way to achieve two translational and one rotational degree of freedom in a parallel mechanism is through a planar mechanism which is also greatly facilitated by the configuration in Figure 24. The machine layout then is reduced to the form shown in Figure 23-(b): the planar mechanism delivers 3-dof in the plane, and the serial mechanism below delivers the two out-of-plane motions. Assuming that this can be engineered, we have achieved a configuration which avoids a 3-axis serial stack-up by using a parallel mechanism, and use a serial mechanism for a more manageable 2-axis stack-up.

5.2 Configuration Design

The kinematics of 3-dof planar type parallel mechanisms have been well investigated in a number of papers in the kinematics literature [12,13,34,45]. Of all the types of planar mechanisms possible, we will only consider those which use three similar actuators. In other words, we will avoid, for example, driving one degree of freedom with a linear ball-screw and two with rotary actuators. The reason for this decision is modularity. Three broad configurations remain, which are shown in Figure 24.

The 3 types of planar parallel mechanisms shown in Figure 24 are well known, and are referred to as RRR, RPR, and PRR types where the R's and P's represent rotational and prismatic joints respectively. A new consideration now enters the selection process. Cutting forces can be usually considered as disturbances with random characteristics. The reflected force of disturbances on the actuator must be small enough to achieve good tracking performance. RRR mechanisms do not satisfy this consideration for machine tool applications because they need a high gear ratio. Furthermore, they place a large bending moment in the struts in the plane, which get rid of the advantages of parallel machines. We further eliminate the RPR structure from our considerations on the grounds that it has a telescoping joint which poses limitations discussed in Section 2.3.

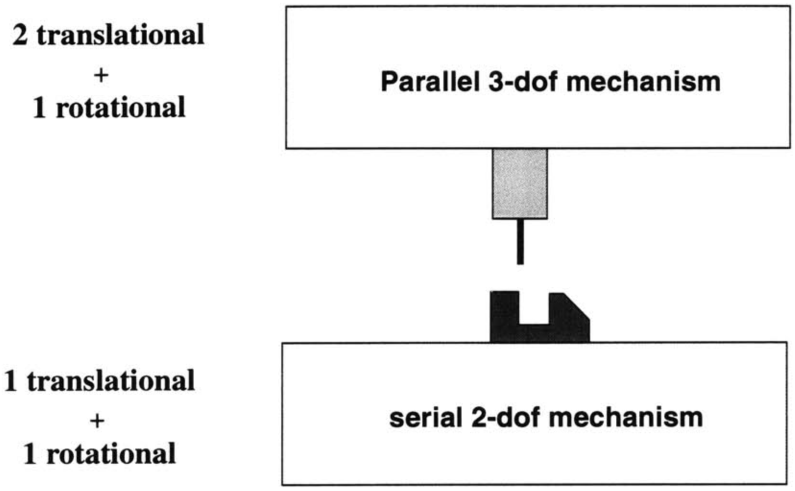

a) dof distribution

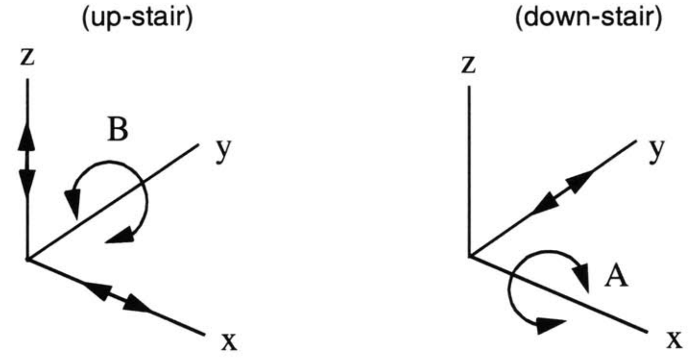

b) Axis assignment

Figure 23 Type IV structures for the MIT-SS-1

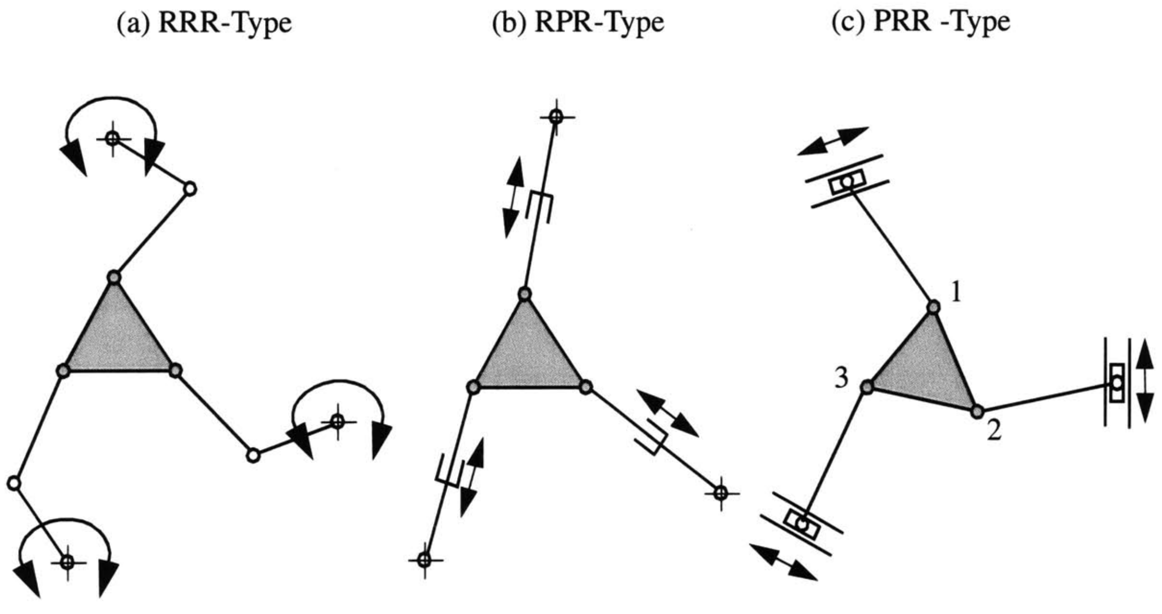

Figure 24 Planar type parallel mechanisms

Figure 24-(c) shows the remaining configurations, namely the PRR type parallel mechanism, in the context of the axis distribution discussed in the previous section. This PKM has also been pointed out by Ferreira that in a special configuration—when joints 1 and 2 in Figure 24-(c) coincide, the forward kinematics of this mechanism can also be solved in closed form [11]. We do not take advantage of this feature in our machine because the combination of these joints poses other challenges related to bearing design, and to collisions between the struts.

6 The MIT-SS-1 Hybrid Stewart Platform Machine

We have designed a 5-axis CNC milling machine (called the MIT-SS-1) based on the hybrid mechanism described previously, with the philosophy of minimizing complexity and error motions by placing the axes parallel in a plane [47]. The machine is constructed and being tested at MIT. Figures 26-(a) and 26-(b) show a solid model of the MIT-SS-1 and a working prototype. The planar parallel mechanism is installed on the vertical plane and the serial mechanism is installed on the horizontal plane. The MIT-SS-1 has been developed for small parts less than $6.0 \times 10^6 mm^3$, and the machine size is very small (0.9*m* by 1.0*m* by 1.5*m*: $W \times D \times H$). The machine frame consists of two simple rectangular blocks of solid granite. The granite has good damping and thermal stability. However, Young's modulus of granite is lower than that of materials typically used for machine tool frames, so the sections need to be massive. The frame configuration of the MIT-SS-1 is so simple that the stiffness can be enhanced simply by increasing the thickness of the granite. The vertical plane and the horizontal plane are joined by bolting which will be discussed in detail in Chapter 8. The actuators are installed on the frame so that they are not burdened with their own weights. All rails for the parallel structure are installed on the same plane—this reduces the one significant challenge posed by the planar Stewart Platform, namely over-constraint. We will analyze this problem more carefully later. Once one rail is assembled, other rails can be installed precisely, and easily, using the carriage itself as the

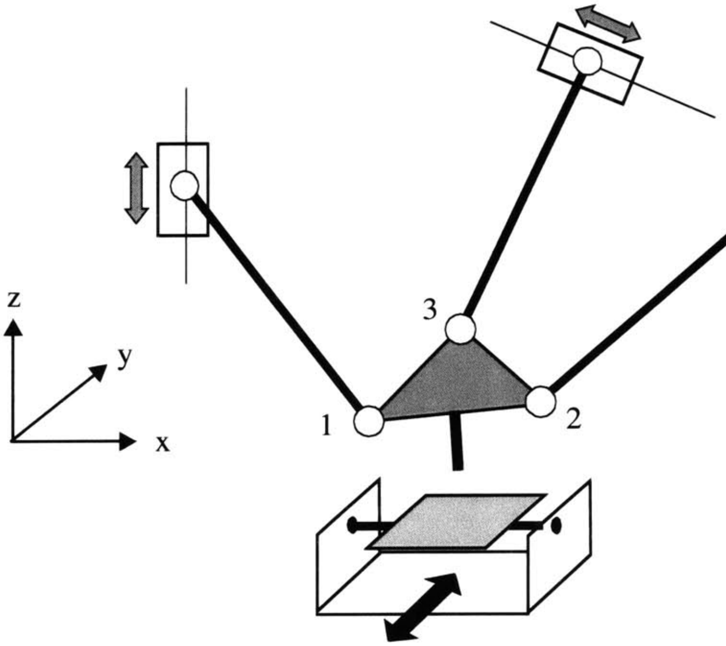

Figure 25 PRR Type Hybrid Structure

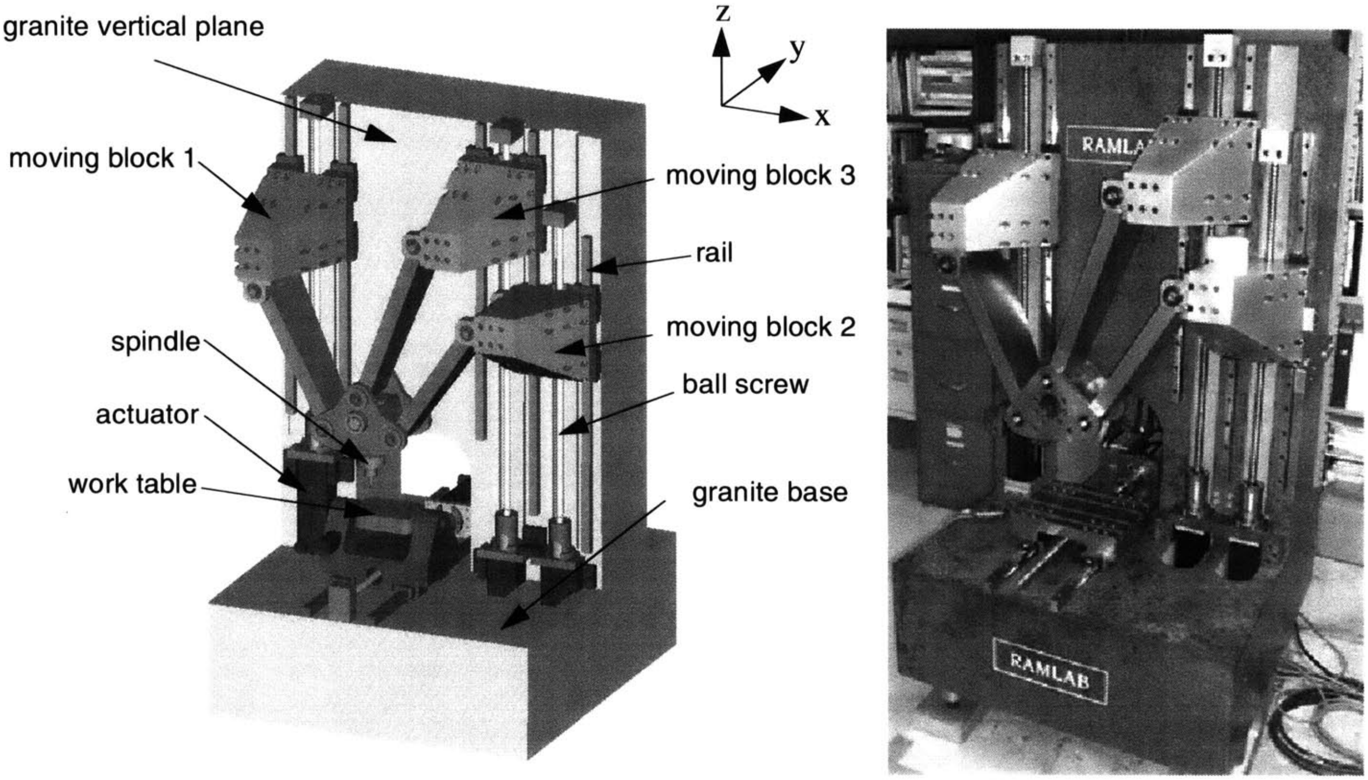

(a) Solid model of the MIT-SS-1

(b) Working prototype

Figure 26 The MIT-SS-1, PRR Type Hybrid CNC Milling Machine

fixture because all rails on the vertical plane are required to be parallel. In this way, manufacturing errors can be minimized.

Working prototype, the MIT-SS-1, as shown in Figure 26-(b) has no rotation axis about *x-axis*. We are interested in the 3-dof parallel mechanism on vertical plane because the 2-dof serial machine on horizontal plane has the same mechanism as the conventional Cartesian machine tools, and can be easily achieved by adding one rotation axis on the table, which is very common in Cartesian machine tools. The working prototype, thus, has 4 axes which include *x-,y-,z-*, and *B-axis*, and tested without *A-axis*.

In the selection of the configuration of this machine, we showed how we could avoid some important kinematic and structural problems. We now examine the inverse kinematics, the stiffness (and singularities), the workspace, the reversal characteristics and the over-constraint problem of the machine.

6.1 Kinematics

Typically, serial mechanisms have simpler forward kinematics and parallel mechanisms have simpler (but not trivial) inverse kinematics. In the MIT-SS-1, a serial mechanism as well as a parallel mechanism are incorporated. The Cartesian serial mechanism is elementary for both forward and inverse kinematics. The planar parallel mechanism as shown in Figures 26 has more complex kinematics. We derive the inverse kinematics here for control purposes. A closed form solution to the forward kinematics has not been found. Figure 27 shows the schematic diagram of the MIT-SS-1. Let θ_i be the coordinate of the *i-th* actuator. From figure 27-(a), we can derive the vector equations to get the active joint angles.

$$\vec{a}_i + \vec{z}_i = \vec{x} + \vec{m}_i + \vec{s}_i \text{ for } i = 1, 2, 3 \tag{37}$$

From Figure 27-(b), the work table coordinate, $\vec{x}^w$, can be expressed with a rotation matrix and vector relations.

$$\vec{x}^w = \bar{R}_o(\vec{x} - \vec{h}_1 - \vec{h}_2 - \vec{z}_4) \tag{38}$$

where $\vec{x}^w = \begin{bmatrix} x^w \\ y^w \\ z^w \end{bmatrix}$, $\bar{R}_o = \begin{bmatrix} 1 & 0 & 0 \\ 0 & cos(a) & -sin(a) \\ 0 & sin(a) & cos(a) \end{bmatrix}$, $\vec{x} = \begin{bmatrix} x \\ 0 \\ z \end{bmatrix}$, $\vec{h}_1 = \begin{bmatrix} 0 \\ 0 \\ h_1 \end{bmatrix}$, $\vec{h}_2 = \begin{bmatrix} 0 \\ h_2 sin(a) \\ h_2 cos(a) \end{bmatrix}$,

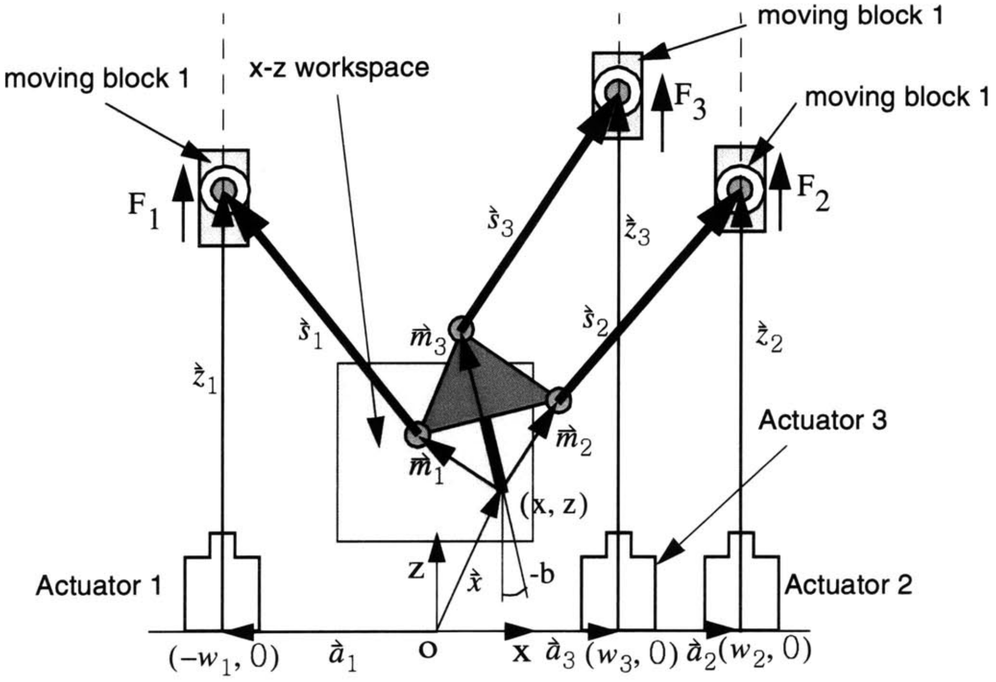

(a) A parallel structure on the vertical plane

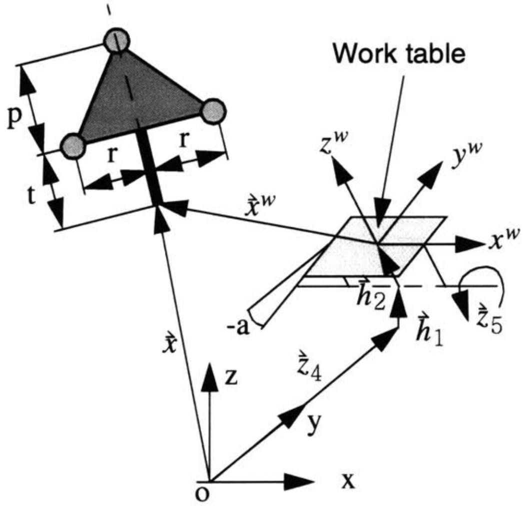

(b) A serial structure on the horizontal plane

Figure 27 Schematic of the MIT-SS-1

and $\vec{z}_4 = \begin{bmatrix} 0 \\ \theta_4 \\ 0 \end{bmatrix}$.

From Equation 38, $\vec{x}$ can be written as:

$$\vec{x} = \begin{bmatrix} x \\ 0 \\ z \end{bmatrix} = \begin{bmatrix} x^w \\ y^w cos(a) + z^w sin(a) + h_2 sin(a) + \theta_4 \\ -y^w sin(a) + z^w cos(a) + h_1 + h_2 cos(a) \end{bmatrix}. \tag{39}$$

The vectors $\vec{s}_i$, associated with the struts can be derived as following.

$$\vec{s}_1 = \begin{bmatrix} s_{1x} \\ 0 \\ s_{1z} \end{bmatrix} = \begin{bmatrix} -w_1 - x + rcos(b) - tsin(b) \\ 0 \\ \theta_1 - z - rsin(b) - tcos(b) \end{bmatrix} \tag{40}$$

$$\vec{s}_2 = \begin{bmatrix} s_{2x} \\ 0 \\ s_{2z} \end{bmatrix} = \begin{bmatrix} w_2 - x - rcos(b) - tsin(b) \\ 0 \\ \theta_2 - z + rsin(b) - tcos(b) \end{bmatrix} \tag{41}$$

$$\vec{s}_3 = \begin{bmatrix} s_{3x} \\ 0 \\ s_{3z} \end{bmatrix} = \begin{bmatrix} w_3 - x - (t+p)sin(b) \\ 0 \\ \theta_3 - z - (t+p)cos(b) \end{bmatrix} \tag{42}$$

The length of each strut, l_i, is fixed, which leads to the inverse kinematics of the MIT-SS-1. The actuator coordinates, $\theta_1, \theta_2, \theta_3$, can be expressed in terms of reference coordinates, x, z, b:

$$\theta_1 = z + rsin(b) + tcos(b) \pm \sqrt{(l_1^2 - s_{1x}^2)} \tag{43}$$

$$\theta_2 = z - rsin(b) + tcos(b) \pm \sqrt{(l_2^2 - s_{2x}^2)} \tag{44}$$

$$\theta_3 = z + (t+p)cos(b) \pm \sqrt{(l_3^2 - s_{3x}^2)} \tag{45}$$

Equations 43, 44, and 45 show that there are two roots for each actuator joint angle, which implies that a total of eight possible configurations of struts exists for each desired tool position. Figure 28-(a) shows all possible configurations for each strut. All the moving blocks must be higher than the end-effector to avoid collision with the mechanical components which are installed on the horizontal plane, which leads to only one realizable configuration.

The actuator coordinate, θ_4, along the *y-axis* can be obtained by using Equation 39. The actuator coordinate θ_5 is equal to the table orientation, $-a$ as follows:

$$\theta_4 = -y^w cos(a) - z^w sin(a) - h_2 sin(a) \tag{46}$$

$$\theta_5 = -a \tag{47}$$

Now all actuator coordinates can be expressed in terms of table coordinates. When the table coordinates are given, actuator coordinates can be easily obtained from Equations 43 to 47. Differentiating these equations with respect to time gives us the inverse Jacobian as shown below. Details are presented in Appendix B.

$$\begin{bmatrix} \dot{\theta}_1 \\ \dot{\theta}_2 \\ \dot{\theta}_3 \\ \dot{\theta}_4 \\ \dot{\theta}_5 \end{bmatrix} = J^{-1} \begin{bmatrix} \dot{x}^w \\ \dot{y}^w \\ \dot{z}^w \\ \dot{a} \\ \dot{b} \end{bmatrix} \tag{48}$$

Actuator and kinematic singularities of the MIT-SS-1 can be investigated by setting the determinant of the Jacobian and its inverse to zero respectively:

$$|J| = 0 \tag{49}$$

$$|J^{-1}| = 0 \tag{50}$$

Figure 28-(b) shows the singularity map of the MIT-SS-1 on the *x-B* workspace. Kinematic singularities occur when b is equal to $\pm 90°$, with any value of x. Solid curves in Figure 28-(b) show the actuator singularities. When the end-effector is on the solid line, the three extension lines of the struts meet at one point and the structure cannot resist a force or a moment; this is called a torque singularity. The nominal work-space is described as a shaded rectangular box. From the Figure 28-(b), we know that the workspace does not include a singularity. However, the structure loses stiffness near the singularity points, as discussed in the next section.

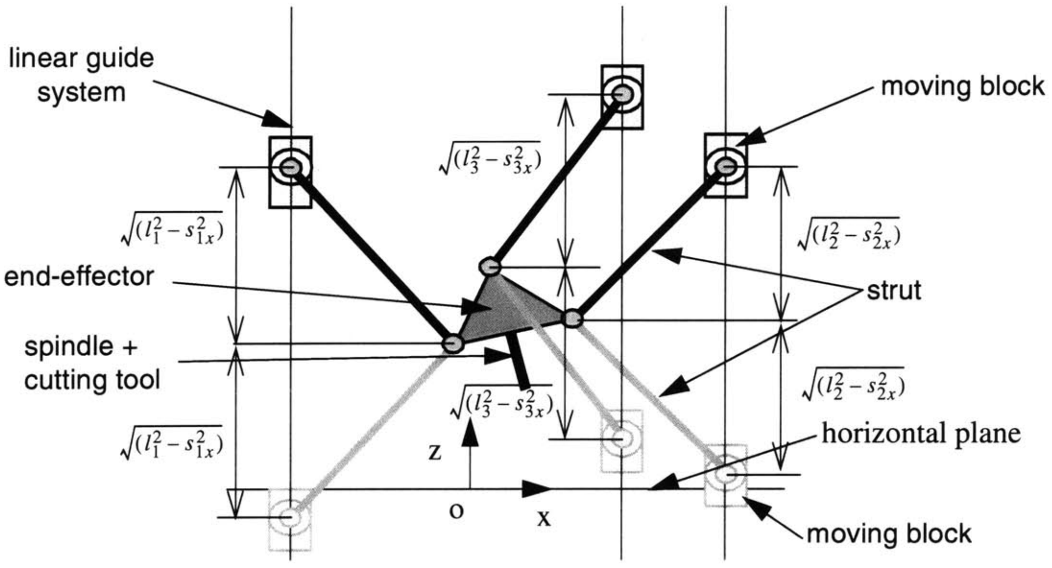

(a) possible configurations

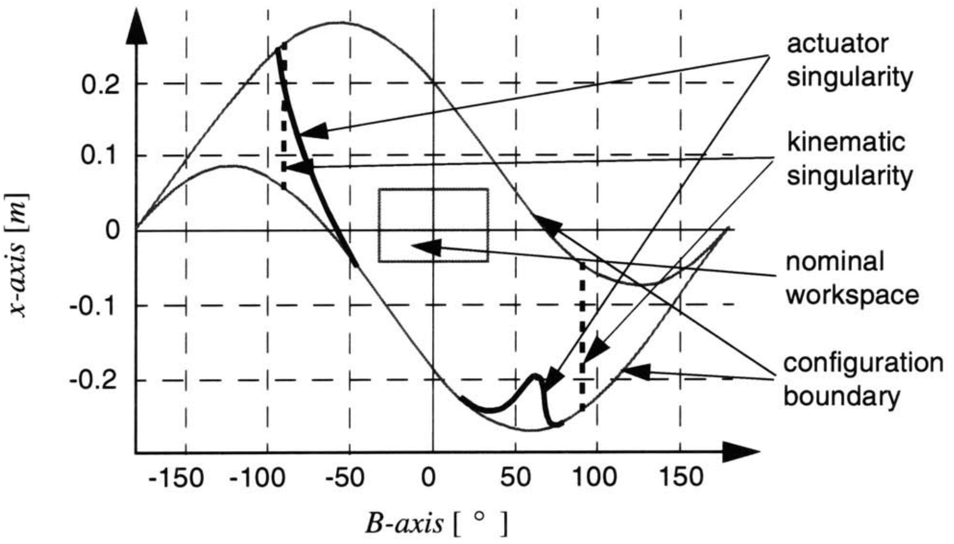

(b) singularity map

Figure 28 Kinematic analysis

6.2 Stiffness Analysis

We limit our attention to the parallel structure because it is the more compliant of the two structures. The overall stiffness of the machine structure depends mostly on the joint stiffnesses because joints are usually the most compliant elements in such machines. There are several engineering methods for increasing stiffness, such as using a pre-load, and using roller bearings instead of ball bearings. We used a linear motion system with cylindrical roller carriages in the prismatic joints and tapered roller bearings in the rotational joints. The stiffness along the x and z directions are investigated by studying the Jacobian derived in Equation 48 and the machine element stiffness. There are tapered roller bearings at each end of the strut. The radial deflection of a preloaded roller bearing is proportional to the $(load)^{0.9}$ [15,18]. For simplicity, we assume that the deflection and load-relation is linear. Therefore we can consider the roller bearings as linear springs. Let the bearing stiffness at the end-effector side be k_{se}, the bearing stiffness of the moving block side be k_{sm}, and the stiffness of struts be k_{st}. The struts are intended to resist only compression or extension forces in the plane (although they will be subject to out-of-plane loads). Since all the bearings are linked serially, the overall stiffness of the *i-th* strut, k_i, can be written as:

$$\frac{1}{k_i} = \frac{1}{k_{se}} + \frac{1}{k_{sm}} + \frac{1}{k_{st}} \tag{51}$$

The overall structural stiffness of the system can be shown to be $J^{-T}K_{st}J^{-1}$ where K_{st} is a diagonal matrix with elements k_i, $K_{st}(i, i) = k_i$. The displacement vector $\vec{d}_1$ for the x, z and *B-axis* can be derived using the overall structural stiffness and applied external load $\vec{F}_{ext}$.

$$\vec{d}_1 = \begin{bmatrix} \delta_{1x} \\ \delta_{1z} \\ \delta_{1b} \end{bmatrix} = K_{so}^{-1}\vec{F}_{ext} \tag{52}$$

Where $K_{so} = J^{-T}K_{st}J^{-1}$. We assume that control with position feedback from the moving block position is ideal, which means that the stiffness of linear guide systems is infinite and the moving blocks are fixed along the z-direction. We need to introduce a new Jacobian with respect to w_1, w_2, and w_3, where w_1, w_2, w_3 are the distances between the origin and the prismatic joint axes, because moving blocks can deflect along the x direction also. Let the stiffness of the linear guide systems be k_{tr} and new Jacobian be J_{tr}. The stiffness of the linear guide systems can be shown to be $J_{tr}^{-T}K_{tr}J_{tr}^{-1}$ where K_{tr} is a diagonal matrix with elements k_{tr-i}, $K_{tr}(i, i) = k_{tr-i}$. The displacements of end-effector, $\vec{d}_2$, caused by the moving block displacement is

$$\vec{d}_2 = \begin{bmatrix} \delta_{2x} \\ \delta_{2z} \\ \delta_{2b} \end{bmatrix} = K_{to}^{-1}\vec{F}_{ext}. \qquad (53)$$

where $K_{to} = J_{tr}^{-T}K_{tr}J_{tr}^{-1}$. Jacobian for the moving block deflection, J_{tr}, is shown in Appendix B. We can investigate the stiffness characteristic of the parallel structure with Equations 52 and 53. Figure 29-(a) shows the stiffness in the *x-B* workspace. The stiffness map is quite flat in the middle of the workspace; however as the end-effector approaches the lower left corner the stiffness drops rapidly because the configuration of the parallel structure is getting closer to an actuator singularity. Figure 29-(b) shows the stiffness map of the Hexel's Hexapod at the level of $z = 0.4m$. The stiffness variations of the Hexapod are very much greater, and the stiffness drops far more rapidly as the end-effector moves away from the middle of the workspace. In other words, the fact that we use a lower order parallel mechanism makes the behavior of our machine more constant. However, even in our case, we must select the workspace to avoid the more severely compromised portions of the configuration space.

We investigated the stiffness of the machine along the *y*-direction and computed the modal stiffness in several postures of the end-effector using finite element analysis. The results show that the static stiffness along *y-axis* is about $35.0N/\mu m$ and the *1st* mode frequency is 111.2*Hz*, which is shown in Figure 30-(a). Several simulations with different spindle orientations show that variation in the angular postures does not affect the static and dynamic stiffnesses very much because the *1st* mode shape depends on the mass of the end-effector and the joint bearing compliances and the strut lengths are constant. The *2nd* mode frequency shown in Figure 30-(b), which is dominated by joint bearing compliance at moving block side, is 182.3*Hz*. These are much higher than one would encounter with conventional machine tools, where the typical value is in the range of 30 ~ 50*Hz*. The granite frame bending mode frequency, shown in Figure 30-(c), is 269.4*Hz* and the twisting mode frequency, shown in Figure 30-(d), is 320.9*Hz*. The modal frequency of granite frame can be easily enhanced by increasing its thickness.

In summary, numerical analysis about the MIT-SS-1 show that it is quite stiff dynamically and statically and the stiffness variation is very low when compared with that of the Hexapod. These structural performance is also evaluated by experiments.

6.3 Workspace

Parallel mechanisms usually have limited orientation space because singular configurations are closely related with end-effector tilting. We assigned the larger stroke, $\pm 100°$, for the serial structure and the smaller stroke, $\pm 30°$, to the parallel structure.

We can examine the workspace of the MIT-SS-1 by considering axis travel limitations. The

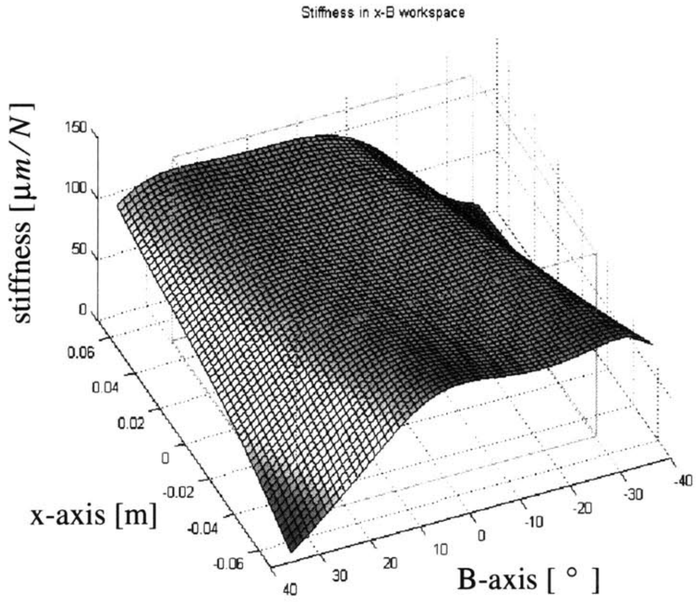

(a) The MIT-SS-1

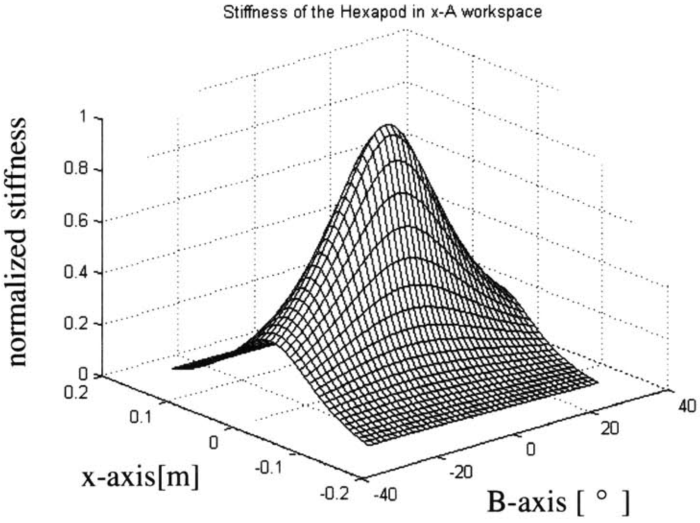

(b) Hexapod

Figure 29 Stiffness map of the parallel structure

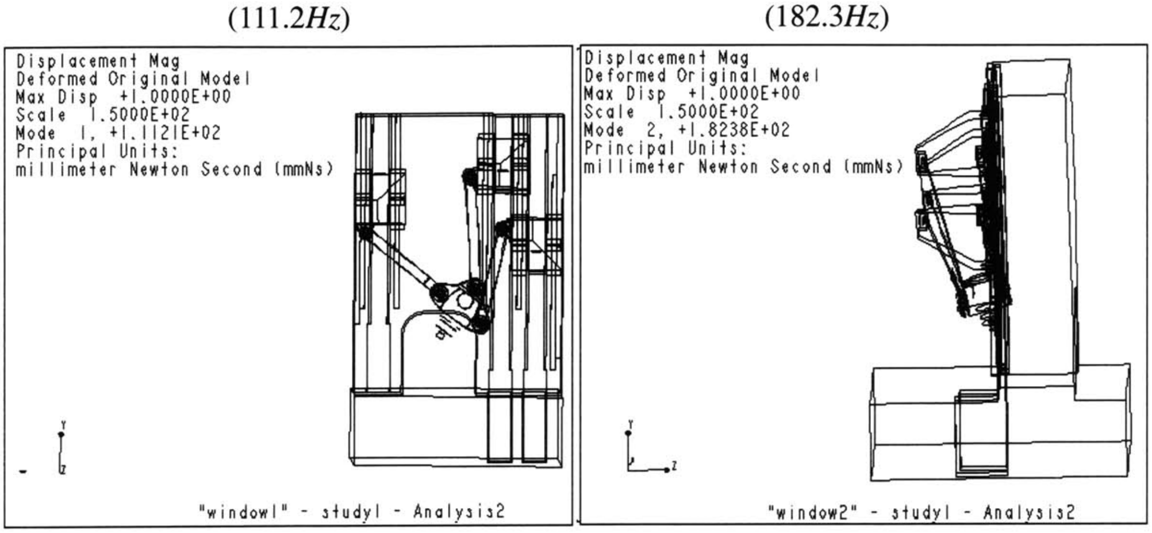

(111.2*Hz*) (182.3*Hz*)

(a) 1st mode (b) 2nd mode

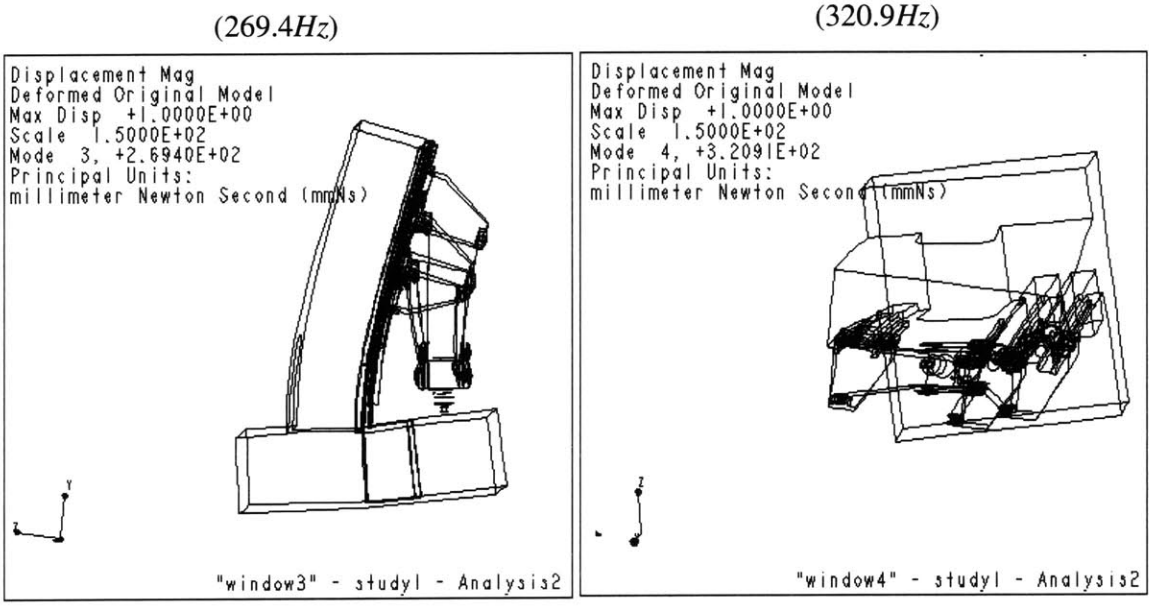

(269.4*Hz*) (320.9*Hz*)

(c) 3rd mode (d) 4th mode

Figure 30 Modal analysis

rotational axis and the translational axis in serial structures don't affect the other axis travelling limits. On the other hand, the rotational axis and the translational axis in the parallel structure do affect the other axis travel limits. We are, therefore, interested in the workspace of the parallel structure installed on the vertical plane. Figure 31-(a) shows the *x-z* workspace with/without end-effector tilting, and Figure 31-(b) shows the workspace with the end-effector tilted positions (the tilt degree corresponds to the vertical axis). As the orientation, *b*, approaches $+80^\circ/-60^\circ$, the *x-z* workspace decreases because of collision between struts, the end-effector, and mechanical stops.

When we compute the workspace while considering the tilting of the *B-axis*, we refer to it as the 5-axis workspace. When the end-effector is not tilted, we will refer to the extent of the workspace as the 3-axis workspace. The 5-axis workspace is shown in Figure 31-(a), and its area is, as expected, smaller than 3-axis workspace. Since machine tool vendors typically supply the information regarding only the travel length of each axis, we compared the volume ratio of the MIT-SS-1 with that of commercial 5-axis CNC milling machines based on the 3-axis workspace. The term "volume ratio" here represents the ratio of the workspace volume to the machine volume. Figure 32 shows that commercial 5-axis CNC milling machines have a volume ratio of about 1%. In the case the Cincinnati U5, which is a gantry type serial machine with a fixed table, and the whole structure moves along the *x-axis* up to 4.2m. If the *x-axis* travelling length is increased, the volume ratio can be improved. This type of machine is applicable to a large

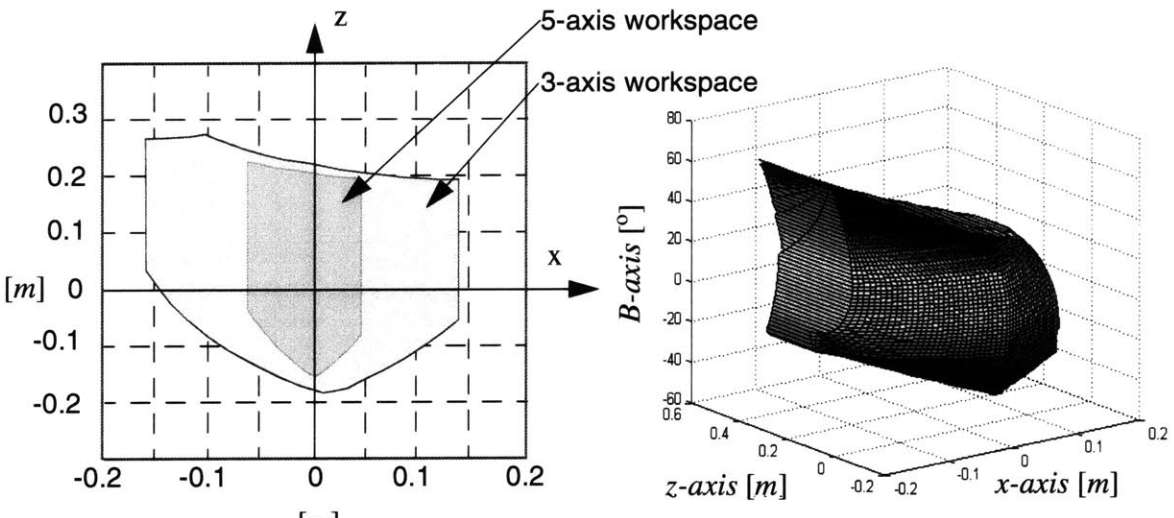

(a) workspace on *x-z* plane

(b) workspace in *x-z-B*

Figure 31 Workspace of the MIT-SS-1

workpiece which is common in aircraft industry. The volume ratio of the MIT-SS-1 is about 2.1%, and is almost identical with that of machine "U5". After the addition of ancillary equipment, such as an automatic tool changer (ATC) and coolant delivery systems, we expect that the volume ratio of our machine to be around 1.5%, which is still higher than commercial machine tools.

6.4 Manipulability

The MIT-SS-1 consists of 4 translational actuators and 1 rotational actuator. We have investigated the position manipulability only because the rotational axis (*A-axis*) has an independent drive mechanism, the rotation velocity of which can be adjusted by changing the gear ratio. Figure 33 and Figure 34 show the manipulability of the MIT-SS-1. Velocity ellipsoids in *x-y-z* workspace are shown in Figure 33. Quantitative measures are shown in Figures 34-(a), 34-(b), and 34-(c). The condition number varies between 1.74 ~ 2.71; this range is lower than the Hexapod which varies between 2.76 ~ 3.10. However, as the end-effector gets close to $x = -0.06, b = -30°$ or $x = 0.04, b = 30°$, the condition number increases sharply and the volume of the velocity ellipsoid and the minimum eigenvalue goes down rapidly, which imply that the MIT-SS-1 loses manipulability near those regions. As the angle between the strut and the horizontal line decreases, it becomes harder to move the end-effector along x-axis. The extreme case is when the strut is in the horizontal plane, in which the mechanism loses degrees of freedom. Therefore, workspace should be defined very carefully. This explains the 0.01*m*

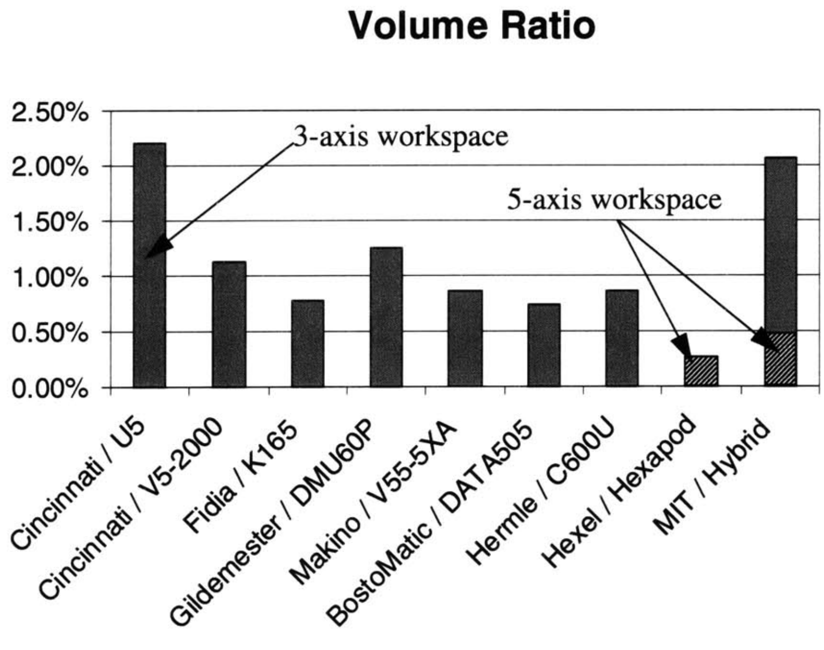

Figure 32 Volume ratio between workspace and machine volume

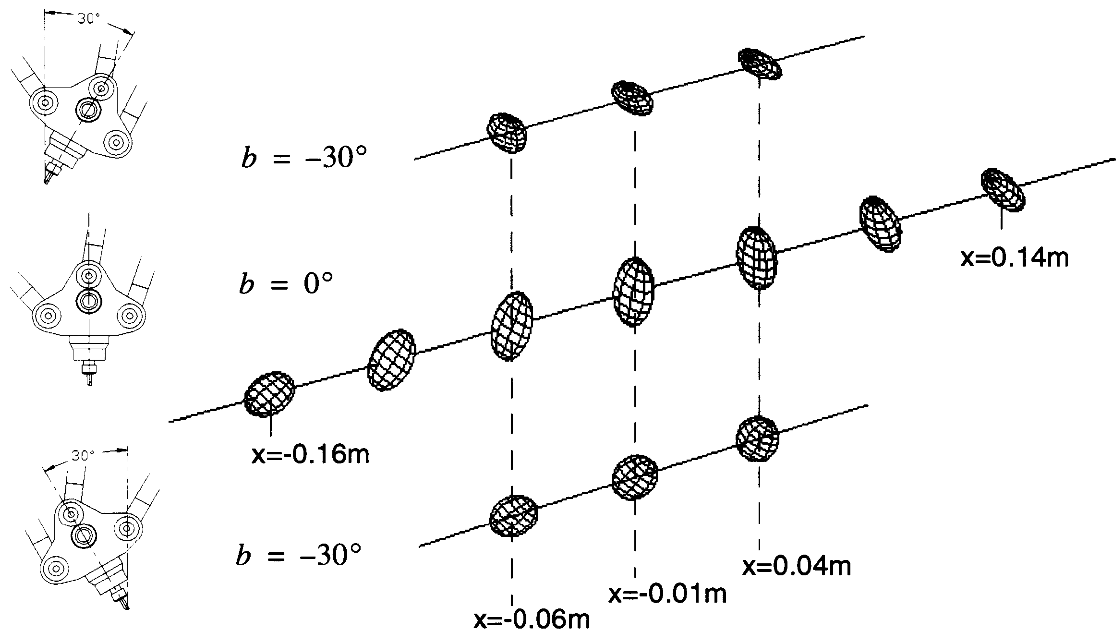

Figure 33 Velocity ellipsoids of the MIT-SS-1

workspace shift along *x-axis*.

6.5 Reversals in plane

Reversal singular points can be computed by solving $\partial f_k/\partial u = 0$ and $\partial f_k/\partial v = 0$ simultaneously for each k. We show a typical case in Figure 35-(a); in the task space shown, we show $\partial f_4/\partial u = 0$ lines, $\partial f_4/\partial v = 0$ lines and the level lines of the 4th component $f_4(u, v)$ of the inverse kinematics of the hybrid machine when we machine the curved surface with the surface normal orientation. One reversal singular point is strong among the total of 3 reversal singular points as shown in Figure 35-(a). By repeating the same procedure for other actuators, we find the total of 30 reversal singular points in the task space as shown in Figure 35-(b). In Figure 36, singular points are shown at each cutting condition. In case of the vertical orientation, only 3 singular points exist on the curved surface and no singular point exists on the flat plane. The number of singular points is highly dependent on the tool orientation requirement, which is similar to the serial and parallel mechanisms.

We have checked the reversal lines which are generated during the surface sweep task. Figure 37 show the results. The reversal lines depend the tool path. Circle shaped tool path show the most complicated reversal lines. And also, surface normal machining condition induces more reversal

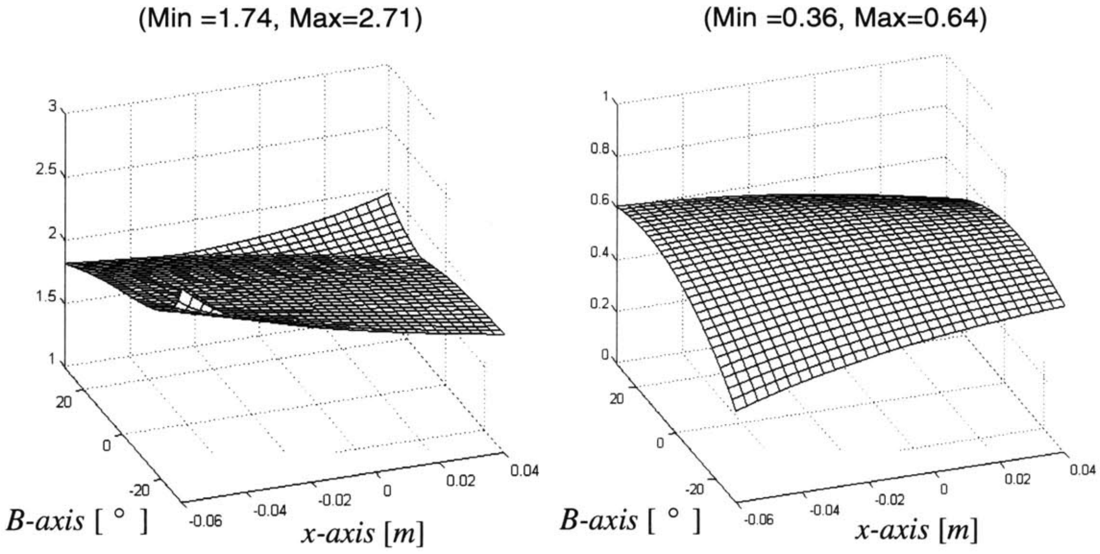
(Min =1.74, Max=2.71)

(Min =0.36, Max=0.64)

(a) Condition number

(b) Volume of the ellipsoid

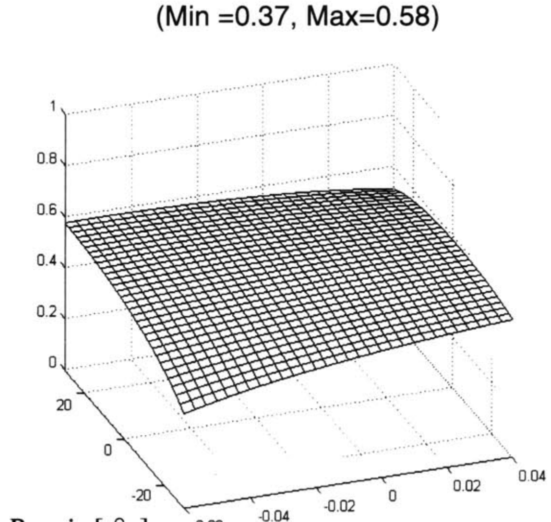
(Min =0.37, Max=0.58)

(c) Minimum eigenvalue

Figure 34 Position manipulability of the MIT-SS-1

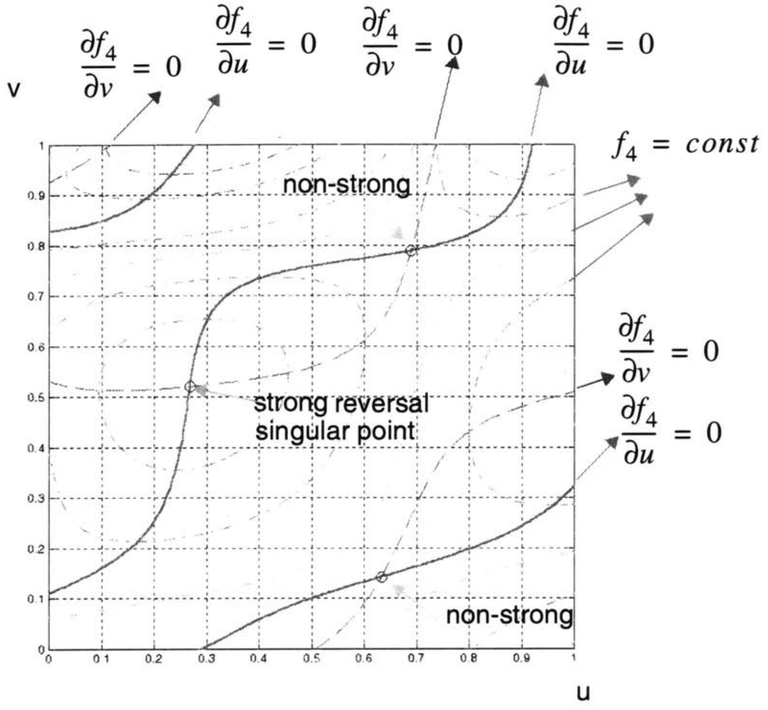

(a) The Reversal Singular Points for the 4th Actuator of the Hybrid Machine for Surface Normal Orientation Assignment in uv-Task Space or Parameter Space.

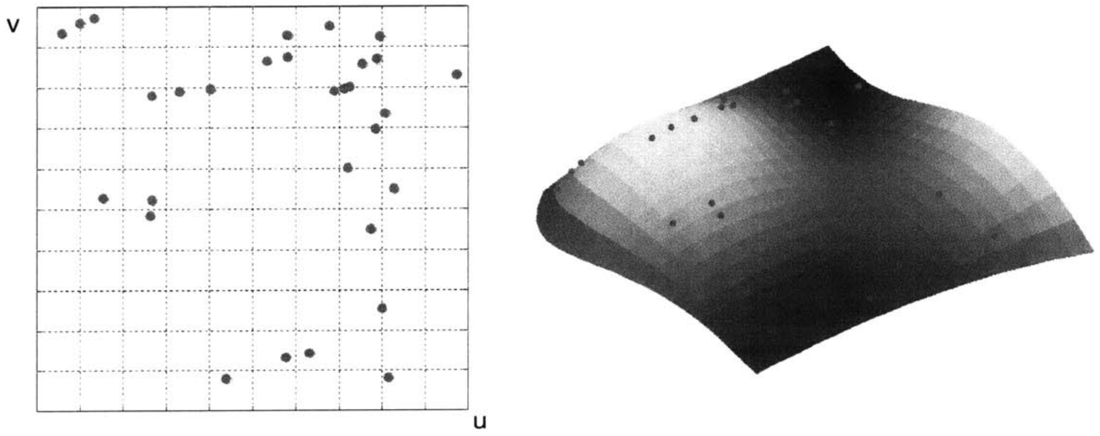

(b) The distribution of all the reversal singular points.

Figure 35 Finding reversal singular points of the MIT-SS-1

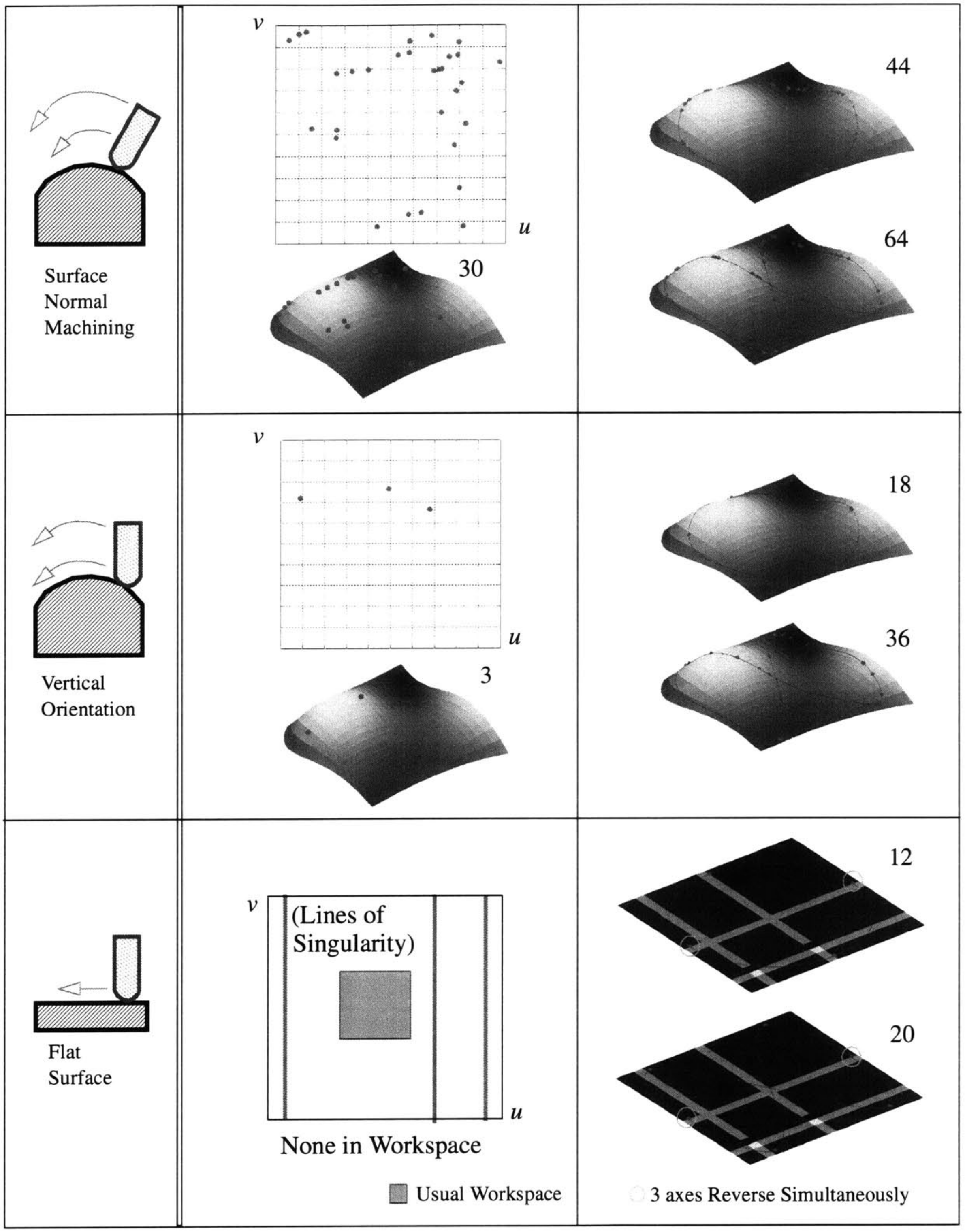

Figure 36 Distribution of Reversal Singular Points

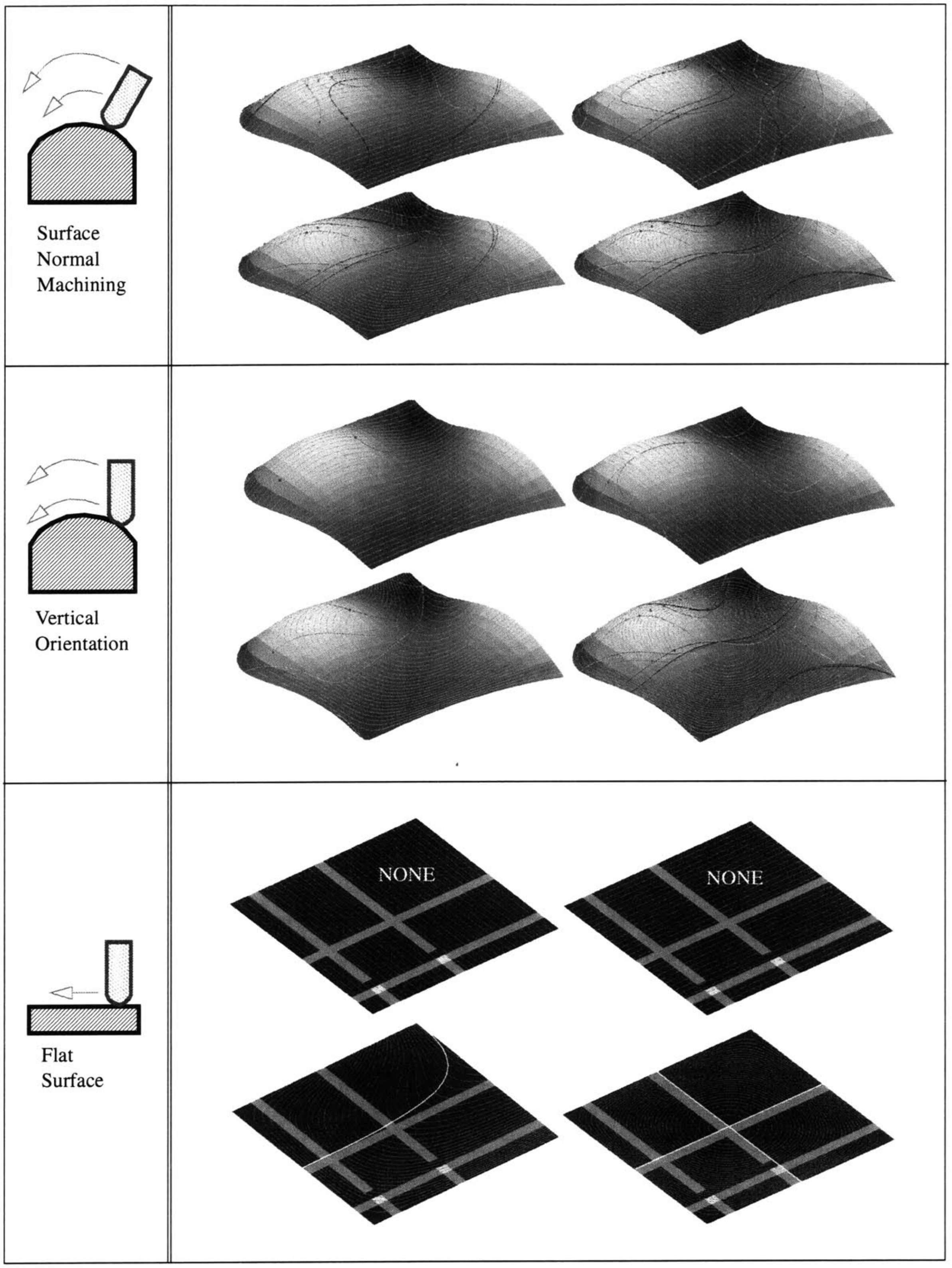

Figure 37 Reversal lines for various cases

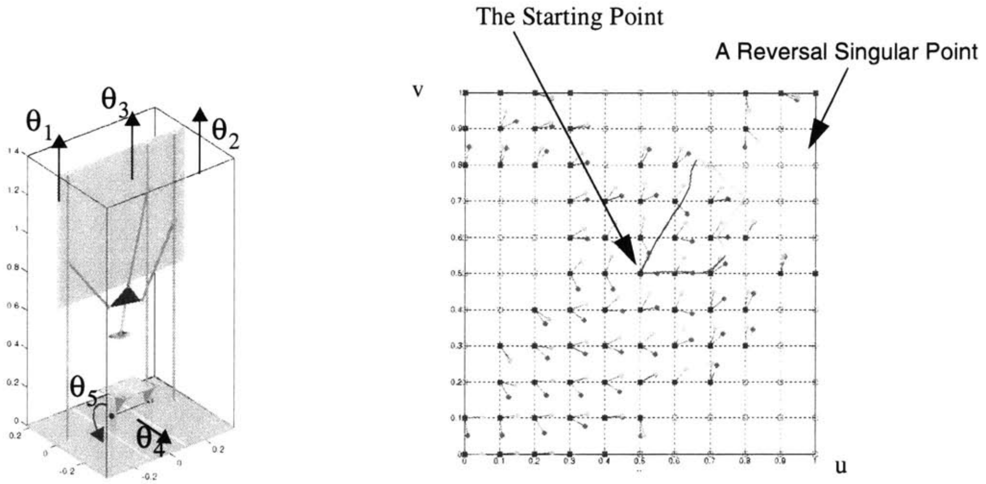

(a) The surface normal machining using the MIT-SS-1

(b) The reversal free cones in the 01111th plate and the corresponding reachability leaf

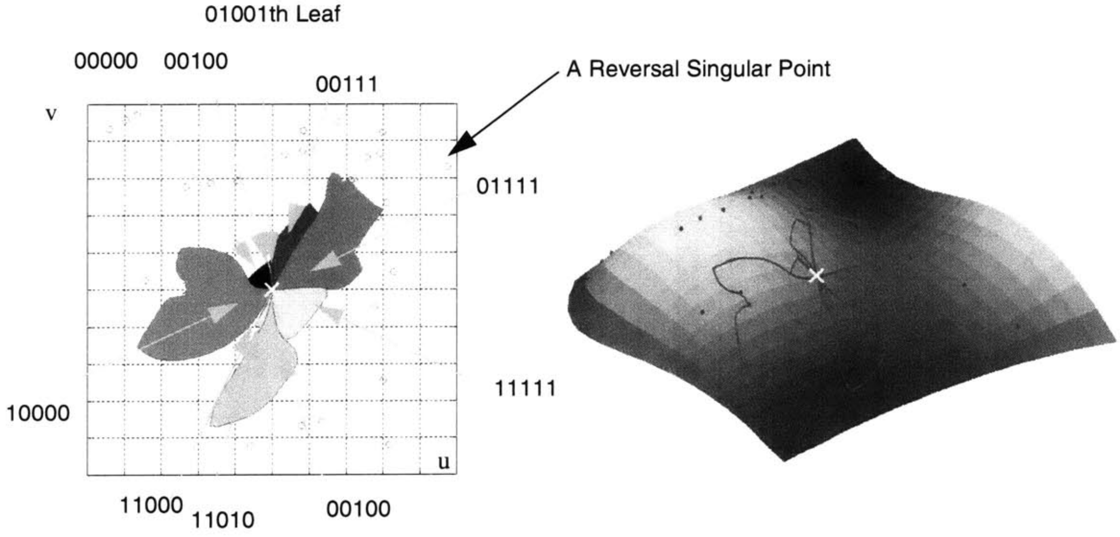

(c) The reachability set constructed as a union of reachability leaves in the parameter space

(d) The reachability set in the workspace

Figure 38 Finding a reachability set

lines than the vertical orientation machining condition. In case of the flat plane sweep task, though the reversal lines are simple, it has similar trend to the case of the curved surface.

Generating reversal free tool-path depends highly on the reachable region without reversal in workspace when the starting point is decided. The reachable regions are shown in Figure 38-(c). The tool tip is placed at the "x" mark, it can reach within the reachability leaves. However, tool path can not cross the boundary of the reachability leaves to maintain reversal free condition.

The analysis shows that the reversal characteristics of the MIT-SS-1 are simpler than the Hexapod, but more complicated than the serial machine. And they are highly dependent on the tool path as well as the surface type.

6.6 Structural over-constraint

An elegant aspect of hexapods is that they are perfectly constrained: six degrees of freedom are determined by six actuators, and assembly involves no over-constraint. The one serious disadvantage of planar PKM of the type proposed here is that they are fundamentally over-constrained structures. From a practical point of view it is impossible to achieve perfect parallelism between three rotational axes, and between prismatic joints. Only if the misalignments are small enough that the bearing and strut compliances can absorb them, the mechanism will work as expected. What these acceptable manufacturing tolerances are depends on two factors: 1) the tolerances we seek from the machine tool, and 2) the allowable load limits of the structural elements when they are forced into an over-constrained assembly. In our machine, the second factor dominates. An important feature of the MIT-SS-1 is the fact that all three prismatic joints have been designed to lie on a single ground surface. This greatly reduces the tolerance stack-up and limits the extent of the over-constraint problem. Figure 39 shows the evolution of the machine topology in response to these manufacturing concerns. The design (a) was the first concept with no manufacturing considerations. The design (b) attempted to reduce the misalignments between two of the three prismatic joints by placing them on the same datum. The design (c), all three linear guides on the same plane, reducing stack-up further and in particular, overcomes the over-constraint problem. Final version of the MIT-SS-1 becomes more feasible.

Joint bearings with rolling elements are usually the most compliant structural elements and have low allowable load limits because the rolling elements fail easily under heavy loads. Examples of recommended load limits and compliances of a deep groove ball bearing and a tapered roller bearing are available in [15,46]. Struts also have compliances. The struts, thus, can be modeled as rigid solids with springs as shown in Figure 40. The real joint positions on each strut are determined by assuming that the assembly is at the extreme of its manufacturing tolerance. The end-effector must be in equilibrium after assembly. The end-effector is much stiffer than the strut and the bearing assembly, and can thus be considered as a rigid solid because it consists of one

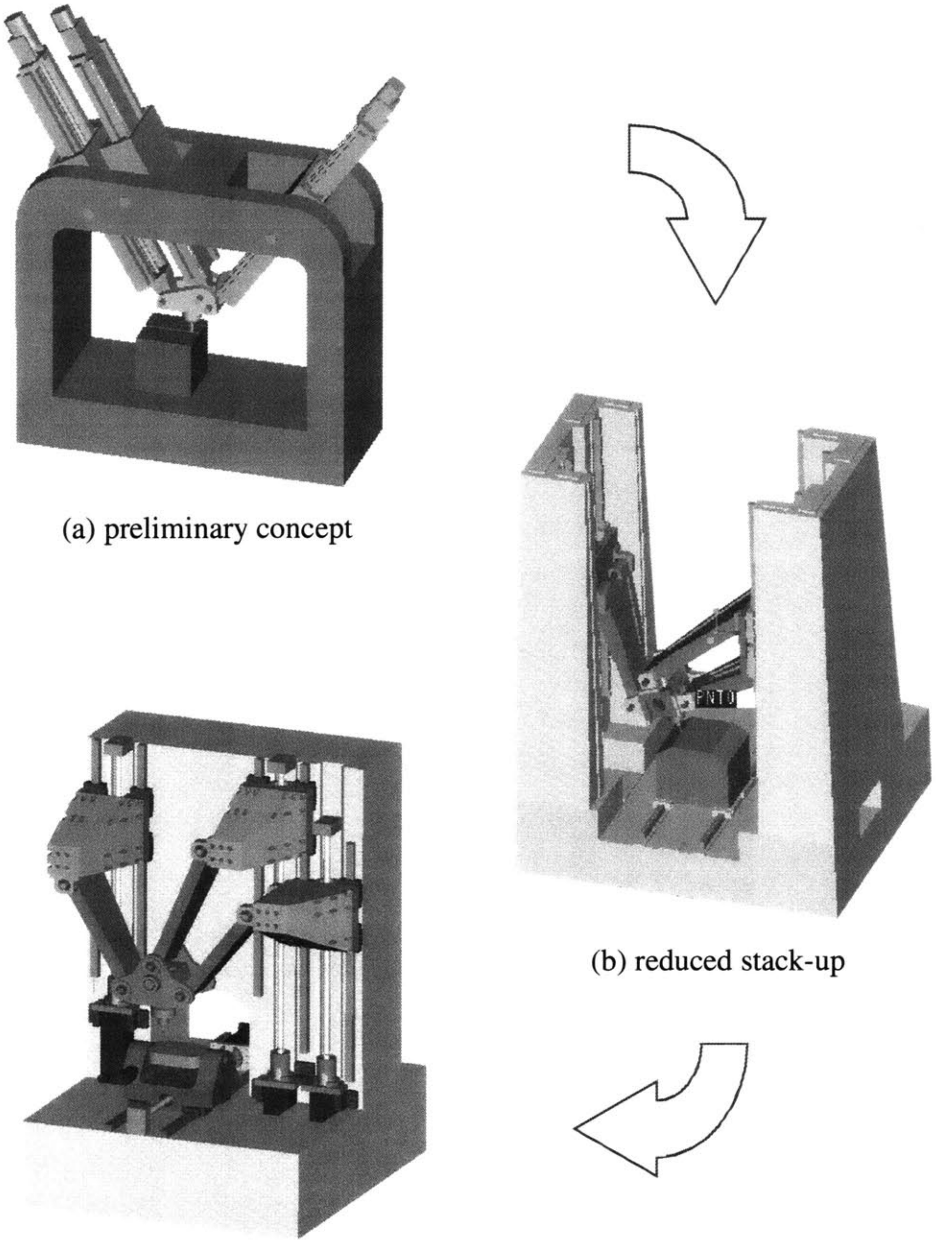

(a) preliminary concept

(b) reduced stack-up

(c) reduced stack-up

Figure 39 Evolution of the MIT-SS-1 to reduce misalignment errors: design for manufacture

solid steel body. If the equilibrium position of the end-effector can be determined, we can calculate the forces which are applied to the joints. The values of these forces will tell us if the over-constraint is acceptable. The remainder of this section will show how to compute the equilibrium position and the required assembly forces at the joints because the system is not statically determinate.

Let the ideal joint positions of the moving block be D_i, and its equilibrium positions after the assembly be R_i. Figure 41 shows the end-effector displacements due to manufacturing errors. Equilibrium position, R_i, can be obtained from D_i if displacement vector, $\vec{u}_i$, is obtained. We need 3 translational and 3 rotational parameters to describe the end-effector because a rigid body has 6-dof in space. Let us attach a body-fixed coordinate to *joint-1*. Then the end-effector can be described with the translation of the *joint-1* position, $\vec{u}_1$, and the rotation, $\theta\vec{w}$ where $\vec{w}$ is the unit vector along the rotation axis. Rotation matrix R_o, can be expressed as [36]:

$$R_o = e^{\hat{w}\theta} = \begin{bmatrix} 1 - v_\theta(w_y^2 + w_z^2) & w_x w_y v_\theta - w_z s_\theta & w_x w_z v_\theta + w_y s_\theta \\ w_x w_y v_\theta + w_z s_\theta & 1 - v_\theta(w_x^2 + w_z^2) & w_y w_z v_\theta - w_x s_\theta \\ w_x w_z v_\theta - w_y s_\theta & w_y w_z v_\theta + w_x s_\theta & 1 - v_\theta(w_x^2 + w_y^2) \end{bmatrix} . \tag{54}$$

where $v_\theta = 1 - cos(\theta)$ and $s_\theta = sin(\theta)$. Typical manufacturing errors with modern CNC machines are well under $30\mu m$. We can assume that the amount of rotation, θ, is small enough that $v_\theta = 0, s_\theta = \theta$. The rotation matrix can be simplified in the following form:

$$R_o = I + \begin{bmatrix} 0 & -w_z\theta & w_y\theta \\ w_z\theta & 0 & -w_x\theta \\ -w_y\theta & w_x\theta & 0 \end{bmatrix} = I + \begin{bmatrix} 0 & -\theta_z & \theta_y \\ \theta_z & 0 & -\theta_x \\ -\theta_y & \theta_x & 0 \end{bmatrix} \tag{55}$$

The displacement vector, $\vec{u}_i$, of the joints can be obtained using $\hat{\theta}$:

$$\vec{u}_i = \vec{u}_1 + \theta\vec{w} \times \vec{p}_i = \vec{u}_1 + \hat{\theta}\vec{p}_i \tag{56}$$

The spring deformation vector, $\vec{q}_i$, can be written as:

$$\vec{q}_i = \vec{u}_i - \vec{e}_i = \vec{u}_1 + \hat{\theta}\vec{p}_i - \vec{e}_i . \tag{57}$$

Potential energy in the springs can be obtained by using $\vec{q}_i$:

$$V = \sum\frac{1}{2}\vec{q}_i^T\bar{K}_i\vec{q}_i = \sum\frac{1}{2}[\vec{u}_i - \vec{e}_i]^T\bar{K}_i[\vec{u}_i - \vec{e}_i]$$
$$= \sum\frac{1}{2}[\vec{u}_i^T\bar{K}_i\vec{u}_i + \vec{e}_i^T\bar{K}_i\vec{e}_i - 2\vec{u}_i^T\bar{K}_i\vec{e}_i] \tag{58}$$

where $\bar{K}_i = Diag(k_{ix}, k_{iy}, k_{iz})$.

We apply the virtual work theorem for this static system: $\vec{F}_{ext} \bullet \delta\vec{e} = \delta V$.

$$\delta V = \sum\delta\vec{q}_i^T\bar{K}_i\vec{q}_i = \sum[\delta\vec{u}_1 + \delta\hat{\theta}\vec{p}_i]^T\bar{K}_i\vec{q}_i$$
$$= \sum\delta\vec{u}_1^T\bar{K}_i\vec{q}_i + \sum[\delta\hat{\theta}\vec{p}_i]^T\bar{K}_i\vec{q}_i \tag{59}$$

where $\delta\vec{q}_i = \delta\vec{u}_1 + \delta\hat{\theta}\vec{p}_i + \hat{\theta}\delta\vec{p}_i - \delta\vec{e}_i = \delta\vec{u}_1 + \delta\hat{\theta}\vec{p}_i$.

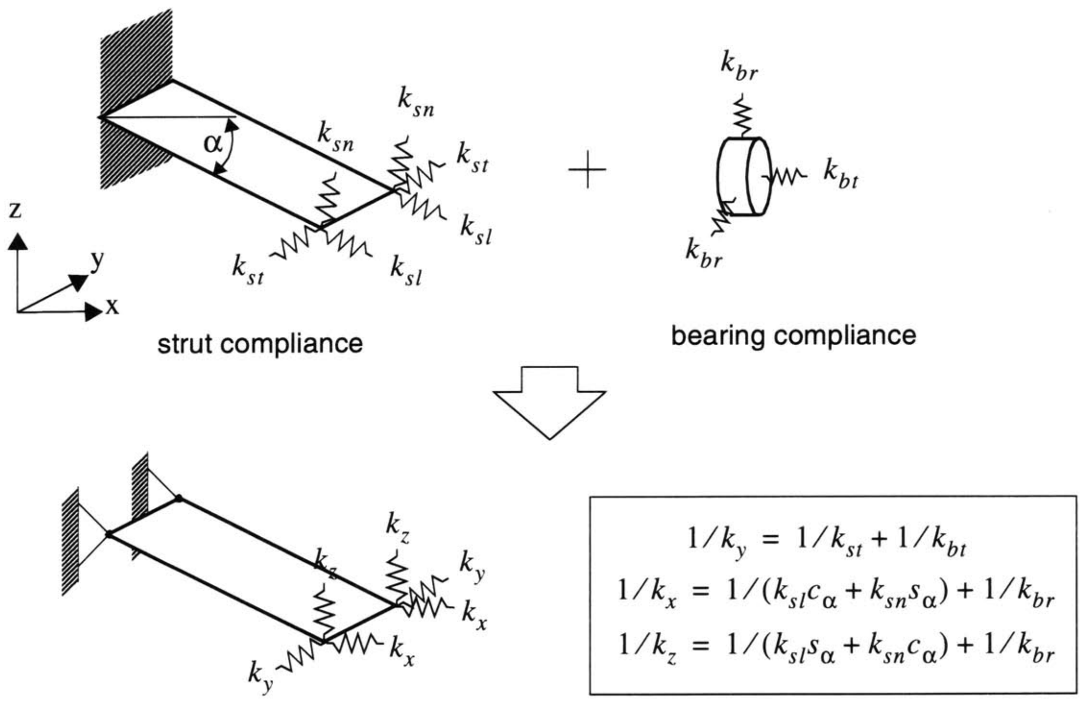

$$1/k_y = 1/k_{st} + 1/k_{bt}$$
$$1/k_x = 1/(k_{sl}c_\alpha + k_{sn}s_\alpha) + 1/k_{br}$$
$$1/k_z = 1/(k_{sl}s_\alpha + k_{sn}c_\alpha) + 1/k_{br}$$

Figure 40 Model for strut and joint bearing assembly

There is no work done by the surroundings because no external forces exist. δV should be equal to zero. Equations 60 and 61 below can be derived with the condition that $\delta\vec{u}_1^T$ and $\delta\vec{\theta}$ are arbitrary.

$$\sum \bar{K}_i\vec{e}_i = \sum \bar{K}_i\vec{u}_i + \sum \bar{K}_i\bar{E}_x\vec{p}_i\theta_x + \sum \bar{K}_i\bar{E}_y\vec{p}_i\theta_y + \sum \bar{K}_i\bar{E}_z\vec{p}_i\theta_z \qquad (60)$$

where $\bar{E}_x = \begin{bmatrix} 0 & 0 & 0 \\ 0 & 0 & -1 \\ 0 & 1 & 0 \end{bmatrix}$, $\bar{E}_y = \begin{bmatrix} 0 & 0 & 1 \\ 0 & 0 & 0 \\ -1 & 0 & 0 \end{bmatrix}$, and $\bar{E}_z = \begin{bmatrix} 0 & -1 & 0 \\ 1 & 0 & 0 \\ 0 & 0 & 0 \end{bmatrix}$.

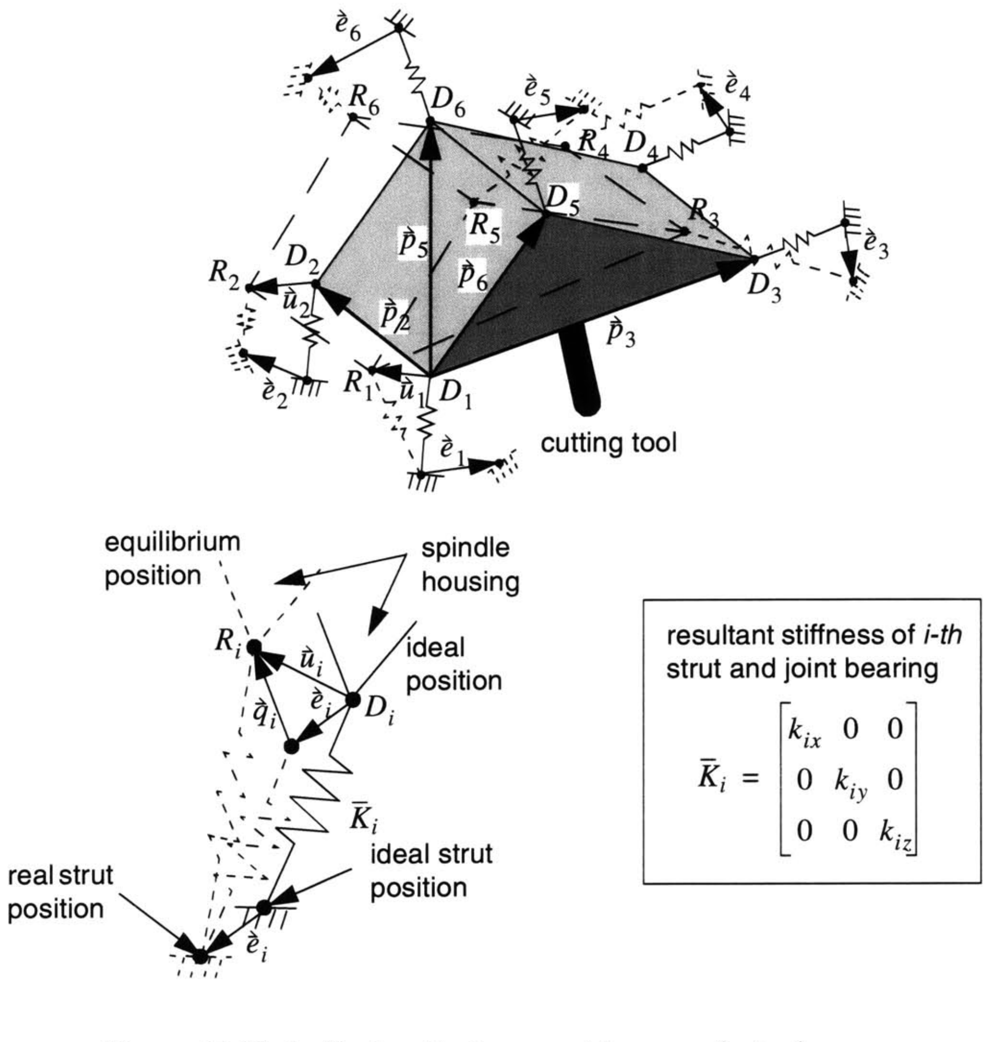

Figure 41 End-effector displacement by manufacturing errors

$$\sum \hat{p}_i \bar{K}_i \vec{e}_i = \sum \hat{p}_i \bar{K}_i \vec{p}_1 + \sum \hat{p}_i \bar{K}_i \bar{E}_x \vec{p}_i \theta_x + \sum \hat{p}_i \bar{K}_i \bar{E}_y \vec{p}_i \theta_y + \sum \hat{p}_i \bar{K}_i \bar{E}_z \vec{p}_i \theta_z \tag{61}$$

where $\begin{bmatrix} 0 & -p_{iz} & p_{iy} \\ p_{iz} & 0 & -p_{ix} \\ -p_{iy} & p_{ix} & 0 \end{bmatrix}$.

Combining Equations 60 and 61 leads to Equation 62.

$$\begin{bmatrix} \left[\sum \bar{K}_i\right] & \left[\sum \bar{K}_i \bar{E}_x \vec{p}_i\right] & \left[\sum \bar{K}_i \bar{E}_y \vec{p}_i\right] & \left[\sum \bar{K}_i \bar{E}_z \vec{p}_i\right] \\ \left[\sum \hat{p}_i \bar{K}_i\right] & \left[\sum \hat{p}_i \bar{K}_i \bar{E}_x \vec{p}_i\right] & \left[\sum \hat{p}_i \bar{K}_i \bar{E}_y \vec{p}_i\right] & \left[\sum \hat{p}_i \bar{K}_i \bar{E}_z \vec{p}_i\right] \end{bmatrix} \begin{bmatrix} \left[\vec{u}_1\right] \\ \theta_x \\ \theta_y \\ \theta_z \end{bmatrix} = \begin{bmatrix} \left[\sum \bar{K}_i \vec{e}_i\right] \\ \left[\sum \hat{p}_i \bar{K}_i \vec{e}_i\right] \end{bmatrix} \tag{62}$$

With Equation 62 the displacement of the position D_1, $\vec{u}_1$, and the rotation angle, $\begin{bmatrix} \theta_x & \theta_y & \theta_z \end{bmatrix}^T$, can be obtained. Now we can derive the spring deformation with Equation 57. And the required assembly forces at each joint can be obtained with the stiffness matrix and deformation of the *joint-i*:

$$\begin{bmatrix} F_{ix} \\ F_{iy} \\ F_{iz} \end{bmatrix} = \begin{bmatrix} k_{ix} & 0 & 0 \\ 0 & k_{iy} & 0 \\ 0 & 0 & k_{iz} \end{bmatrix} \begin{bmatrix} q_{ix} \\ q_{iy} \\ q_{iz} \end{bmatrix} . \tag{63}$$

We examined the required assembly forces at each joint location for 3 equal, fixed-length strut planar mechanisms. Figure 42 shows the schematic diagram and the dimensions. We assume that parallelism between ideal rotational axis and real rotational axis is $300 \mu m/m$ and that the rotational axis can be placed randomly on the surface of the tolerance cone. The width of strut, *w*, is determined such that it is related to the bending stiffness along the *y-axis* as shown below:

$$w = l\left(\frac{4K_y}{Et}\right)^{1/3} \tag{64}$$

where *t* is the thickness of the strut. We calculated assembly forces for 3 cases as shown in Table 2. *Fr(max)* in the table stands for maximum radial forces and *Fa(max)* stands for maximum axial forces. There are 6 values of *Fr(max)* and *Fa(max)* in each case; the first number is the assembly

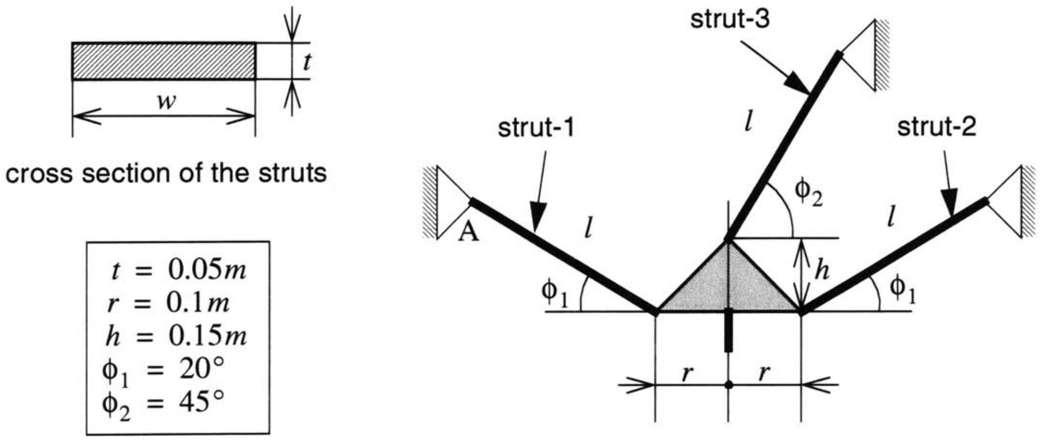

(a) Structure dimensions

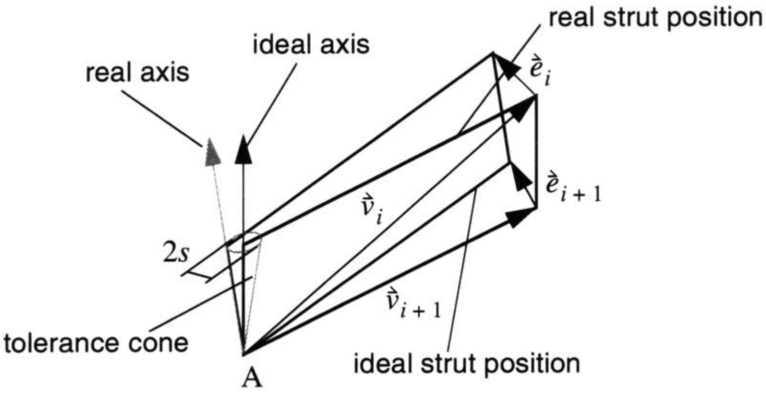

(b) Strut displacement due to manufacturing error

Figure 42 Schematic of the tested structure

force at *joint-1*, the second number the assembly force of *joint-2* and so on. The results show that 3-dof planar parallel structures with longer struts need larger assembly forces and the assembly forces increase linearly with the strut length. This is because the position errors are linearly dependent on the length of the strut and the stiffness of the strut remains constant. Required assembly forces of large structures can exceed the permitted load ranges of joint bearings. This implies that planar parallel mechanisms which use radial rolling bearings are not good for large machine tool applications. On the other hand, these constraints work favorably for small machine tools. For the machine dimensions we have proposed, assembly is possible, and the loads are tolerable.

	l	w	$Fr(max)$ [kN]	$Fa(max)$ [kN]
Case-I	0.5m	0.1m	9.7/4.7/10.0/4.1/10.2/2.9	1.9/1.9/1.8/1.8/1.7/1.7
Case-II	1.0m	0.2m	19.6/7.7/19.8/6.9/18.7/5.8	3.9/3.9/3.7/3.7/3.6/3.6
Case-III	1.5m	0.3m	29.4/10.6/29.5/9.8/27.3/9.2	5.7/5.7/5.6/5.6/5.5/5.5

Table 2: Required assembly forces at each joint for the worst case

7 Performance targets

We have attempted to design a small 5-axis CNC milling machine with high feedrate and acceleration capabilities and high structural rigidity statically and dynamically by using the serial and parallel mechanisms. Therefore, the MIT-SS-1 has been designed with the following performance targets in mind:

- Maximum rapid motion speed in work-space: $30m/min(0.5m/s)$
- Stiffness: $30N/\mu m$
- Dynamic performance: $\omega_1 = 70Hz$
- Acceleration: $2g$

The system will be controlled by PID motion controller, Aerotech UNIDEX500 which can support 4 axes simultaneously. Several spindles have been sized for the machine and IBAG HFK90S40C is selected as the spindle for the MIT-SS-1. The specifications of the motion controller and the spindle are shown in Appendix C. The machine is targeted for high-speed machining of aerospace-type parts.

8 Fabrication

Generally fabrication cost depends highly on the time for assembly and the ratio between the number of standard and custom-made parts. The custom-made parts are usually several times more expensive than the standard ones. And also parts with complex profiles or undercuts are not recommendable because it is not easy to check the dimensional accuracy of the profiles, and the undercuts need more than one setup, which induces poor dimensional accuracy and long assembly time. All custom-made parts, therefore, need to be designed based on DFM (Design For Manufacturing).

8.1 Machine frame

The machine frame is the basis of the whole machine. It will support all the constructural and functional elements and will resist the load generated during machine operation. Good machine performance can not be achieved even with good machine components when the machine frame is designed poorly. There are several design parameters of a machine:

- Static/Dynamic stiffness
- Damping
- Thermal stability
- Configuration

Several materials are generally used in machine tool structures including aluminum, steel, cast iron, copper, granite, polymer concrete, and titanium. Their properties are quite different so that machine designers should consider the specific structural requirements carefully because the requirements listed above are closely related with material properties.

Cast Iron

Historically, cast iron has been used for machine frames since machine tools were introduced. Due to its good damping and good machinability, cast iron is still being used in modern machine tools. Once patterns for the structure are made, a number of parts can be casted economically, which makes cast iron suitable for the mass production. However, as the size of the pattern increases, the manufacturing cost increases rapidly. Cast iron is not recommended for large structures which are generally manufactured using welding.

Aluminum

Aluminum has many good material properties such as high strength-to-weight ratio, good corrosion resistance, good thermal conductivity and excellent machinability. Good machinability results in aluminum being widely used in the aircraft industry, while the ease with which it can be diecasted makes it appropriate for various kinds of appliances which use diecasting for mass production. However, aluminum is generally not considered suitable for machine tool structures due to its poor damping and low surface hardness properties. When aluminum is used for machine frame, additional damping devices are generally required.

Polymer Concrete

Polymer concrete consists of binder and aggregate on whose composition and manufacturing process the material properties depend. Polymer concrete has better damping and larger thermal inertia than cast iron has. Many types of polymer concretes have been developed for machine tool frames. However, absorbing water can induce dimensional changes, and inserts for part assembly are needed because polymer concrete is brittle. Polymer concrete is not proper for precision machine tools which use cutting fluids.

Steel

Steel is one of the most widely used material in industry. It has very good stiffness, machinability, and welding properties. Machine structures with steel are made mainly with bolt jointing process and/or welding process, which makes steel appropriate for large structures. But due to poor damping, steel structures need additional damping devices such as tuned mass damper and shear damper which use viscous materials between layers.

Material	Damping Coefficient $[10^{-4}]$	Young's Modulus $[GN/m^2]$	Specific Weight $[g/cm^3]$	Stiffness to density ratio[a] $[E/\rho]/[E/\rho]_c$	Yield strength $[MN/m^2]$	Manufacturing cost for one quantity
Steel	4.5	200	7.8	1.51	400	Medium
Cast Iron	6.0	120	7.1	1.00	240	High
Polymer Concrete	35.0	45	2.5	1.07	40	High
Aluminum alloy	2.5	70	2.8	1.48	140	Medium
Granite	25.0	78	3.0	1.54	13.5	Low

Table 3: Typical materials for machine frame

a. Stiffness to density ratio is used for comparing the structural materials. Generally, materials with high ratio are more proper for structures which require high rigidity. The values are normalized with respect to Cast Iron.

Granite

Granite has low thermal conductivity and low thermal expansion coefficient, and quite good flatness can be achieved, which makes it proper for precision machine bases which are in clean surroundings. Typical application of granite is for coordinate measuring machines. It is, however, not recommended for cutting machines with coolant because granite absorbs water and swells.

Material properties mentioned above are compared in Table 3. In case of the manufacturing cost, they are compared qualitatively with the assumption that only 1 unit is to be constructed. The frame of the small hybrid 5-axis CNC machine consists of two simple solid blocks. Since both cast iron and polymer concrete need patterns and molds which induce high manufacturing cost, they are unsuitable for the working prototype. Aluminum has poor damping and the surfaces on which the linear guide systems will be installed can be easily damaged, which makes aluminum not proper for the frame of the MIT-SS-1. Steel has high stiffness and good welding property but it has poor damping. To use aluminum or steel as the machine frame, additional dampers would be needed and bolt jointing or welding would need to be used, which results in high manufacturing cost. In the case of granite, it has good damping and the manufacturing cost is low. But it needs to be thick to attain high stiffness because it has a low Young's modulus.

Granite is chosen as the frame material for the MIT-SS-1. Figure 43-(a) shows the granite machine frame which is manufactured by a granite supplier, Rock of Ages Corporation. $4 \mu m$ of surface flatness and $15 \mu m$ squareness between horizontal and vertical plane was achieved. Two granite blocks are connected by bolting and epoxy. Figure 43-(b) shows the configuration of bolt assembly. Eight M20 bolts are incorporated in the assembled structure.

8.2 Joint assembly

Many passive joints are incorporated in parallel machines, and joints are usually more compliant than other machine components, which can make parallel machines loose the advantage of better stiffness. Six pin joints are incorporated in the MIT-SS-1 for passive joints. Using preload is the most common way to achieve better stiffness of bearings. Tapered roller bearings with about $25°$ angle are used for all passive joints in the MIT-SS-1. Preload can be achieved easily by adjusting the preload nuts. After proper preload is applied, the preload nut can be fixed by a set screw. The joint configurations for bearing preload are shown in Figure 44. Since both ends of the pin joint are supposed to have the same amount of preload, the stiffness of both sides of each pin joint can be well balanced.

Interference fit was recommended for the joint bearing assembly in the MIT-SS-1 because clearance fit is usually the source of backlash and harms the whole structure's stiffness. However, once bearings are assembled with interference fit, it is not easy to adjust the bearing

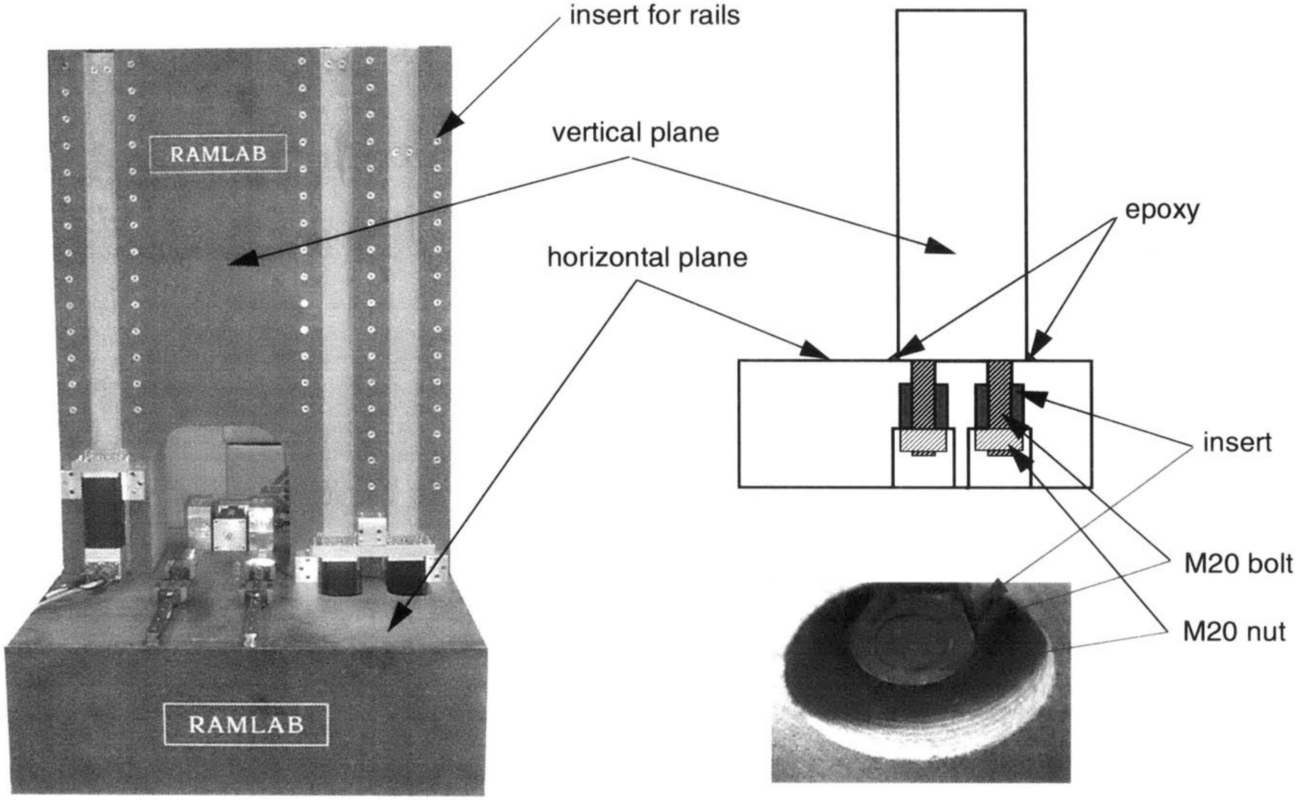

(a) Granite frame

(b) Bolt assembly configuration

Figure 43 Granite frame for the MIT-SS-1

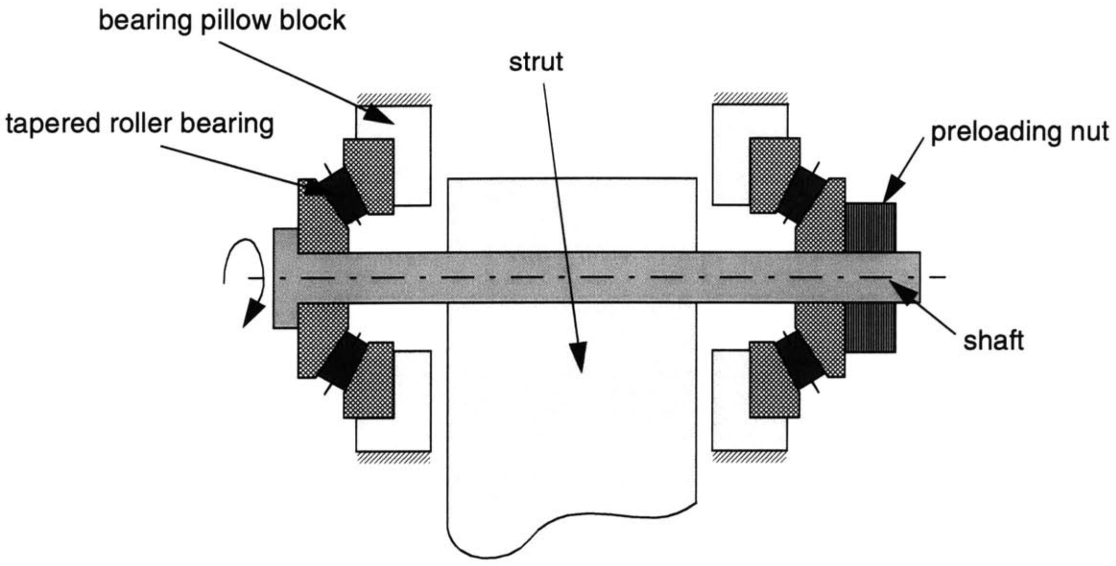

Figure 44 Pin joint configuration

preload. One end of the pin joint shaft is assembled with bearing inner race with $10\mu m$ to $20\mu m$ interference for firm assembly, and the other end is with 0 to $5\mu m$ clearance for adjusting preload with ease. Same assembly method is applied to all pin joints.

In the case of the assembly between a pin joint shaft and a strut, assembly lengths are 140 ~ 220*mm* long, which makes it difficult to use interference fit. Any problem during the assembly process such as dent on the surfaces or sticking due to fast cooling, would require the pin joint shaft and the strut to be thrown away because it is almost impossible to disassemble the shaft and strut without damaging the surfaces. To avoid such problems, three-jaw clamping type

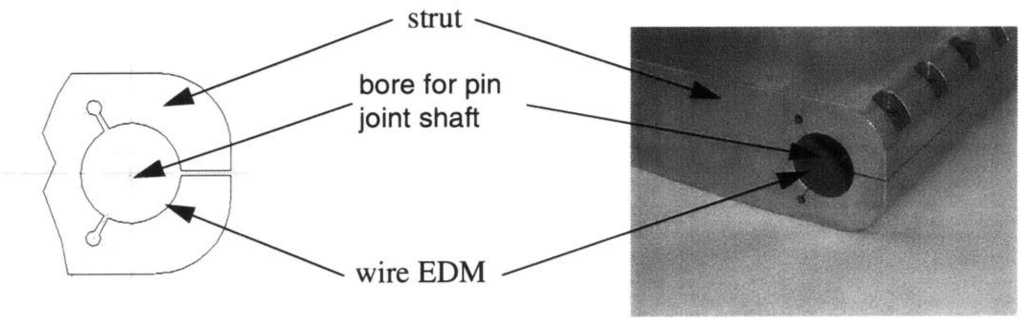

Figure 45 Three jaw clamping configuration in struts

configuration is used which is shown in Figure 45. The hole and the slits are machined with wire EDM process with which $5\mu m$ accuracy and $0.1mm$ slit width can be achieved. Before tightening the clamping screws, the pin joint shaft can be assembled into the struts with clearance fit. When the struts are placed correctly, the shaft is fixed firmly using clamping screws.

8.3 Part machining

The 3-dof planar type parallel mechanism in the MIT-SS-1 incorporates six pin joints which are aligned along the *y-axis*. Six pin joints include several custom made parts and standard machine component, tapered roller bearings. Manufacturing errors in parts are unavoidable, which may cause jamming in joint bearings under normal operating conditions. Parallelism between joint axes, therefore, should be within acceptable range.

The custom made parts which can affect the pin joint axis parallelism and their important geometric features are shown in Figure 46. Sliding units of the linear guide system and pillow blocks for pin joints are supposed to be installed on moving blocks. The parallelism between pin joint axes is directly dependent on the perpendicularity of the two surfaces of the moving block, parallelism between two pin joint axes of each strut, and the parallelism between the three pin joint axes in spindle housing. Wire EDM process with one setup for each part is used to get high accuracy. In Figure 46, the inspection results are shown which show that the geometric accuracies are within $15\mu m$.

8.4 Standard machine elements

There are several standard machine elements such as, linear guide system, ball screw, and rolling bearing, incorporated in the MIT-SS-1. Linear guide system with cylindrical rollers and tapered roller bearing for passive joint are selected to increase the joint stiffness. In the case of lead screw, 5% preloaded nuts are used, and 1 pair of angular contact ball bearings are used for lead screw support. Standard part specifications and suppliers are listed in Table 4. Active joint configuration is shown in Figure 47.

8.5 Motion control

Four translational axes and one rotational axis are supposed to be installed in the MIT-SS-1. In this fabrication, 4-axis CNC milling machine without rotational axis (*A-axis*) is constructed because serial mechanism on horizontal plane is very common in commercial 5-axis CNC milling machines. Because the MIT-SS-1 incorporates 3-dof planar parallel mechanism on vertical plane and 1-dof translational axis on horizontal plane, the motion controller should be able to support at least 4 axes simultaneously.

Proportional Integral Derivative (PID) controllers are generally used for motion control with position feedback. Figure 48 shows the control system with feedback loop. K_P, K_I, and K_D are the

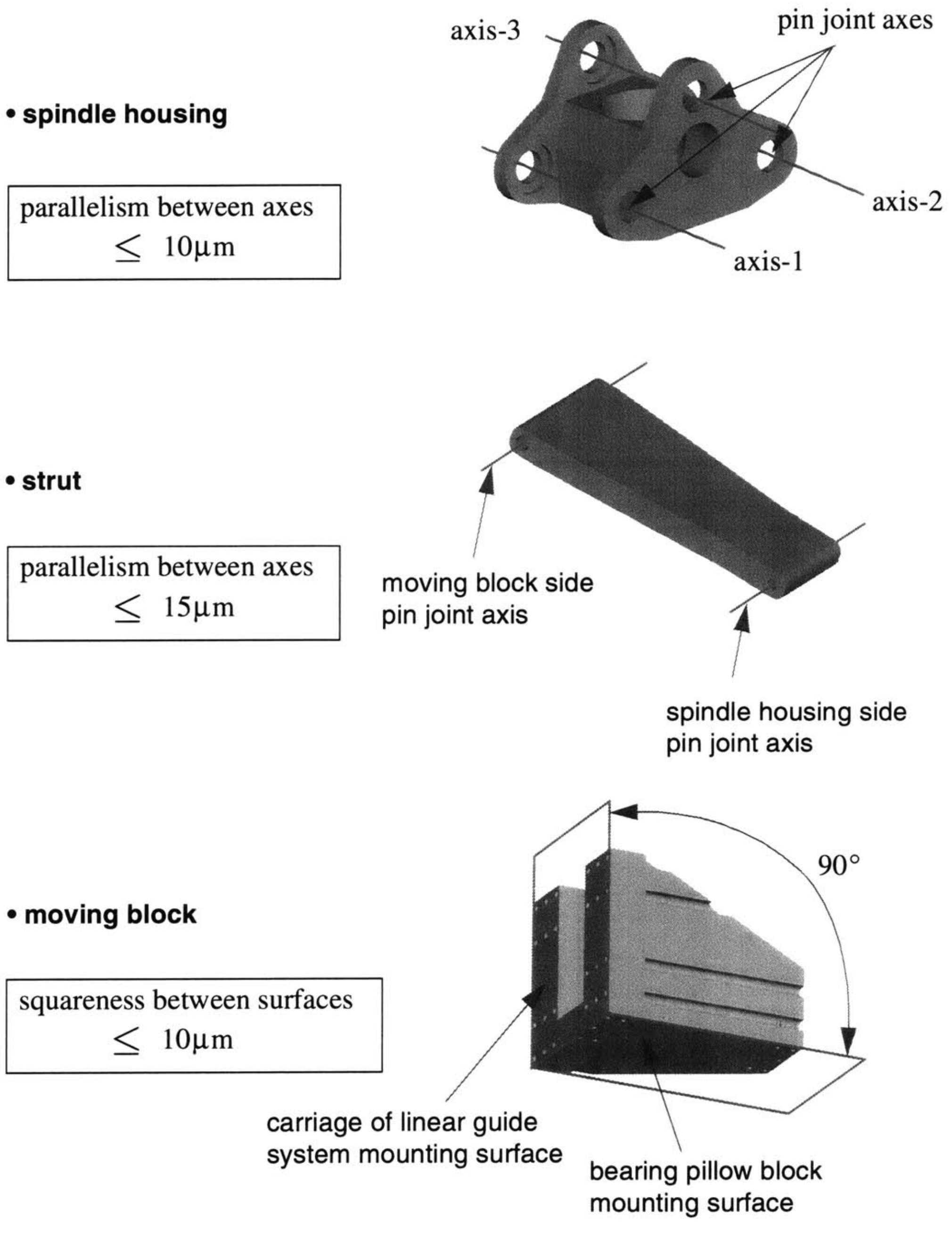

Figure 46 Parts machined by wire EDM process

standard components	Specification	Supplier
Linear guide system	Rail : $23mm \times 24.5mm$ Sliding unit: $70mm \times 30mm \times 98mm$	IKO
Ball lead screw	$\varnothing 20mm \times 10mm$	KURODA
Angular contact ball bearing	$d = 15mm, D = 42mm$ $\alpha = 45°$	NSK
Deep groove ball bearing	$d = 15mm, D = 35mm$	NSK
Flexible coupling	$k_t = 8070Nm/rad$	RIMTEC
Tapered roller bearing	$d = 15mm, D = 35mm$ $d = 20mm, D = 42mm$	NSK

Table 4: Standard machine components

PID gains which need to be adjusted according to the plant information such as, mass, compliance, and damping and to the performance requirement such as, overshoot, time constant, settling time, and steady state errors. Fixed PID gains during operation are very common in most motion controllers. The fixed gain PID controllers are used for systems whose parameters do not change seriously during operation. For example, the system parameters of Cartesian machine tool do not change seriously (except the mass of the workpiece) during machining. However, mass change of the workpiece which is reflected on actuator is very small because effective mass

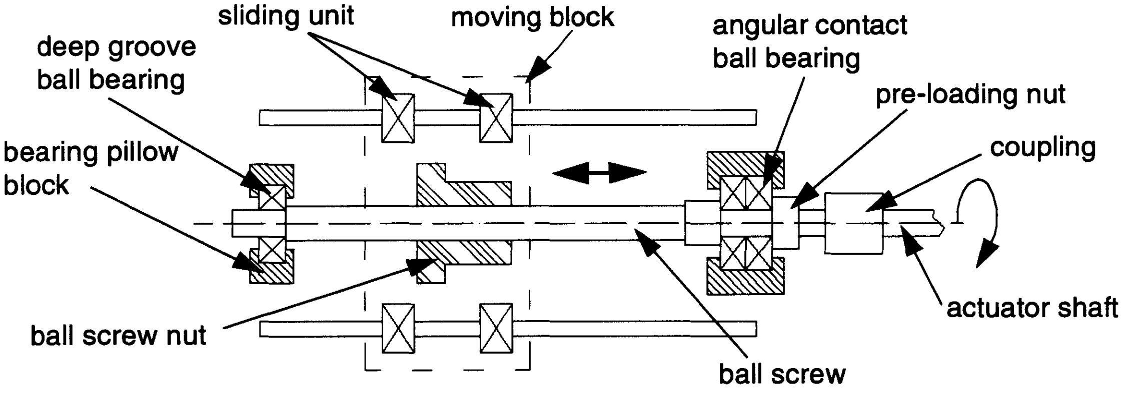

Figure 47 Ball lead screw and linear guide system configuration

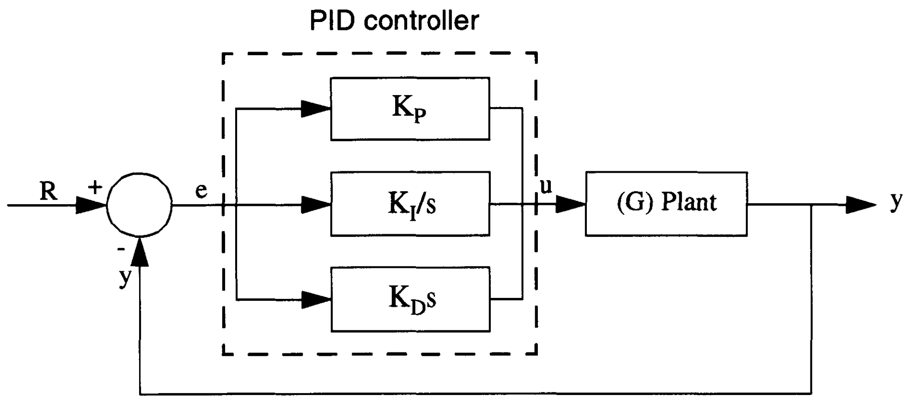

Figure 48 Block diagram of PID control system

of the workpiece is generally much smaller than the worktable so that the mass change of the workpiece can be considered negligible compared to the worktable, which results in fixed gain controller being suitable for most machine tool control.

In the case of parallel machines, inertia change reflected on actuators is generally not negligible as the end-effector moves in the workspace. PID controllers with variable gains are more proper for the MIT-SS-1. But such controllers cost over 20K US dollars and they are almost 10~15 times more expensive than controllers with fixed gains. Since our main interests are the kinematic properties and static/dynamic stiffness of the machine, motion controller with fixed gain, AEROTECH UNIDEX500, which can support four axes simultaneously, is selected for motion control. The detailed specifications of UNIDEX500 are shown in Appendix C.

8.6 Assembly

Assembly is the final stage of fabrication. Expected machine performance can not be achieved with poor assembly process even if the machine components are in perfect condition. In case of the MIT-SS-1, rail parallelism and pin joint axis parallelism are the most critical assembly issues. Left side of the vertical granite plane was used as a datum plane for rail installation. 1st rail which is closest to the datum plane was installed by using a spacer, from which $4\mu m$ parallelism could be achieved. The remaining rails were installed easily using dummy carriages. The holes for pin joints in the spindle housing were machined by wire EDM with one setup so that the alignment between holes was quite good. We used the holes as the datum line for the strut assembly. After all the struts are assembled with the spindle housing, the other ends of the struts were attached to the moving blocks.

During the assembly, we checked the over-constraints by moving the spindle housing with two assembled struts. If the over-constraint is beyond the limits, the force required to move the spindle should be high due to jamming in the joints. Joint jamming was checked by checking visual defects on the bearing races. Because no defects on the bearing surfaces were found, we could assume that the joints are working within allowable load ranges.

9 Experiments

Several tests with the MIT-SS-1 were performed for evaluation. In these experiments, the spindle is not attached to the end-effector. It may affect the performance, especially for tracking accuracy and dynamic stiffness. We considered its effect on static/dynamic stiffness. But the mass of the high speed spindle, IBAG HFK90S40C, is so small (7.1kg), about 6% of the strut and end-effector, we assume that the spindle effect on motion control is negligible.

9.1 Motion

We performed motion tests which included straightness test, repetability test, and tracking test with different feedrates. G-code is used for machine control. The linear displacement transducer, FASTER FS380, and a digital oscilloscope are used in this experiment. The detailed sensor specifications are shown in Appendix D. The saved data are transferred to a computer and visualized using Microsoft Excel.

9.1.1 Straightness of parallel structure in the MIT-SS-1

Before the performance of the MIT-SS-1 is tested, straightness along *x-axis* is checked. If the pin joint axes are not aligned well, the end-effector will deviate from the ideal straight line which is aligned with *x-axis*. The vertical granite plane is used as the datum plane for measurement. We can assume that the flatness of the granite within 100*mm* is practically zero because the flatness

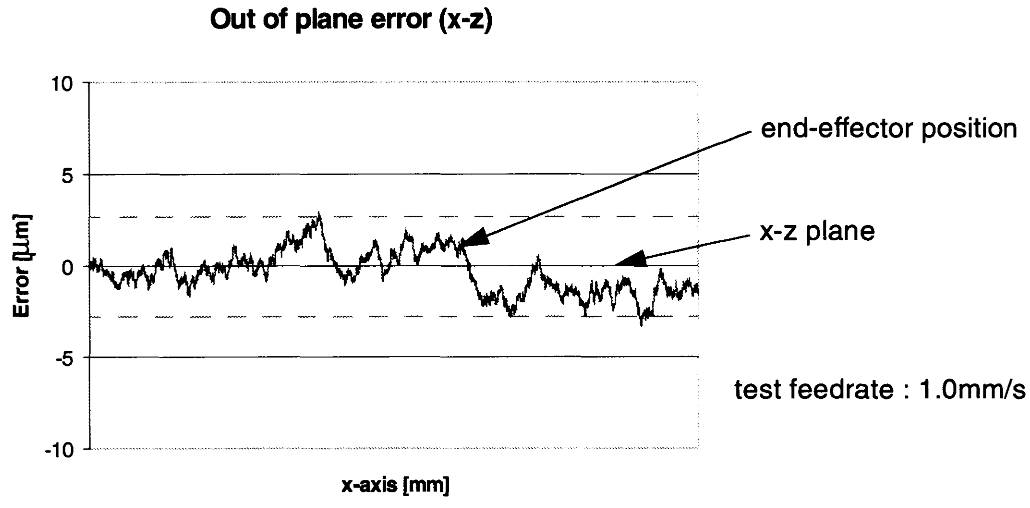

Figure 49 Straightness of the MIT-SS-1 along x-axis

of the whole vertical granite surface is about $4\mu m$. Figure 49 shows the test result with a feedrate of 1.0*mm/s*.

End-effector deviation from the *x-z* plane (vertical granite plane) was found to be within $+3\mu m$/-$3\mu m$. Several factors, such as pin joint shaft alignment, bearing eccentricity, and bearing clearance, could be the major sources of the end-effector errors. All passive joint bearings are assembled with interference fit using thermal shrinkage except between the joint shafts and pre-loading nut side inner race. There can be clearance between the bearing inner race and shaft, which can make the joint more compliant radially, which could be another major source of the errors. Their effects will be investigated in detail in future work.

9.1.2 Repeatability

Repeatability is defined as "the error between a number of successive attempts to move the machine to the same position" in [47]. The repeatability of the four linear axes were checked first, after which the end-effector repeatability was checked. Several end effector positions were selected to investigate the effect of different measuring positions. The measuring positions and directions are shown in Figure 50. After checking the position repeatability 10 times with $2\mu m$ minimum scale dial indicator at x = -0.1*m*, 0*m*, 0.1*m* and z = 0.1*m*, 0.2*m*, the maximum values were gathered to represent the repeatability.

The test results shown in Table 5 indicate that the repeatability is not dependent on end-effector position. In the case of the moving blocks and work-table, the repeatability was less than $2.0\mu m$, but the end-effector had about 2~ $4\mu m$ repeatability.

9.1.3 Tracking error

Ball bar test (BCD-00NCP) is the standard test method to check machine accuracy. When the end-effector of the machine moves along a circle on *x-y* plane, *x-z* plane, or *y-z* plane, it checks the radial displacement of the ball bar. Drawing a circle with cartesian machine is not an easy

$[\mu m]$

Measuring Point	1	2	3	4	5	6
End effector (x / z)	<4 / <2	<4 / <2	<4 / <2	<4 / <2	<4 / <2	<4 / <2
Moving block 1 (z)	<2	<2	<2	<2	<2	<2
Moving block 2 (z)	<2	<2	<2	<2	<2	<2
Moving block 3 (z)	<2	<2	<2	<2	<2	<2

Table 5: Repeatability test results

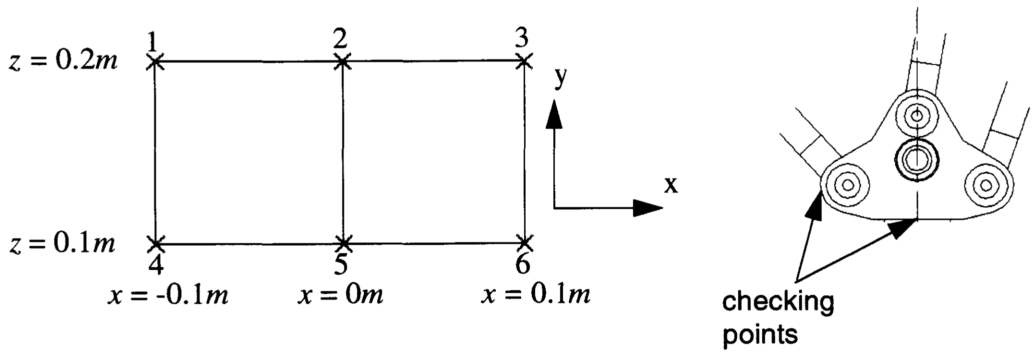

Figure 50 Measuring position for repeatability

task, because each axis feedrate changes according to the position to maintain constant end-effector feedrate. On the other hand, drawing lines with cartesian machine is relatively easy task for a controller. In case of parallel machines, there is no big difference between a circle and a line because the controller should coordinate each axis with variable feedrates not only for a line but for a circle.

Figure 51 shows each axis position history with a Cartesian machine and the MIT-SS-1 when they draw a 50*mm* circle on *x-z* plane and a 300*mm* line along *x-axis* with 10*mm/s* constant feedrate. In the case of drawing a circle, both mechanisms experience variable feedrates in all

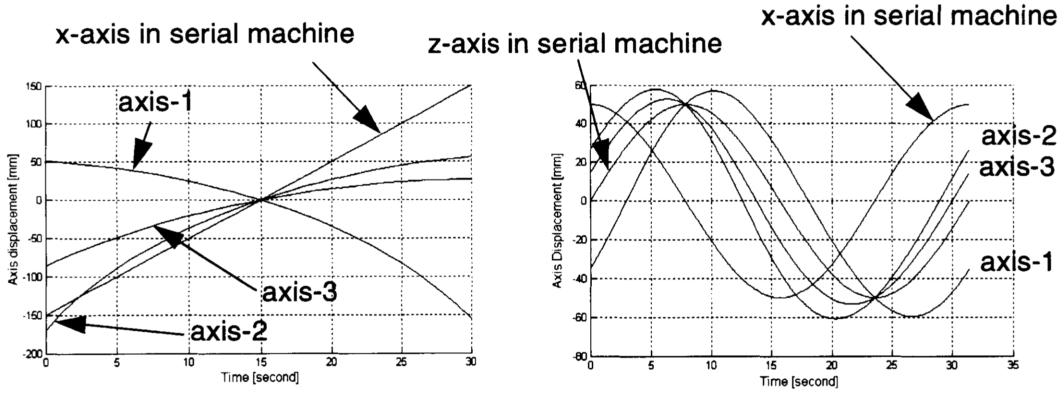

(a) case with a straight line along x-axis

(b) case with a circle on x-z plane

Figure 51 Axis time history of the MIT-SS-1 incorporated axes. In the case of drawing a line, the MIT-SS-1 experiences variable feedrates in all axes, but the feedrate in a cartesian machine remains constant.

Because there is no big difference between a line and a circle with the MIT-SS-1, we select a line to check the tracking ability. G-code for a straight line between $x = -50mm$ and $x = 50mm$ is created and used for the experiment of tracking error. The reference trajectory in Figure 52 shows the datum line which is generated by moving the end-effector along *x-axis*. The line is not a straight line but a curve. Since parts which are incorporated in the MIT-SS-1 are produced with manufacturing errors, G-code generated with the assumption that all parts are manufactured without errors, can not make the end-effector move along a perfect straight line. Deviation in vertical axis represents the end-effector errors along *z-axis*.

The datum line is created with 1.0*mm/s* feedrate. Tracking errors are investigated with increasing feedrate. Figure 52 shows that tracking errors with feedrates under 25mm/s are within $\pm 5 \mu m$. However, as the feedrate increases, the tracking errors increase and the end-effector becomes vibratory. The vibratory motion becomes obvious at feedrates higher than 100mm/s, and is accompanied with loud sound. Tracking errors also become larger.

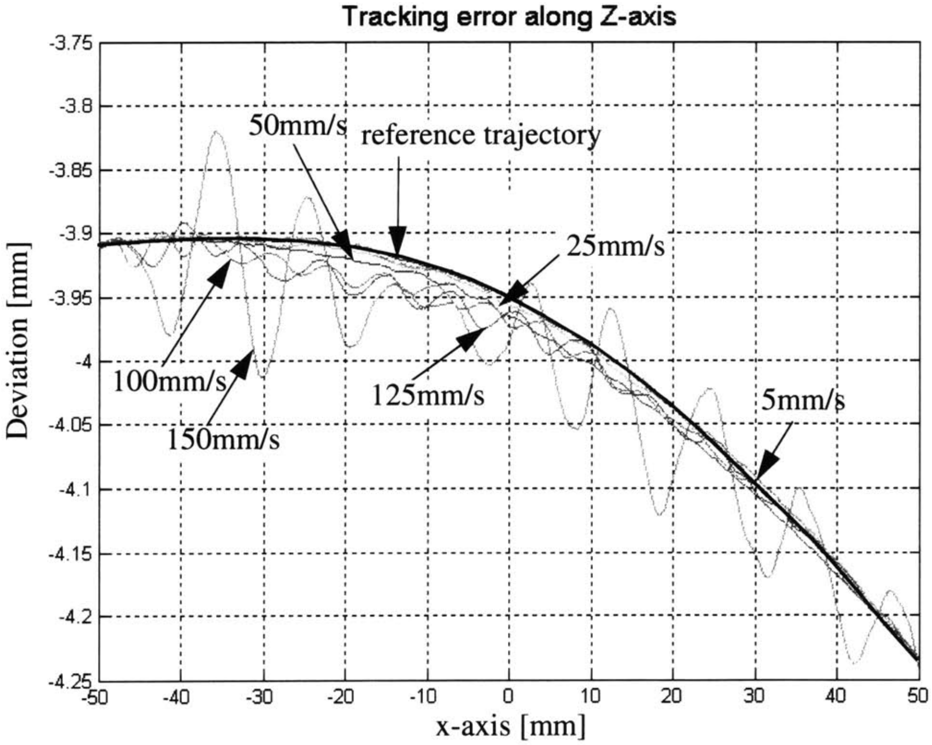

Figure 52 Tracking performance with different feedrates

The maximum achievable feedrate for this experiment is far below than the theoretical limit, 1.0m/s. PID gains are tuned with the auto axis tuning function and the gain is fixed during operation. Proper gains are, however, dependent highly on the end-effector position and orientation. To avoid the vibratory trajectory, proper gains should be assigned to the PID controller. It needs to be tested again with different gain values. We expect that better tracking performance with a straight line along *x-axis* would be achieved with higher gain values. In addition to the PID gain adjustment, we speculate that several factors can affect the tracking performance:

- More compliances than expected in joint bearing assembly.
- Higher harmonics in control signal.
- Controller saturation.
- Low modal frequency in testing device (sensor mounting device).

They will be investigated in future work.

9.2 Stiffness

We have performed static and dynamic stiffness tests on the MIT-SS-1. During the stiffness tests, all actuators are powered on to maintain the end-effector position and orientation with which we want to test because back drivable ball screws are incorporated in all axes.

9.2.1 Static stiffness

The MIT-SS-1 has the capability that the end-effector can tilt ±30° in whole 5-axis workspace. Stiffness tests were performed at the 5-axis workspace boundary and the mid-point. A 100N force was applied to the end-effector along *x-*, *y-*, and *z-axis* direction at each point 10 times. Because the test was performed without a spindle, we checked the deflection of the spindle housing shown in 53-(a). When the force is applied, it is found that there was a $2 \sim 4\mu m$ dead-zone in which the end-effector moved easily with small forces. We speculate that there are clearances between the joint shafts and the tapered roller bearing inner racers. The experimental data are collected after the dead-zone is passed, and averaged to represent the structural stiffness. Forces are applied with a spring scale and the end-effector displacements are checked with a dial indicator with $2\mu m$ resolution.

Table 6 and Figure 53-(b) show the test results. The stiffness at $x = -50mm$, $b = -30°$ and $x = 50mm$, $b = 30°$ are much smaller than at the other boundary points, which matches the trend of the numerical results shown in Chapter 6. In this test, the effects of the torsional stiffness on the translational deflection were neglected. Thus, we can expect that stiffness of the spindle

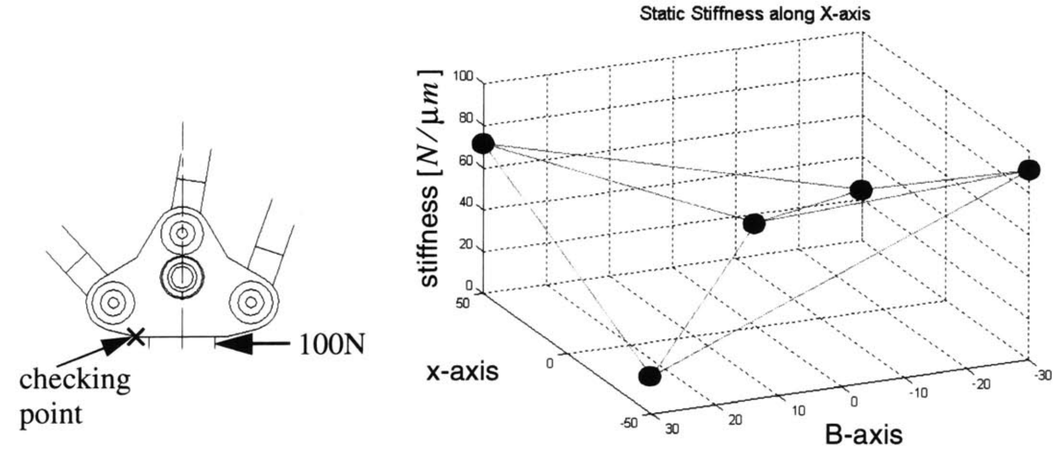

(a) stiffness test

(b) static stiffness results

Figure 53 Static stiffness test

end will be lower than the test results if the spindle, HFK 90S 40C, is attached. If the torsional stiffness, $K_{torsion}$, and the distance between a tilting center and the spindle end, t_{sp}, are known, resultant stiffness, K_r, can be obtained. If we assume that the spindle housing assembly can be considered as a 2nd order system with a mass and a spring, $K_{torsion}$ can be expressed as:

$$K_{torsion} = I_{sp}(2\pi \cdot f_{sp})^2 \quad (65)$$

x-axis [mm]	B-axis [degree]	Stiffness [μm]		
		x-axis	y-axis	z-axis
0	0	52.6	40.0	83.3
50	30	24.4	47.6	25.0
	-30	71.4	90.9	32.3
-50	30	17.5	52.6	23.3
	-30	90.9	76.9	76.9

Table 6: Static stiffness test results

where I_{sp} is a moment of inertia of the spindle housing and f_{sp} is its tilting mode frequency (which will be discussed in the next section). The equivalent stiffness of $K_{torsion}$ along *x-axis* can be written as $K_{eq} = K_{torsion}/t_{sp}^2$. Numerical value of K_{eq} is $6.46 \times 10^6 N/m$ with $t_{sp} = 70mm$. The K_{eq} and the test result can lead the resultant stiffness along *x-axis*. At $x = -50mm$ and $b = 30°$, the resultant stiffness, K_r, becomes $4.7N/\mu m$ which is much lower than the test result.

In the case of the stiffness along *y-axis*, there are no large stiffness variations because actuator singularity can not affect the stiffness along *y-axis*. In case of the *z-axis*, the structure is very stiff when the end-effector is placed at $x = 0mm$, $b = 0°$. This is because the force applied to the end-effector along *z-axis* is evenly distributed in all actuators. However, as the end-effector approaches the actuator singularity, it looses stiffness also.

9.2.2 Dynamic stiffness

Modal testing was performed to get the modal frequencies and mode shapes of the MIT-SS-1. The signal from the impact hammer, PCB 086C20, and from the accelerometer, PCB 356B08, is fed into the Hewlett-Packard signal analyzer, HP35670, which requires 10 time experiments to get reliable data. Finally, modal analysis software, STAR MODAL, shows the mode shapes and the modal frequencies using the data from the signal analyzer. Their detailed specifications are shown in Appendix D.

In the first experiment, 55 points on the structure were selected as shown in Figure 54. The results show that the modal frequencies of the work-table and the actuator support are higher than 400Hz and there are many modes between 100Hz and 300Hz which are coupled with other modes. Because of actuator noise, it was not easy to define the correct modal frequency range. We can get only several modal frequencies which include the strut assembly bending mode and the rigid body modes.

In the second experiment, we reduced the number of points where the accelerometer is placed to avoid the noise effect as much as possible. Figure 55 shows the 37 new points. With reduced test points, we could get clearer information.

Rigid body modes

The MIT-SS-1 is supported by 4 mounting devices installed at the bottom of the horizontal granite plane. It consists of a $\varnothing 100mm$ steel column and a M20 stainless steel bolt as shown in Figure 56. The mounting devices act like springs so that the whole structure vibrates like a rigid body and its frequencies are lower than the modal frequencies of the main structure. Four rigid body modes were found between 20Hz and 70Hz. Figure 57 shows the frequencies and the

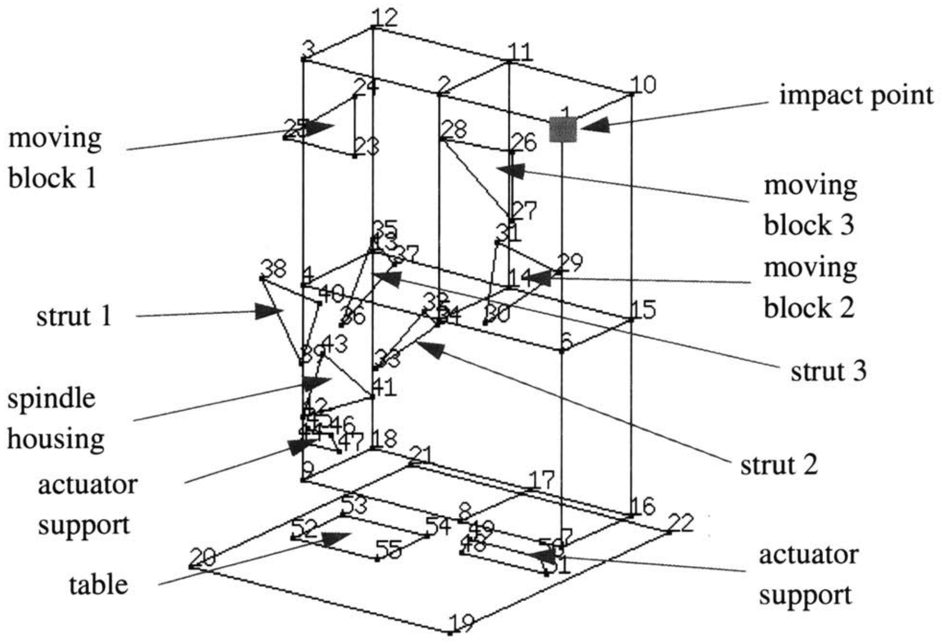

Figure 54 Modal test points at 1st experiment

directions of the vibration.

It is usually recommended that the rigid body mode should be low (< 20Hz) or high (200 ~ 500Hz) to avoid interference with the structural vibration. There may be several different rigid body modes above 70Hz, but modal frequencies for rigid body are not recognizable above 70Hz. The mounting device for the MIT-SS-1 needs to be modified to have lower or higher rigid body mode frequencies.

Structural modes

Many modes between 100Hz and 400Hz have so close modal frequencies that it is not easy to extract correct modes. Several mode shapes can be extracted from the frequency range where the resonances are clear. We could get 5 clear mode shapes which include the end-effector tilting mode, strut assembly bending mode, ball screw mode, granite frame bending mode, and granite frame twisting mode.

Figure 58 shows the spindle housing tilting mode with 79.2Hz of modal frequency which is lower than that from the numerical result, 113.24Hz, in Chapter 6. The experimental result implies that the stiffness of the tapered roller bearings incorporated in the spindle housing is lower than expected. If a spindle is attached, the moment of inertia of the spindle housing, I_{sp}, will be increased and the modal frequency will be decreased. The modal frequency with the

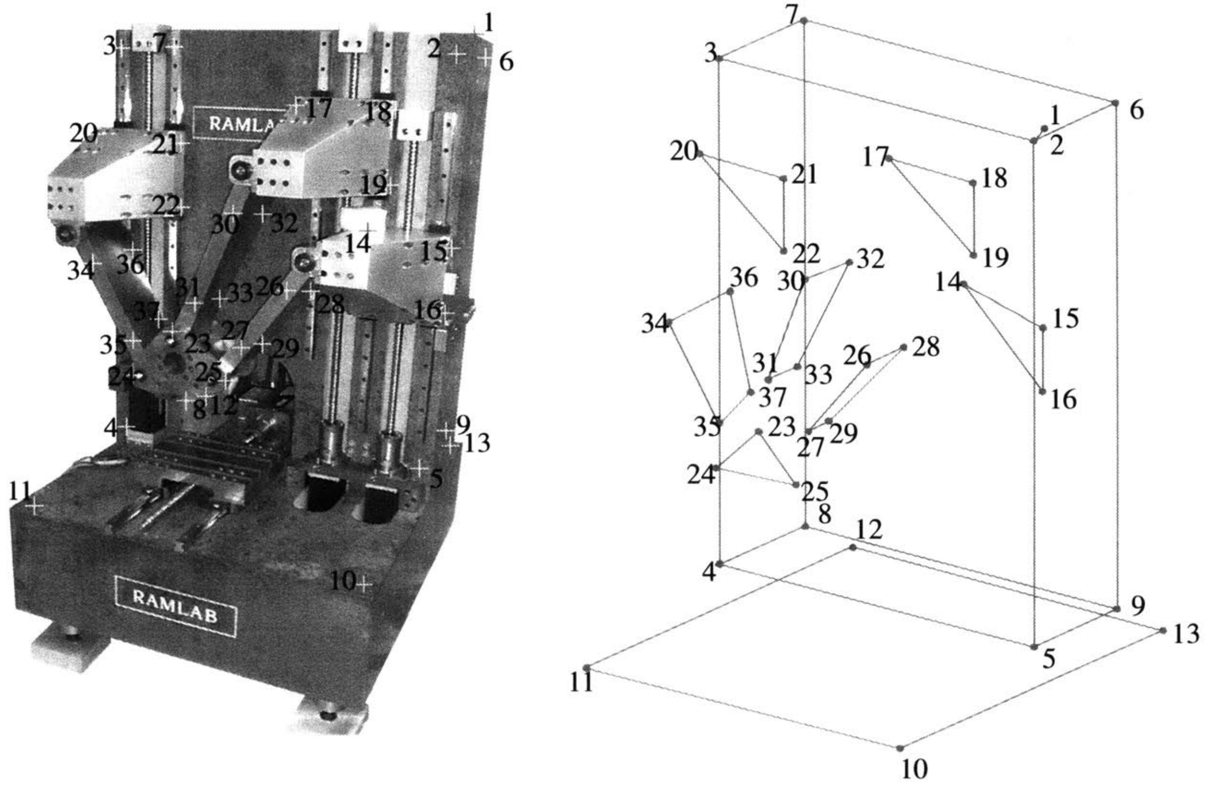

Figure 55 Modal test points

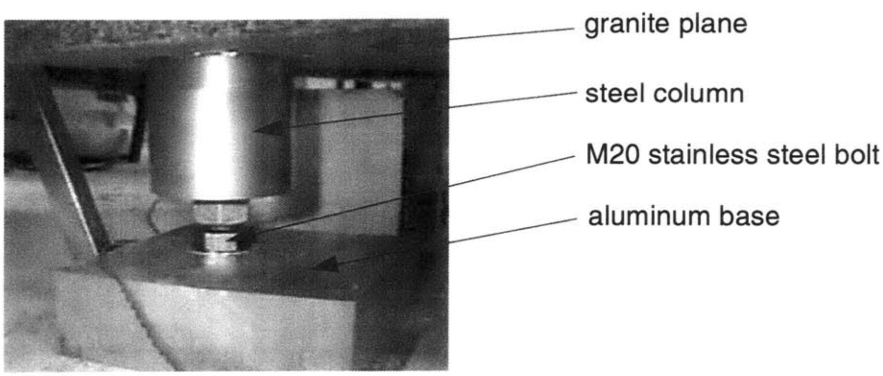

Figure 56 Mounting device of the MIT-SS-1

spindle, f_{sp}, can be predicted with new I_{sp} and the torsional stiffness as:

$$f_{sp} = \frac{1}{2\pi}\sqrt{\frac{K_{torsion}}{I_{sp}}}. \tag{66}$$

The numerical value of Equation 66 is 71.3 Hz which is about 10% lower than the modal testing result. Thus, a dynamic stiffness of the spindle housing will be decreased by amount of 10% when the spindle is attached. As indicated in previous section 9.2.1, the clearance fit between the shaft and the inner race at the pre-loading nut side of the spindle housing induces more compliance than the interference fit. Even though a spindle is attached, we expect that the structure will have high 1st mode frequency (about 70Hz), and can be considered as dynamically stiff.

An interesting mode is the strut assembly bending. Figure 59 shows the clear bending mode at 154.12Hz. It highly depends on the mass of the strut assembly which includes 3 struts and a spindle housing, and the stiffness of the bearings placed on the moving blocks. In this experiment, the spindle is not attached. However, the weight of the spindle is so small that its effect can be considered negligible. The stiffness of the real bearing joint is not stiff as we expect because of the same reason explained above. The numerical result is 182.38Hz.

The ball screws are supported by 1 pair of angular contact ball bearings. The moving block assembly which includes the end-effector, struts, moving blocks, and ball screw can vibrate along *z-axis*. Figure 60 shows the ball screw mode which is at 238.64Hz.

The ball screw modal frequency can be improved by increasing the joint stiffness. To increase the stiffness, there are 3 usual ways:

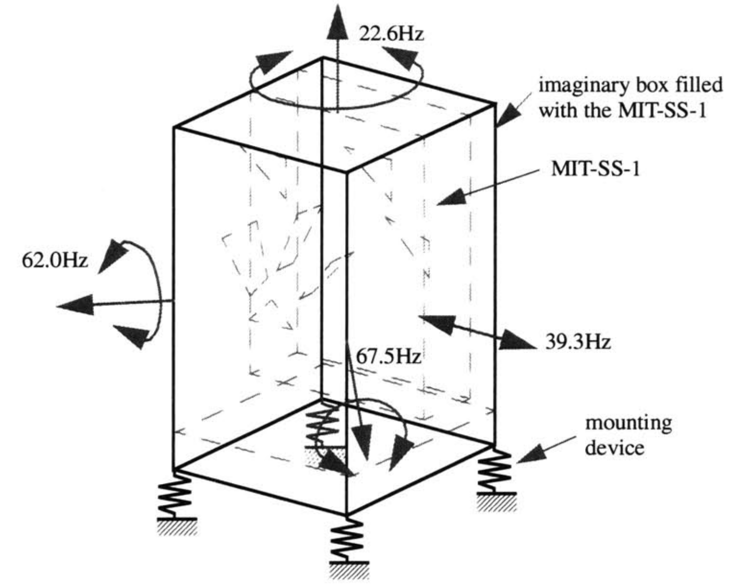

Figure 57 Rigid body modes of the MIT-SS-1

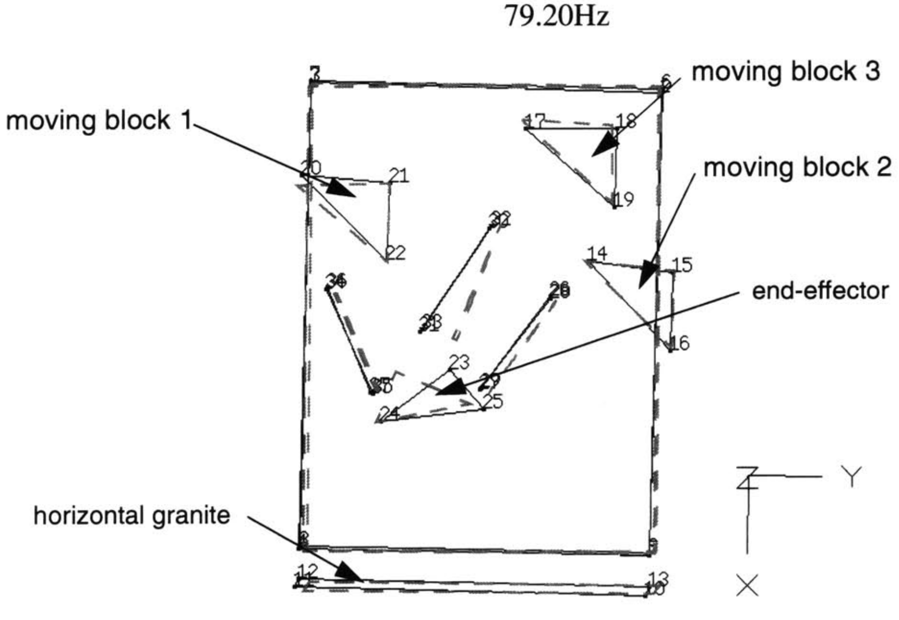

Figure 58 Spindle housing tilting mode

- Preloading the bearings
- Adding more bearings
- Using roller bearings

Configurations of applying preload and adding more angular contact ball bearings are shown in Figure 61. Applying preload increases the stiffness by a factor of two as shown in Fig 61-(a) and 61-(b). High preload can cause damage on the rolling elements easily, because the sum of the preload force and the external force can be above the allowable range. Before the bearings are preloaded, the resultant force applied to the rolling elements should be checked. Adding pairs of angular contact ball bearings also increases stiffness. If a pair of angular contact ball bearing is added, the joint becomes stiffer 2 times and about 1.4 times higher modal frequency can be achieved because the modal frequency is proportional to $\sqrt{stiffness}$. Using cylindrical roller thrust bearings can increase the joint stiffness. But when roller bearings are used, the maximum allowable rotating speed should be checked because limit speed of roller bearings is usually lower than that of ball bearings. The actuator, BM500E, incorporated in the MIT-SS-1, has peak speed of 8,000RPM, which does not permit roller bearing usage. In the case of the spherical roller thrust bearings, limiting speeds depend on the bearing size which are usually between 340 ~ 2600RPM [37].

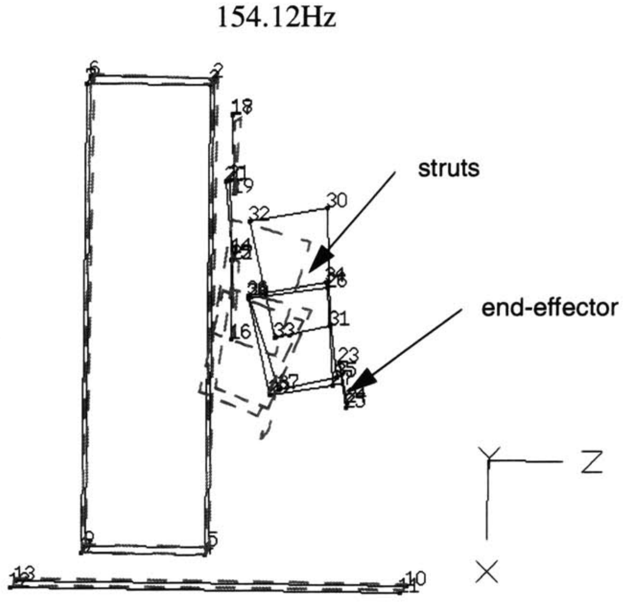

Figure 59 Bending mode of the strut assembly

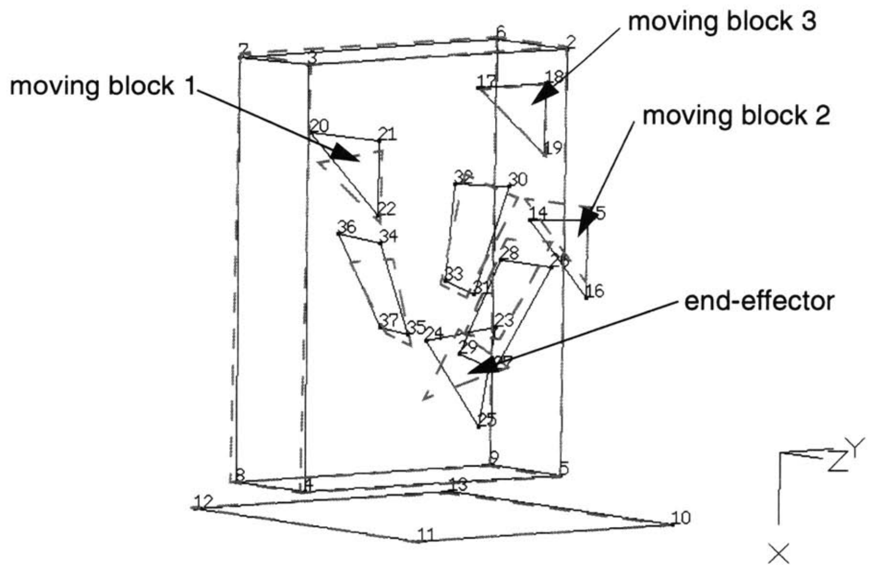

Figure 60 Moving block vibration mode along *z-axis*

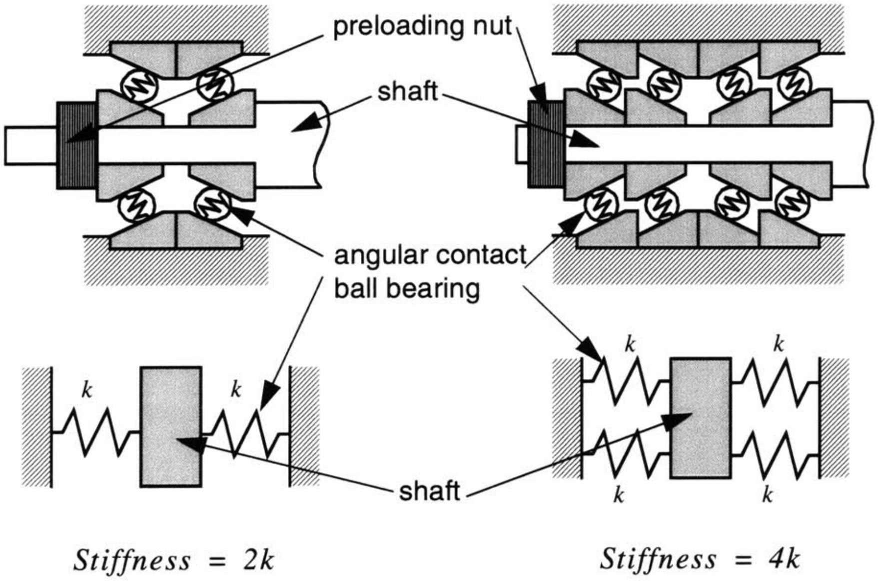

$Stiffness = 2k$

$Stiffness = 4k$

a) One pair configuration

b) Two pair configuration

Figure 61 Ball screw assembly configurations

Figure 62-(a) shows the granite frame bending modes. The vertical granite plane and the horizontal granite plane bend about *y-axis*. The experimental result of granite frame bending mode is 268.25Hz and the numerical result is 269.40Hz. The result from FEA is comparable to the result from experiment.

The granite frame twisting mode is shown in Figure 62-(b). The granite frame twists about *z-axis* with 319.95Hz modal frequency. The numerical result, shown in Figure 30, is 320.91Hz and it is almost same as the experimental results.

From the test results, we know that the granite vertical column and the horizontal base are well joined and they can be considered as one granite solid block. The granite modal frequency can be easily increased by increasing the column thickness or by adding guide bars to connect the granite column and the base at each side of the granite frame.

Furthermore, we know that the joint stiffness where the tapered roller bearings are installed is lower than expected. The joint stiffness can be improved with secure interference fit, and a higher modal frequency can therefore be achieved.

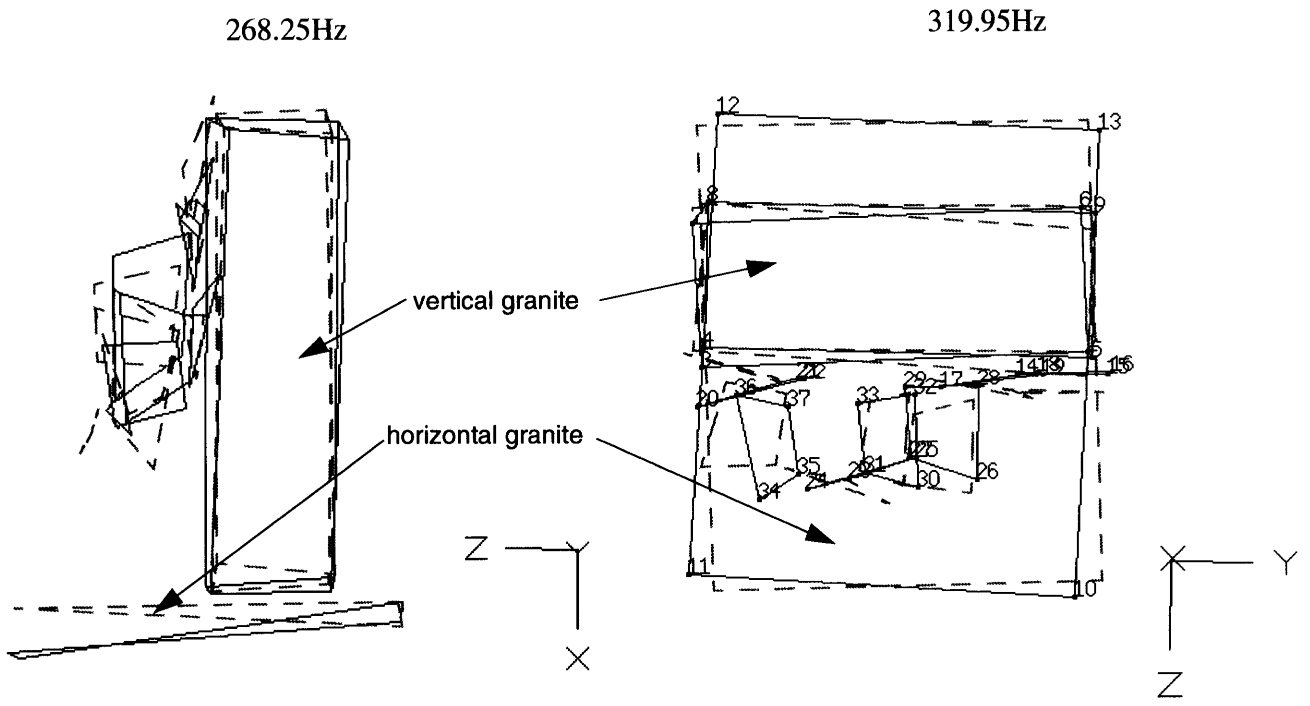

(a) Bending mode of granite frame

(b) Twisting mode of granite frame

Figure 62 Granite frame bending and twisting modes

10 Moving-Bridge 4-axis Machine

One of the important assets of PKM's is that they can have "one-sided" configuration. In other words, all the joints can be placed on one ceiling-type platform, which can be moved. When the hexapod first appeared, there was speculation about whether it could be mounted on a moving gantry or a 2D structure of high stiffness to machine large, 5-axis shapes like boat hulls and aerospace parts. This would correspond to a coarse-fine manipulation strategy common in robotics and precision engineering.

The same strategy can be applied to the MIT-SS-1 as we have described here. The 5-axis machine configuration is easily converted to a 4-axis configuration of almost unlimited length by reducing the serial 2-axis structure to a simple 1-axis stage. Alternatively, the planar PKM in the MIT-SS-1 may be attached to a moving bridge. In other papers [31], we have made the argument that most 5-axis tool paths can be reduced, in effect, to 4-axis tool paths. The 5th axis becomes important when the relative angle between the tool and the surface normal must be adjusted to control the physics of the cut. In high-speed situations, this angle must be adjusted to ensure that the cutting load, in terms of feed per tooth, remains constant during the cut. However, in large structures, this is less important, especially during hogging. In these situations, the moving bridge configuration, and the 4-axis reduction of this machine in general, are attractive configurations.

11 Conclusion

We have investigated the kinematic properties of parallel and serial mechanisms and pointed out several kinematic and structural challenges in the practical deployment of these machines. We have shown that the hybrid concept uses the advantages of serial and parallel mechanisms, and avoids most of their pitfalls, as we have shown. In particular, the hybrid machine can attain a relatively large workspace without compromising much on stiffness and manipulability, it can be configured in a way to avoid reversals in the workspace, it can be designed with well-understood revolute joints and linear guides, thus avoiding the problems of spherical joints and prismatic joints, and it can be designed with a relatively compact footprint.

We pointed out that a 3-dof planar parallel mechanism with wide struts cannot avoid over-constraints, and is sensitive to manufacturing tolerances. We showed that the effects of these over-constraints can be avoided by placing all the sliding joints on a single plane. However, the effects of these tolerances depend on the size of the structure, so that the hybrid planar mechanism is more applicable to small machine tools and does not scale well with size.

We have designed a small 5-axis CNC milling machine, the MIT-SS-1, which combines a 2-dof serial mechanism and a 3-dof planar type parallel mechanism based on these criteria. The effects of over-constraints are within acceptable ranges and the reversal characteristics of the MIT-SS-1 are the same as those of Cartesian machine tools on the x-y plane when there is no end-effector tilting. We can achieve a fairly good volume ratio between workspace and machine volume, low stiffness variation within the workspace, and a low moving inertia. From the numerical analysis, the 1st and 2nd mode frequencies of the MIT-SS-1 are as high as 111.2Hz and 182.3Hz, which implies that the MIT-SS-1 has the potential for high-speed machining.

We have constructed the working prototype of the MIT-SS-1. We could reduce the over-constraints in 3-dof planar parallel mechanism with one installation plane for linear guide systems and precise parts wire EDMed. The moving blocks are made of aluminum alloy and the machined surface can be easily damaged so that we had to assemble them with the sliding unit with much care. Joint bearings at the pre-loading nut side are assembled with light interference for adjusting the preload, but those at the granite vertical side are assembled with $10 \sim 20\mu m$ interference to enhance the stiffness. Although we could adjust the preload with ease, in this assembly, we loose the stiffness of the pre-loading side joints.

The MIT-SS-1was tested and evaluated. Modal analysis shows that the joints are not as stiff as expected. The 1st and 2nd mode frequencies are 79.2Hz and 154.12Hz which are lower than the numerical results. The joint stiffness at the pre-loading side can explain these differences. In case of the granite frame, the test results and the numerical results are almost identical, which implies that the granite frame is well constructed and assembled. Static stiffness is also lower than the numerical result for the same reason. We have checked the tracking performance. With feedrates lower than 0.1m/s (about 20% of the maximum achievable feedrate), the errors are within $10\mu m$. However, as the feedrate increases, the end-effector vibrates. The PID gain should be readjusted to get better tracking performance.

We have demonstrated that hybrid mechanisms are potentially attractive candidates for small 5-axis machine-tool applications. The test results with the MIT-SS-1, however, showed that the static/dynamic stiffness and the maximum feedrates with acceptable tracking accuracy were lower than expected. Secure interference fit in preloading side pin joints and non-linear controller proper for the systems with variable inertia effects need to be used in order that the MIT-SS-1 can be used for high speed machining (HSM) application.

12 Future Work

With the MIT-SS-1, we showed that the hybrid concept has a potential for 5-axis machine tool application. During the test and evaluation, we felt that further work, including issues in control and manufacturing, needs to be investigated. Following are suggestions for future work.

Error analysis

Part manufacturing error can affect the machining accuracy. It is, thus, needed to analyze the error sources and their effect on the accuracy. Error analyses have been performed only based on a Stewart Platform [40]. It is rare to find literature about error analysis of the 3-dof planar parallel mechanisms because it already constrains the motion to a plane. The errors in the parts of the MIT-SS-1 induce the out of plane errors. Understanding the error sources and their effects are critical to get high machining accuracy.

Motion control

PID control with fixed gains are common in machine tool motion control. The parameters of parallel mechanism vary according to the end-effector position and orientation. Therefore, the gain values need to be adjusted during machine operation. The MIT-SS-1 uses fixed gain PID controller, and we expect that better performance can be achieved with PID controller with adjustable gains during operation. Another approach is to use adaptive control with modelling uncertainty, which may be able to compensate for the inertia changes. Details about the adaptive control techniques can be found in conventional machine tool control literature[30,33,51].

Moving block feedback control

As indicated in Chapter 9, actuator encoder feedback is used for position control. The ball screw support system compliance can affect the moving block position accuracy on which the end-effector accuracy depends directly. Better accuracy can be obtained with moving block position feedback. However, this needs more sophisticated control technique to prevent instability problem.

Cutting test

Many parameters will be involved in real cutting. Damping, vibration, and thermal expansion may be the major interests of most machine tool designers. The MIT-SS-1 needs to be evaluated with real cutting tests and geometric accuracy according to the standard ASME B5.54 which is the standard of the conventional machine tool performance evaluation [5,49].

Reference

[1] Alexander, R. M., "Body Support, Scaling, and Allometry," in Functional Vertebrate Morphology, Ed. Hildebrand, M., Bramble, D. M., Liem, K. F., Wake, D. B., Belknap Harvard, Cambridge, Massachusetts, pp. 26-37.

[2] Armstrong, B., Neevel, D. and Kusik, T., "New results in NPID control: Tracking, Integral Control, Friction Compensation and Experimental Results," IEEE Transactions on control systems technology, Vol.9, No.2, March 2001.

[3] Armstrong-Helouvry, B., Dupon, P., "Friction modelling for control," Proc. of the American Control Conference, San Francisco, June 1993.

[4] Armstrong-Helouvry, B., Dupon, P. and Canudas De Wit, C., "A survey of models, analysis tools and compensation methods for the control of machine with friction," Automatica, Vol. 30 No. 7, pp. 1083-1138, 1994.

[5] ASME, "Method for Performance Evaluation of Computer Numerically Controlled Machining Centers", The American Society of Mechanical Engineers, 1992.

[6] Bonev, I., http://wwwrobot.gmc.ulaval.ca/~bonev/Bookmarks.html

[7] Dahl, P. R., "Measurement of solid friction parameters of ball bearings," Proc. of 6th Annual Symp. on Incremental Motion Control System and Devices, University of Illinois, 1977.

[8] El-Khasawneh, B. S. and Ferreira, P.M., "On Using Parallel Link Manipulators as Machine Tools," Transactions of NAMRAC XXV, pp 305-310, 1997

[9] El-Khasawneh, B. S. and Ferreira, P.M., "The Tetrahedral Tripod," in Parallel Kinematic Machines: Theoretical Aspects and Industrial Requirements, C.R. Boër, L. Molinari-Tosatti, and K.S. Smith, eds. (Springer-Verlag, 1999), pp419-430

[10] Fassi, I. and Wiens, G. J., "Multiaxis Machining: PKMs and Traditional Machining Centers," J. of Manufacturing Process, Vol. 1/No.2, 2000, pp 79-92

[11] Ferreira, P., Personal Conversation. Milan, Italy, September 1999.

[12] Gosselin, C. and Angeles, J., "Singularity Analysis of Closed Loop Kinematic Chains," ASME Journal of Mechanical Design (v112, n3, 1990), pp331-336.

[13] Gosselin, C. and Angeles, J., "The Optimum Kinematic Design of a Planar Three-Degrees-of-Freedom Parallel Manipulator," J. of Mechanisms, Transmissions, and Automation in Design, Vol. 110, March 1988.

[14] Hardage D. S. and Wiens, G., "Modal Analysis and Modeling of a Parallel Kinematic Machine," 1999 IMECE Proc. of ASME: Mfg. Science and Eng., MED-v8, Nashville, TN, Nov. 14-19, 1999, 6 pp.90

[15] Harris, Tedric A., Rolling bearing analysis, 2nd edition, New York: Wiley, 1984.

[16] Hebsacker, M., Treib, T., Zirn, O. and Honegger, M., "Hexaglide 6 DOF and Triaglide 3 DOF Parallel Manipulators," in Parallel Kinematic Machines: Theoretical Aspects and Industrial Requirements, C.R. Boër, L. Molinari-Tosatti, and K.S. Smith, eds. (Springer-Verlag, 1999), pp345-355

[17] Heisel, U., "Precision Requirements of Hexapod-Machines and Investigation," in Parallel Kinematic Machines: Theoretical Aspects and Industrial Requirements, C.R. Boër, L. Molinari-Tosatti, and K.S. Smith, eds. (Springer-Verlag, 1999), pp131-150

[18] Houghton, P. S., Ball and Roller Bearings, Applied Science Publishers, 1976.

[19] Huang, T., Whitehouse, D. J. and Wang, J., "The Local Dexterity, Optimal Architecture and Design Criteria of Parallel Machine Tools," Annals of the CIRP (v47/1, 1998).

[20] Innocenti, C. "Forward Kinematics in Polynomial Form of the General Stewart Platform," Paper No. DETC98/MECH-5894, Proc. of 1998 ASME Design Eng. Technical Conf., Atlanta, GA.

[21] Innocenti, C. and Parenti-Castelli, V., "Forward Kinematics of the General 6-6 Fully Parallel Mechanism: An Exhaustive Numerical Approach via a Mono-Dimensional-Search Algorithm," Robotics, Spatial Mechanisms, and Mechanical Systems (ASME DE-v45, 1992), pp545-552.

[22] Innocenti, C. and Parenti-Castelli, V., "Exhaustive Enumeration of Fully Parallel Kinematic Chains," Dynamic Systems and Control, ASME (v2, 1994).

[23] Ji, Z. "Analysis of Design Parameters in Platform Manipulators," ASME Journal of Mechanical Design (v118, n4, 1996), pp526-531.

[24] Kalpakjian, S., Manufacturing Engineering and Technology, 3rd Ed., Addison-Wesley, 1995.

[25] Kargert, Adolf and Husty, Manfred, "Classification of All Self-Motions of The Original Stewart-Gough Platform," Computer-Aided Design, Vol. 30, No. 3,pp. 205-215,1998.

[26] Kato, S., Sato, N. and Matsubayashi, T., "Some considerations of characteristics of static friction of machine tool slideway," Journal of Lubrication Technology, 94(3), 234-247,1972.

[27] Kim, J. W., Park, C., Kim J. and Park, F. C., "Performance Analysis of Parallel Manipulator Architectures for CNC Machining Applications," MED-Vol.6-2, Manufacturing Science and Technology Vol.2, ASME 1997, pp341-348

[28] Kim, T. and Sarma, S. E., "Toolpath Generation along Directions of Maximum Kinematic performance; a First Cut at Machine-optimal Paths," Computer-Aided Design, pp. 453-468, May 2002.

[29] Kosuge, K., Okuda, M., Kawamata, H. and Fukuda, T., "Input/Output Force Analysis of Parallel Link Manipulators," Proc. of IEEE Int. Conference on Robotics and Automation, 1993, pp714-719

[30] Lauderbaugh, L. K. and Ulsoy, A. G., "Dynamic Modeling for Control of the Milling Process," ASME Journal of Eng. for Industry (v110, n4, 1988), pp367-375.

[31] Mahadevan, B., Sarma, S. E. and Marciniak, K. "Collision-Free Finishing Tool Paths from Visibility Data," Accepted for publication in Computer-Aided design. To appear in 2002.

[32] Martone, R. and Roth, B., "The Effects of Actuation Schemes on the Kinematic Performance of Manipulators," Trans. of ASME, Vol. 119, June 1997, pp212-217

[33] Masory, O. and Koren, Y., "Stability Analysis of a Constant Force Adaptive Control System for Turning," ASME Journal of Eng. for Industry (v107, n1, 1985), pp295-300.

[34] Merlet, J., Gosselin, C. and Mouly, N., "Workspace of Planar Parallel Manipulators," Mech. Mach. Theory Vol. 33, No. 1/2, 1998.

[35] Molinari-Tosatti, L., Bianchi, G., Fassi, I., Boër, C. and Jovane, F., "An Integrated Methodology for the Design of Parallel Kinematic Machines (PKM)," Annals of the CIRP (v47, 1998), pp341-345.

[36] Murray, R. Li, Z. and Sastry, S., A Mathematical Introduction to Robotic Manipulation, CRC Press, 1994

[37] NSK Corporation, Bearing Replacement Guide, 1998.

[38] Ohnishi, K., Shibata, M. and Murakami, T., "Motion control for advanced mechatronics," IEEE/ASME Transactions on mechatronics, Vol.1, No.1, March 1996.

[39] Park, F. C. and Kim, J. W., "A Singularity Classification for Closed Chains," Advances in Robot Kinematics: Analysis and Control, Lenarcic and Husty, M. L. (eds.), pp. 483-492, Kluwer Academic Publisher, 1998.

[40] Patel, A. and Ehmann, K. F., "Volumetric Error Analysis of a Stewart Platform Based Machine Tool," Annals of the CIRP (v46/1, 1997), pp287-290.

[41] Pierrot, F. and Shibukawa, T., "From Hexa to HexaM," in Parallel Kinematic Machines: Theoretical Aspects and Industrial Requirements, C.R. Boër, L. Molinari-Tosatti, and K.S. Smith, eds. (Springer-Verlag, 1999), pp357-364

[42] Pritschow, G. and Wurst, K-H., "Systematic Design of Hexapods and Other Parallel Link Systems," Annals of the CIRP (v46/1, 1997), pp291-295.

[43] Rabinowicz, E., "A study of the stick-slip process," In R. Davies(Ed.), Friction and Wear, Elsevier, NY.

[44] Salisbury, J. K. and Craig, J. J., "Articulated Hands: Force Control and Kinematic Issues," The Int. Journal of Robotics Research, Vol. 1, No. 1, Spring 1982, pp4-17

[45] Sefrioui, J. and Gosselin, C., "Singularity Analysis and Representation of Planar Parallel Manipulators," Robotics and Autonomous Systems, October 1992.

[46] SKF USA Inc., General Catalog, 1999.

[47] Slocum, A., Precision Machine Design, Society of Manufacturing Engineers; ISBN: 0872634922. 1992.

[48] Southward, S., Radcliffe, C. and MacCluer, C., "Robust nonlinear stick-slip friction compensation," ASME J. of Dynamic Systems, Measurement, and Control, Vol. 113, pp. 639-645, 1991.

[49] Tlusty, J., Smith, S. and Zamudio, C., "Evaluation of Cutting Performance of Machining Centers," Annals of the CIRP (v40/1, 1991), pp405-410.

[50] Tlusty, J., Ziegert, J. and Ridgeway, S., "Fundamental Comparison of the Use of Serial and Parallel Kinematics for Machines Tools," Annals of the CIRP (v48/1, 1999), pp351-356.

[51] Tomizuka, M. and Zhang, S., "Modeling and Conventional/Adaptive PI Control of a Lathe Cutting Process," ASME Journal of Dynamic Systems, Measurement, and Control (v110, n4, 1988), pp350-354.

[52] Tonshoff, H. K. and Grendel, H., "A Systematic Comparison of Parallel Kinematics," in Parallel Kinematic Machines: Theoretical Aspects and Industrial Requirements, C.R. Boër, L. Molinari-Tosatti, and K.S. Smith, eds. (Springer-Verlag, 1999), pp295-312

[53] Tooling and Production Magazine, Putting the Hex(apod) on Machining, Tooling and Production Magazine, September, 1996, pp37-42

[54] Tsai, L. W., "Systematic Enumeration of Parallel Manipulators," in Parallel Kinematic Machines: Theoretical Aspects and Industrial Requirements, C.R. Boër, L. Molinari-Tosatti, and K.S. Smith, eds. (Springer-Verlag, 1999), pp 33-49

[55] Tu, Q. and Rastegar, J., "On the inherent characteristics of the dynamics of rigid link robot manipulators," Mechanism and Machine Theory, Vol. 34, pp. 171-191, 1999.

[56] Tung, E. D., "Identification and control of high-speed machine tools," Doctoral thesis in Mechanical Engineering, U.C. Berkeley, 1993.

[57] Waldron, K. J., "Design of Walking Machines," in Human and Machine Lcomotion, ed. Morecki, A. and Waldron, K. J., Springer Verlag, 1997, pp. 283-315.

[58] Waldron, K.J. and Hubert, C., "Scaling of Robotic Mechanisms," Proceedings of the 2000 IEEE International Conference on Robotics and Automation, Volume 1, 2000, Page(s) 40-45 San Francisco, CA, April 2000

[59] Walrath, C. D., "Adaptive bearing friction compensation based on recent knowledge of dynamic friction," Automatica, Vol. 20 No. 20, pp. 717-727, 1984.

[60] Wenger, Ph. and Chablat, D., "Workspace and Assembly Modes in Fully-Parallel Manipulators: A Descriptive Study," Advances in Robot Kinematics: Analysis and Control, Lenarcic and Husty, M. L. (eds.), pp. 117-126, Kluwer Academic Publisher, 1998.

[61] Wiens, G. and Walker, C., "Hexapod Machine Tool Error Analysis with Inclusion of System Dynamics," 1998 IMECE Proc. of the ASME: Mfg. Science and Eng., Anaheim, CA, Nov. 15-20, 1998, MED-v8, pp. 705-713.

[62] Yuan, L. and Rastegar, J., "Optimal integration of smart actuators in parallel and cooperating robots to enhance operating speed and accuracy," Proc. of ASME 2001 Design Engineering Technical Conference, Pittsburgh, PA, September 9-12, 2001.

[63] Yoshikawa, T., "Manipulability of Robotic Mechanisms," The Int. Journal of Robotics Research, Vol. 4, No. 2, Summer 1985, pp3-9

[64] Zhang, D. and Gosselin, C., "Kinetostatic Modelling of N-DOF Parallel Mechanisms with a Passive Constraining Leg and Prismatic Actuators." Journal of Mechanical Design, Vol. 123, September 2001.

Appendix A

- **Hexapod information**

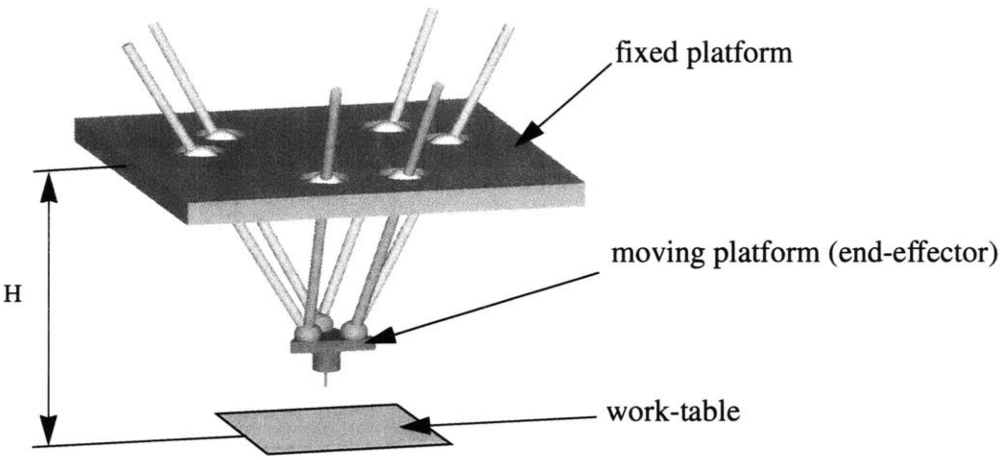

(a) 6 x 3 type Hexapod

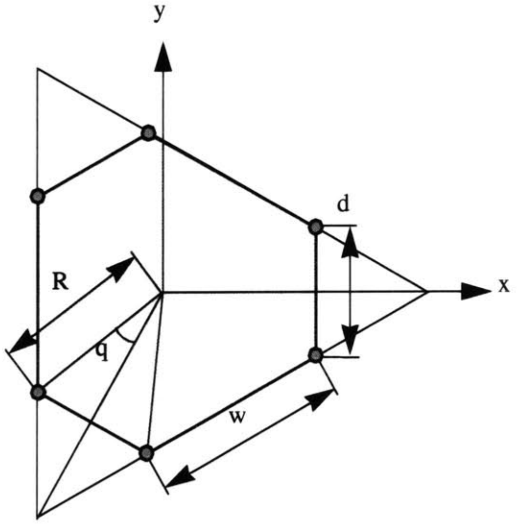

(b) fixed platform

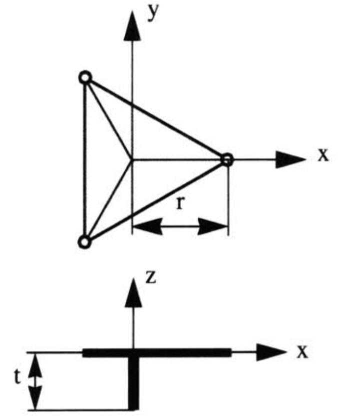

(c) moving platform

Dimension: [m]

w=0.66m r=0.175m
d=0.25m H=1.2m
t=0.2m

Appendix B

- **Inverse Jacobian of the MIT-SS-1**

$$J^{-1}(1,1) = \frac{s_{1x}}{\sqrt{(l_1^2 - s_{1x}^2)}},\ J^{-1}(2,1) = \frac{s_{2x}}{\sqrt{(l_2^2 - s_{2x}^2)}},\ J^{-1}(3,1) = \frac{s_{3x}}{\sqrt{(l_3^2 - s_{3x}^2)}},$$

$$J^{-1}(4,1) = 0,\ J^{-1}(5,1) = 0$$

$$J^{-1}(1,2) = -sin(a),\ J^{-1}(2,2) = -sin(a),\ J^{-1}(3,2) = -sin(a),$$

$$J^{-1}(4,2) = -cos(a),\ J^{-1}(5,2) = 0$$

$$J^{-1}(1,3) = cos(a),\ J^{-1}(2,3) = cos(a),\ J^{-1}(3,3) = cos(a),$$

$$J^{-1}(4,3) = -sin(a),\ J^{-1}(5,3) = 0$$

$$J^{-1}(1,4) = -y^w cos(a) - z^w sin(a) - h_2 sin(a),$$

$$J^{-1}(2,4) = -y^w cos(a) - z^w sin(a) - h_2 sin(a),$$

$$J^{-1}(3,4) = -y^w cos(a) - z^w sin(a) - h_2 sin(a),$$

$$J^{-1}(4,4) = y^w sin(a) - z^w cos(a) - h_2 cos(a),\ J^{-1}(5,4) = -1$$

$$J^{-1}(1,5) = rcos(b) - tsin(b) + \frac{s_{1x}}{\sqrt{(l_1^2 - s_{1x}^2)}}(rsin(b) + tcos(b)),$$

$$J^{-1}(2,5) = -rcos(b) - tsin(b) - \frac{s_{2x}}{\sqrt{(l_2^2 - s_{2x}^2)}}(rsin(b) - tcos(b)),$$

$$J^{-1}(3,5) = -(t+p)sin(b) + \frac{s_{3x}}{\sqrt{(l_3^2 - s_{3x}^2)}}(t+p)cos(b),$$

$$J^{-1}(4,5) = 0,\ J^{-1}(5,5) = 0$$

Dimension

$w_1 = 0.2975m,\ w_2 = 0.3075m,\ w_3 = 0.1575m$

$l_1 = 0.4m,\ l_2 = 0.4m,\ l_3 = 0.475m$

$h_1 = 0.1m,\ h_2 = 0.1m$

$t = 0.15m,\ r = 0.095m,\ p = 0.095m$

- **Inverse Jacobian of the sliding units**

Jacobian for the moving block deflections, J_{tr}, can be obtained by considering w_1, w_2, w_3 as variables and fixing θ_1, θ_2, θ_3 as constants. Differentiating Equations 43, 44, and 45 with respect to time leads:

$$0 = \dot{z} + (r cos(b) - t sin(b))\dot{b} - \frac{s_{1x}}{\sqrt{(l_1^2 - s_{1x}^2)}}(\dot{s}_{1x})$$

where $\dot{s}_{1x} = -\dot{w}_1 - \dot{x} - (r sin(b) + t cos(b))\dot{b}$,

$$0 = \dot{z} - (r cos(b) + t sin(b))\dot{b} - \frac{s_{2x}}{\sqrt{(l_2^2 - s_{2x}^2)}}(\dot{s}_{2x})$$

where $\dot{s}_{2x} = \dot{w}_2 - \dot{x} + (r sin(b) - t cos(b))\dot{b}$,

$$0 = \dot{z} - (t + p) sin(b)\dot{b} - \frac{s_{3x}}{\sqrt{(l_3^2 - s_{3x}^2)}}(\dot{s}_{3x})$$

where $\dot{s}_{3x} = \dot{w}_3 - \dot{x} - (t + p) cos(b)\dot{b}$.

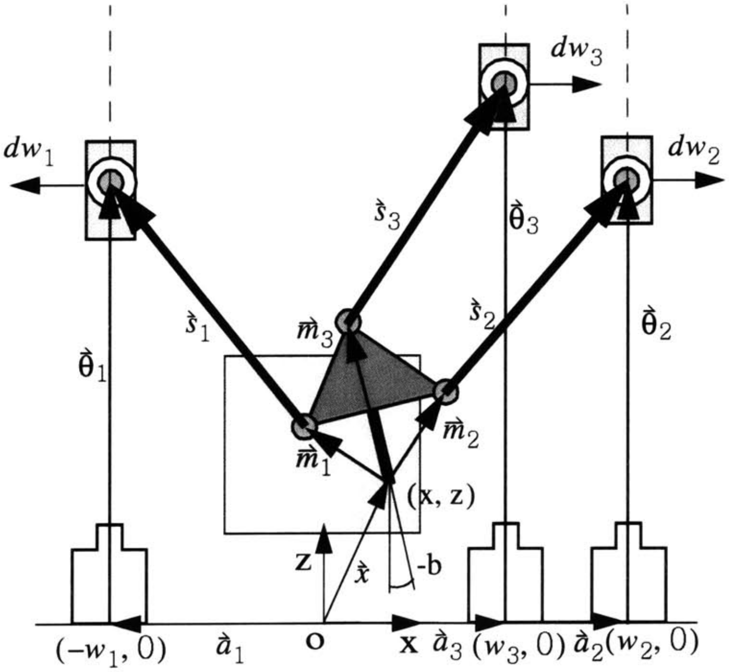

A parallel structure on the vertical plane of the MIT-SS-1

With the previous equations, Equation 46, and 47, J_{tr} can be obtained as:

$$\begin{bmatrix} \dot{w}_1 \\ \dot{w}_2 \\ \dot{w}_3 \\ \dot{\theta}_4 \\ \dot{\theta}_5 \end{bmatrix} = J_{tr}^{-1} \begin{bmatrix} \dot{x}^w \\ \dot{y}^w \\ \dot{z}^w \\ \dot{a} \\ \dot{b} \end{bmatrix}$$

where

$$J_{tr}^{-1}(1,1) = -1,$$

$$J_{tr}^{-1}(1,2) = sin(a)\left(\frac{s_{1x}}{\sqrt{(l_1^2 - s_{1x}^2)}}\right)^{-1}, J_{tr}^{-1}(1,3) = -cos(a)\left(\frac{s_{1x}}{\sqrt{(l_1^2 - s_{1x}^2)}}\right)^{-1},$$

$$J_{tr}^{-1}(1,4) = (y^w cos(a) + (z^w + h_2) sin(a))\left(\frac{s_{1x}}{\sqrt{(l_1^2 - s_{1x}^2)}}\right)^{-1},$$

$$J_{tr}^{-1}(1,5) = -(r cos(b) - t sin(b))\left(\frac{s_{1x}}{\sqrt{(l_1^2 - s_{1x}^2)}}\right)^{-1} - r sin(b) - t cos(b).$$

$$J_{tr}^{-1}(2,1) = 1,$$

$$J_{tr}^{-1}(2,2) = -sin(a)\left(\frac{s_{2x}}{\sqrt{(l_2^2 - s_{2x}^2)}}\right)^{-1}, J_{tr}^{-1}(2,3) = cos(a)\left(\frac{s_{2x}}{\sqrt{(l_2^2 - s_{2x}^2)}}\right)^{-1},$$

$$J_{tr}^{-1}(2,4) = -(y^w cos(a) + (z^w + h_2) sin(a))\left(\frac{s_{2x}}{\sqrt{(l_2^2 - s_{2x}^2)}}\right)^{-1},$$

$$J_{tr}^{-1}(2,5) = -(r cos(b) + t sin(b))\left(\frac{s_{2x}}{\sqrt{(l_2^2 - s_{2x}^2)}}\right)^{-1} - r sin(b) + t cos(b).$$

$$J_{tr}^{-1}(3,1) = 1,$$

$$J_{tr}^{-1}(3,2) = -sin(a)\left(\frac{s_{3x}}{\sqrt{(l_3^2 - s_{3x}^2)}}\right)^{-1}, J_{tr}^{-1}(3,3) = cos(a)\left(\frac{s_{3x}}{\sqrt{(l_3^2 - s_{3x}^2)}}\right)^{-1},$$

$$J_{tr}^{-1}(3,4) = -(y^w cos(a) + (z^w + h_2) sin(a))\left(\frac{s_{3x}}{\sqrt{(l_3^2 - s_{3x}^2)}}\right)^{-1},$$

$$J_{tr}^{-1}(3,5) = (t+p)\left(cos(b) - sin(b)\left(\frac{s_{3x}}{\sqrt{(l_3^2 - s_{3x}^2)}}\right)^{-1}\right).$$

$J_{tr}^{-1}(4,1) = 0$, $J_{tr}^{-1}(4,2) = -cos(a)$, $J_{tr}^{-1}(4,3) = -sin(a)$,

$J_{tr}^{-1}(4,4) = y^w sin(a) - z^w cos(a) - h_2 cos(a)$, $J_{tr}^{-1}(4,5) = 0$.

$J_{tr}^{-1}(5,1) = 0$, $J_{tr}^{-1}(5,2) = 0$, $J_{tr}^{-1}(5,3) = 0$, $J_{tr}^{-1}(5,4) = -1$, $J_{tr}^{-1}(5,5) = 0$.

Appendix C

- **Spindle**

Maker: IBAG Switzerland AG
Model: HFK 90 S 40 C
Speed Range: ~ 50,000 rpm
Power Range: 1.9 kW
Torque: 0.4N-m
Tool Diameter: 0.5mm ~ 10.0mm
Motor Type: induction motor
Size: 90mm(diameter), 178.5mm(length)
Weight: 7.1kg

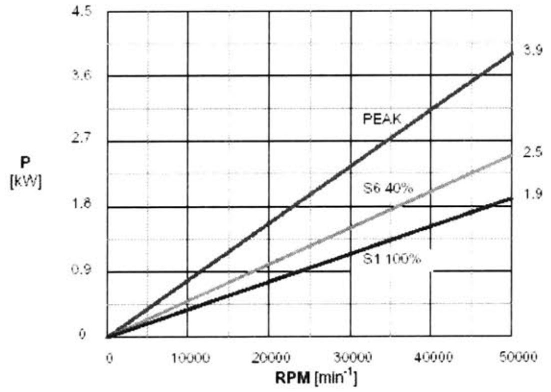

spindle power

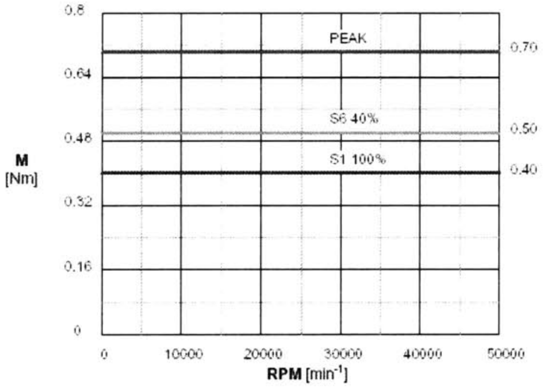

spindle torque

- **Motion controller**

Maker: Aerotech
Model: UNIDEX® 500 PCI
Axis processor: 80MHz, DSP
Axis Loop Type/Update Rate: PID with velocity and acceleration feedforward
62.5μsec/axis servo update time
Range Limits: Position(2^{47}-1counts); Velocity(2^{23}*steps/ms*);
Acceleration(2^{15}*steps/ms*^{2})
Process time: Command execution < 1ms; read request < 1ms
Programming: G-code, AeroBASIC™, C, C++, Visual Basic®, LabVIEW™

- **Amplifier**

Maker: Aerotech
Model: BA30
Output Voltage: 40-320VDC
Peak/Continuous Output Current: 30/15 A
Peak/Continuous Output Power: 8,160/4,080 W
Bandwidth: 2kHz
PWM Switching Frequency: 20kHz
Brushless Operation: Torque(current), velocity, dual phase

- **Servo-motor**

Maker: Aerotech
Model: BM500E
Continuous/Peak Torque: 3.6/9.0 N-m
Rated/Maximum Speed: 8,000/4,000 rpm
Rated Power: 1,100W (1.5hp)
Torque Constant: 0.19N-m/Amp$_{pk}$; 0.28N-m/Amp$_{rms}$
BEMF Constant: 23.6 V$_{pk}$/krpm
Rotor Moment of Inertia: 13.9x10^{-5}$kg \cdot m^2$
Number of Poles: 8

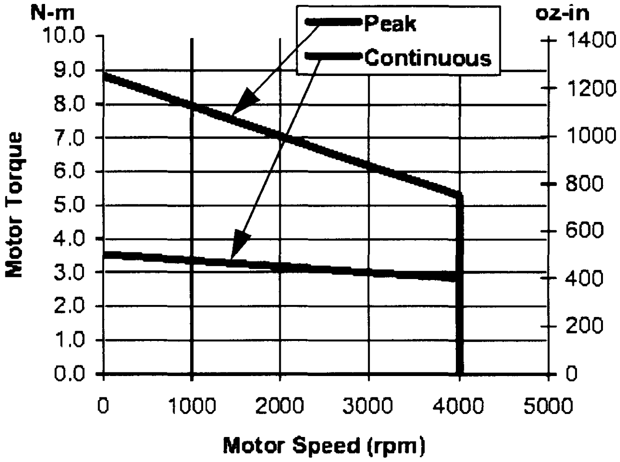

BM500E Motor Performance

Appendix D

- **Linear displacement sensor**

  Maker: Fastar
  Model: FS380
  Resolution: Infinite
  Non-linearity: < ±0.15%
  Repeatability: 0.003% of full scale
  Excitation: 112kHz
  Frequency response: DC to 15kHz (-3dB)
  Response time: 35μs

- **Impact hammer**

  Maker: PCB Piezotronics
  Model: PCB 086C20
  Voltage sensitivity: 0.23mV/N (±15%)
  Measurement range (-10dB): 1.0kHz
  Amplitude linearity: < ±1%
  Mounted resonant frequency: higher than 12kHz
  Excitation voltage/constant current: 18 to 30/2 to 20 VDC/mA
  Discharge time constant: 2,000sec

- **Accelometer**

  Maker: PCB Piezotronics
  Model: PCB 356B08
  Voltage sensitivity: 10mV(m/s^2)
  Frequency range: 0.5~5,000Hz(±5%), 0.3~6,500Hz(±10%)
  Resonant frequency: higher than 20kHz
  Measurement range: ±500m/s^{2}pk
  Resolution: 0.002m/s^{2}rms
  Linearity: ±1%

- **Signal analyzer**

  Maker: Hewllet-Packard
  Model: HP 35670
  Frequency range: 102.4 kHz 1 channel, 51.2 kHz 2 channel, 25.6 kHz 4 channel
  Dynamic range: 90 dB typical
  Accuracy: ±0.15 dB
  Channel match: ±0.04 dB and ±0.5 degrees
  Real-time bandwidth: 25.6 kHz/1 channel
  Resolution: 100, 200, 400, 800 and 1,600 lines
  Time capture: 0.8 to 5 Msamples